12-2014

# Exploring the Energy Density Functional with High-Performance Computing

Erik Michael Olsen
*University of Tennessee - Knoxville*, eolsen1@vols.utk.edu

To the Graduate Council:

I am submitting herewith a dissertation written by Erik Michael Olsen entitled "Exploring the Energy Density Functional with High-Performance Computing." I have examined the final electronic copy of this dissertation for form and content and recommend that it be accepted in partial fulfillment of the requirements for the degree of Doctor of Philosophy, with a major in Physics.

Witek Nazarewicz, Major Professor

We have read this dissertation and recommend its acceptance:

Vasilios Alexiades, Robert Grzywacz, Thomas Papenbrock

Accepted for the Council:

Carolyn R. Hodges

Vice Provost and Dean of the Graduate School

(Original signatures are on file with official student records.)

# Exploring the Energy Density Functional with High-Performance Computing

A Dissertation Presented for the

Doctor of Philosophy

Degree

The University of Tennessee, Knoxville

Erik Michael Olsen

December 2014

*This dissertation is dedicated to my family and friends, to whom I owe everything.*

*Thank you for all of your love and support!*

# Acknowledgments

I would like to thank Witek Nazarewicz, my advisor, for accepting me into his research group and for everything he has taught me about nuclear physics and science in general. I would not be the scientist I am today if not for his tutelage and guidance.

I am indebted to the late Mario Stoitsov for all of the time he took to teach me about programming and nuclear physics. The knowledge he gave me and his crucial work in developing nuclear physics codes made my research possible.

I am very grateful to Jochen Erler for helping me learn about computer parallelization and tutoring me in nuclear physics.

I am grateful to Noah Birge for all of his help through the years in running my calculations.

I am grateful to Nicholas Schunck for helping me in troubleshooting the nuclear physics codes used in my research.

I am grateful to Jordan Mcdonnell for his help in editing my dissertation.

I am grateful to John Trubisz, my high school physics teacher, for showing me the enjoyment of learning about the world around me and sparking my passion for physics.

I would like to thank Thomas Papenbrock, Robert Grzywacz, and Vasilios Alexiades for serving as my doctoral committee. I am very grateful for their time and feedback given on this dissertation.

Lastly, I want to thank the Physics and Astronomy Department of The University of Tennessee, Knoxville for accepting me into their program and for the funding they provided to me through my time in graduate school.

# Abstract

For theoretical nuclear physics to gain a comprehensive and quantitative understanding of all nuclei it is necessary to develop a framework where meaningful calculations can be made throughout the nuclear chart. Such a framework has been established; using nuclear Density Functional Theory along with massively parallel computing, it is now possible to analyze and predict global nuclear properties. For this work, large-scale mass tables were made using Skyrme Energy Density Functionals. Using the ground state binding energy, pairing gap, root-mean-square radius, and shape deformation data from these tables, the following global properties were analyzed: the two-proton and two-neutron drip lines, two-proton radioactivity, ground state reflection-asymmetric shapes, and neutron-skin thicknesses. These data were also used in the development of a new energy density functional. In order to determine the statistical and systematic uncertainties of these calculations, six different energy density functionals were used. Lastly, in an effort to better understand nuclear collective modes, parallel computing techniques were used in the development of a method to calculate the sum rules of energy centroids for giant resonances.

# Table of Contents

# List of Tables

# List of Figures

# Chapter 1

# Introduction

Research in low-energy nuclear theory focuses on describing and predicting properties of atomic nuclei and understanding how interactions occur at the nucleonic level. Work in this field has inspired the development of different nuclear structure models [1, 2]: *ab initio* methods, shell model approaches, and self-consistent mean field techniques [3, 4].

The ultimate goal of low-energy nuclear physics is a comprehensive and quantitative description of all nuclei and their reactions based on a microscopic (quantum mechanical) theory. There has been a renewed interest in this goal due to experimental advances at rare isotope beam facilities, new astrophysical observations and simulations, and nuclear energy and security needs [5]. One way to approach this problem is to use global properties to describe and predict trends of nuclei across the nuclear chart. To be able to use such a strategy, a nuclear model must be capable of performing reliable calculations on all types of nuclei, from stable to short lived and from light to superheavy systems. Which of the models listed above are ready to handle this task?

## 1.1 Nuclear Structure Models

*Ab initio* methods construct the nucleus "from scratch" using individual nucleons as building blocks held together by a Hamiltonian representing the bare nucleon-nucleon interaction. Since this interaction is not fully understood, it is constructed as an effective interaction from nucleon-nucleon scattering data [6]. Some examples of *ab initio* methods include the No Core Shell Model [7, 8] (which has had success in calculations up to $A = 14$ [9–11]), the Quantum Monte Carlo method [12] (with successful calculations for $A \leq 12$ [13–16]), and the Coupled Cluster Method [17] (which has yielded results on isotopes of calcium [18]). Due to the computational power needed to handle the configuration space of these and other *ab initio* calculations, they are currently limited to light nuclei, except for the coupled cluster method which reaches to medium-mass systems.

Shell model approaches build a nucleus by filling single particle states to form an inert core and use the valence protons and neutrons surrounding that core to describe nuclear properties. The nuclear potential is represented by a phenomenological mean-field interaction, often a Harmonic Oscillator or Woods-Saxon potential [19]. Modern calculations expand the original shell model of Mayer and Jensen [20, 21] by including a residual interaction between the valence protons and neutrons [22]. Some examples of shell model approaches include the Gamow Shell Model [23] (which has been used on isotopes of oxygen [24, 25]) and the Monte Carlo Shell Model [26, 27] (which has yielded results as far as the lanthanides [28]). Similarly to *ab initio* methods, shell model calculations are constrained by computational power and are currently limited to light- and medium-mass nuclei and heavy semi-magic systems.

Self-consistent mean-field techniques picture the nucleus as a collection of protons and neutrons that move independently of one another within an average potential produced by all of the nucleons present. The nuclear potential is developed using nuclear Density Functional Theory (DFT) [29, 30] and is represented by an energy density functional (EDF) with phenomenological inputs. These methods are based

on the electronic DFT [31] and include the Skyrme Hartree-Fock-Bogoliubov (HFB) method [32, 33], the Gogny HFB method [34, 35], and the relativistic mean-field model [36, 37]. Each of these methods has been used to perform calculations on nuclei all over the nuclear chart [38–41]. Self-consistent mean-field techniques employing nuclear DFT are the tool of choice when making such calculations for the following reasons [42]:

1. They are general enough to be confidently applied to any region of the nuclear landscape whose properties are largely unknown.

2. They allow for intrinsic symmetry-breaking effects resulting in a large variety of nuclear deformations.

3. They describe both finite nuclei and bulk nuclear matter.

4. They provide values for a variety of observables and are able to assess their error.

## 1.2 Motivation

To achieve the goal of a comprehensive and quantitative description of all nuclei within the framework of nuclear DFT it is essential to develop a universal EDF which is capable of accurately describing and predicting nuclear properties. The establishment of such an EDF has spurred three collaborative efforts between physicists, mathematicians, and computer scientists: the UNEDF (Universal Energy Density Functional) SciDAC-2 (Scientific Discovery through Advanced Computing) collaboration [5, 43, 44], its current successor the NUCLEI (Nuclear Computational Low-Energy Initiative) SciDAC-3 collaboration [45], and the FIDIPRO (Finland Distinguished Professor Programme) collaboration [46]. The goals of these partnerships are as follows [47]:

1. Develop an optimal EDF using all current knowledge of the nuclear Hamiltonian and basic nuclear properties.

2. Test this EDF against known data to verify its quality.

3. Apply this EDF to nuclear properties that cannot currently be measured.

The strategy used by nuclear DFT to accomplish these goals [48] is outlined in Figure 1.1, where the first step is the construction of the EDF. EDFs can be viewed as phenomenological effective interactions and contain a number of coupling constants; their values are optimized to experimental data and theoretical calculations on nuclear matter (pseudo-data) [49–51]. Given the mathematical form of the EDF, its predictive power ultimately depends on the data used in the optimization [52]. There are two possible ways to avoid this dilemma. The first is to build the EDF from an *ab initio* approach; a promising way of doing this is to use the density matrix expansion technique [53] in combination with chiral effective field theory [54]. While initial results are promising [55–57] this method is presently under development. The other way is to include higher-order density dependent interactions in the EDF [58]. This method is also under development.

The next step is to use this EDF to both verify its quality and to make predictions on quantities not yet measurable. Both of these can be accomplished through large-scale mass table calculations, where nuclear binding energies and properties associated with them (like shape deformation) are calculated on nuclei all over the nuclear chart. Making a large-scale mass table is no easy task [44], as it requires the development of codes able to make such calculations and the use of high-performance computing to obtain data in a reasonable amount of time. The data from these mass tables can be used in further calculations to make predictions on nuclear properties not yet measured. The construction and use of large-scale mass tables in this endeavor is the fundamental focus of this dissertation. Specifically, mass table data was used to analyze the following global properties: proton and neutron drip lines, two-proton

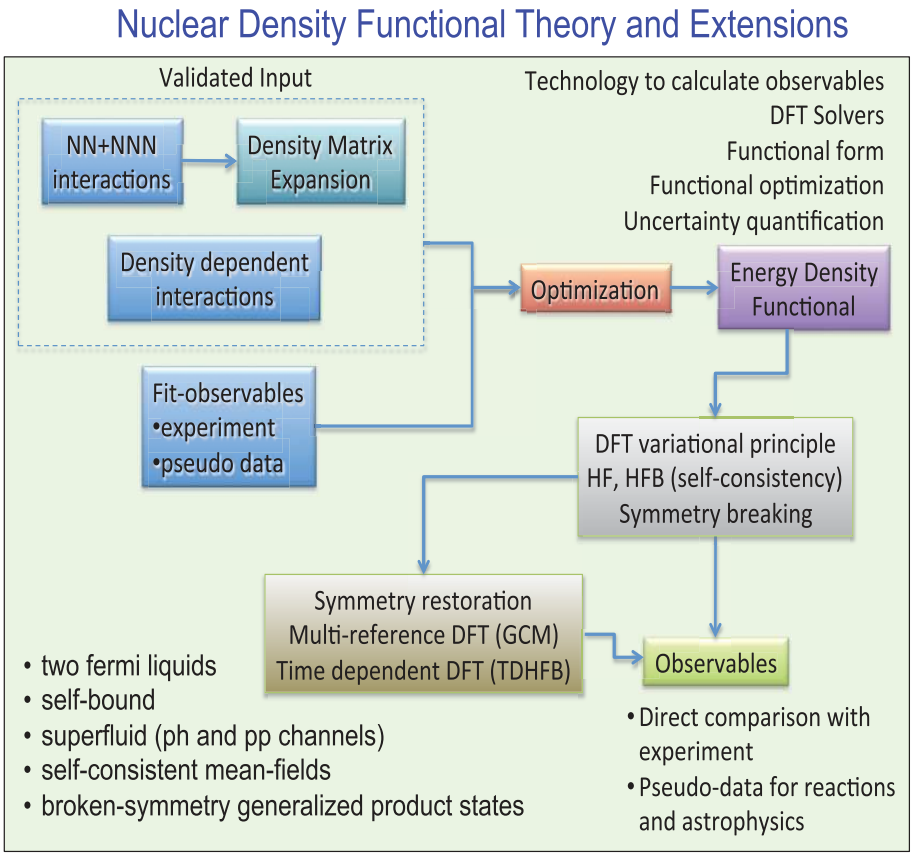


**Figure 1.1:** The nuclear DFT strategy diagram.

decay, and neutron skin thicknesses. They were also constructed to analyze reflection-asymmetric shapes in nuclear ground states and to assess the quality of a new EDF. Lastly, parallel computing techniques were used to improve a method of calculating the sum rules for nuclear giant resonances.

### 1.2.1 Proton and Neutron Drip Lines

Each atomic nucleus is made up of a certain number of protons and neutrons. Is every combination of protons and neutrons possible, or is there a limit as to how many of each can be added to a nucleus? In Chapter 3 we look at the concept of drip lines, the point at which nuclear binding ends on the nuclear chart. The positions of both the proton and neutron drip lines are assessed and their statistical and systematic

uncertainties are analyzed. We also make a theoretical estimate on the number of bound nuclei between proton numbers 2 and 120 [59].

### 1.2.2 Two-Proton Decay

In Chapter 4 we study the phenomenon of ground state two-proton ($2p$) radioactivity, a decay mode found in isotopes of nuclei with even atomic numbers located beyond the two-proton drip line. Experimentally, this process has only been observed in elements up to strontium ($Z = 38$); does it take place in heavier species? We perform a global analysis of $2p$ decay and identify candidates for this decay mode in elements all over the nuclear chart. We also predict cases where the competition between $2p$ and $\alpha$ decay may be observed [60, 61].

### 1.2.3 Neutron Skin

Neutron skin thickness is defined as the difference in root-mean-square (rms) radii of the neutron and proton distributions in a nucleus. Since it is a difference between neutron and proton features, neutron skin is an isovector property. In Chapter 5 we calculate neutron skin thickness values for nuclei across the nuclear chart. The statistical covariance technique is used to evaluate statistical error and both statistical and systematic errors are assessed to determine the uncertainty necessary for an experimental neutron skin value to further improve theory [62].

### 1.2.4 Reflection-Asymmetric Ground State Deformations

What is the shape of the nucleus in its ground state? In Chapter 6 we explore ellipsoidal (quadrupole) and reflection-asymmetric (octupole) shape deformations and their presence in even-even nuclear ground states. The statistical and systematic uncertainties of our calculations are examined. Lastly, the effect of deformation on binding energy and binding energy differences is studied for even-even isotopes of radium and thorium [48].

### 1.2.5 A New EDF

In Chapter 7 we discuss the new EDF parameterization UNEDF2 and compare it with the previous EDFs of the UNEDF collaboration. In particular, we examine the extra data used in its construction and how it was optimized. Calculations made with UNEDF2 are compared to other EDFs and their uncertainties are determined. With all of these details, the overall quality of UNEDF2 as an EDF is assessed [52].

### 1.2.6 Giant Resonances

So far, all of our work has focused on nuclear ground states. In Chapter 8 we investigate nuclear excited states in the form of giant resonances. We present a new method for calculating the sum rules of the energy centroids of these giant resonances using the Finite Amplitude Method. This method is augmented with parallel computing to increase its calculation speed dramatically. Results are shown for the inverse energy-weighted sum rule of the isoscalar giant monopole resonance and compared with the results of constrained HFB calculations.

# Chapter 2

# Methods

Before going any further it will be useful to first review the theoretical techniques and computational tools we used in our research. This chapter will be devoted to this task and is structured as follows. In Section 2.1 we review nuclear DFT, examine how an EDF is constructed, and discuss which EDFs were used in our work. The mean-field HFB approach for calculating nuclear binding energies is explained in Section 2.2. Finally, in Section 2.3 we review the codes created and used for this work and explain the parallelization routines developed for their use on high-performance computers.

## 2.1 Nuclear Density Functional Theory

In nuclear DFT, the total energy of the nucleus is given by [49]

$$E = \int \mathcal{H}(r) d^3r, \tag{2.1}$$

where $\mathcal{H}(r)$ is a local energy density that is a real, scalar, isoscalar, and time reversal invariant function of local densities and their derivatives. To go further with this expression we must specify the form of the nuclear interaction. The three most popular choices are a zero range Skyrme interaction [63, 64], a finite range Gogny interaction [34], and a relativistic interaction [65]. For our research the Skyrme

interaction was chosen, as its zero-range structure simplifies the HFB framework by making it local.

For the Skyrme EDF, the total binding energy of the nucleus $E$ is expressed as a functional of the one-body density $\rho(r)$ and pairing $\tilde{\rho}(r)$ matrices and the energy density $\mathcal{H}(r)$ is written as follows [4]:

$$\mathcal{H}(r) = E_{\text{kin}}(r) + E_{\text{int}}(r) + E_{\text{pair}}(r) + E_{\text{Coul}}(r) - E_{\text{corr}}, \tag{2.2}$$

where $E_{\text{kin}}$ is the kinetic energy density, $E_{\text{int}}$ is the particle-hole interaction energy density, $E_{\text{pair}}$ is the particle-particle pairing energy density, $E_{\text{Coul}}$ is the Coulomb energy density, and $E_{\text{corr}}$ is the correction for spurious motion. The coupling constants are found in $E_{\text{int}}$ and $E_{\text{pair}}$.

The interaction energy density can be written as [4]

$$E_{\text{int}} = \sum_{t=0,1} (\mathcal{E}_t^{\text{even}} + \mathcal{E}_t^{\text{odd}}), \tag{2.3}$$

where $\mathcal{E}_t^{\text{even, odd}}$ are the time-even and time-odd parts of the functional and $t$ is the isospin, where $t = 0$ corresponds to isoscalar densities ($\rho_0 = \rho_n + \rho_p$), $t = 1$ corresponds to isovector densities ($\rho_1 = \rho_n - \rho_p$), and $\rho_n$ and $\rho_p$ are respectively the neutron and proton densities. As we will limit our calculations to ground states of even-even nuclei (nuclei with even numbers of protons and neutrons), the time-odd parts do not contribute and will be ignored. Writing out the time-even part in terms of coupling constants:

$$\begin{aligned} E_{\text{int}} = \sum_{t=0,1} \Big( & C_t^{\rho\rho} \rho_t^2 + C_t^{\rho\tau} \rho_t \tau_t + C_t^{\mathbb{J}^2} \mathbb{J}_t^2 \\ & + C_t^{\rho\Delta\rho} \rho_t \Delta\rho_t + C_t^{\rho\nabla J} \rho_t \nabla \cdot \mathbf{J}_t \Big), \end{aligned} \tag{2.4}$$

where $\rho_t$ is the particle density, $\tau_t$ is the kinetic energy density, $\mathbb{J}_t^2$ is the tensor energy density, and $\mathbf{J}_t$ is the spin-orbit current density. The coupling constants $C_t^{\rho\tau}$,

$C_t^{\mathbb{J}^2}$, $C_t^{\rho\Delta\rho}$, and $C_t^{\rho\nabla J}$ are all real numbers, whereas $C_t^{\rho\rho}$ has the following density dependence [50]:

$$C_t^{\rho\rho} = C_{t0}^{\rho\rho} + C_{tD}^{\rho\rho}\rho_0^{\gamma}, \tag{2.5}$$

where $C_{t0}^{\rho\rho}$, $C_{tD}^{\rho\rho}$, and $\gamma$ are real numbers.

For $E_{\text{pair}}$ the following mixed-pairing description is used [66]:

$$E_{\text{pair}} = \sum_{q=n,p} \frac{V_0^q}{2}\left[1 - \frac{1}{2}\frac{\rho(r)}{\rho_0}\right]\tilde{\rho}_q{}^2(r), \tag{2.6}$$

where $\rho_0$ is the saturation density (set to 0.16 fm$^{-3}$) and $\tilde{\rho}_q$ is the local pairing density. $V_0^q$ are the coupling constants representing pairing strengths; different values are allowed for neutrons $V_0^n$ and protons $V_0^p$ [67].

To more easily relate the coupling constants to physical observables, it is advantageous to represent them in terms of nuclear matter properties (NMPs) which have clear physical interpretations and known ranges [68–70]. The NMPs chosen are the equilibrium density $\rho_c$, the total energy per nucleon at equilibrium $E/A$, the isoscalar effective mass $M_s^*$, the nuclear-matter incompressibility $K$, the symmetry energy coefficient $a_{\text{sym}}$, the density dependence of the symmetry energy $L_{\text{sym}}$, and the isovector effective mass $M_v^*$. This makes the coupling constants of the Skyrme EDF the following [49]:

$$\begin{aligned}\Big\{&\rho_c,\ E_{\text{NM}}/A,\ M_s^*,\ K^{\text{NM}},\ a_{\text{sym}}^{\text{NM}},\ L_{\text{sym}}^{\text{NM}},\ M_v^*,\\ &C_0^{\rho\Delta\rho},\ C_1^{\rho\Delta\rho},\ C_0^{\rho\nabla J},\ C_1^{\rho\nabla J},\ C_0^{J^2},\ C_1^{J^2},\ V_0^n,\ V_0^p\Big\},\end{aligned} \tag{2.7}$$

The isoscalar and isovector $C_t^{\rho\Delta\rho}$, spin-orbit $C_t^{\rho\nabla J}$, and tensor $C_t^{\mathbb{J}^2}$ terms cannot be represented in terms of NMPs and are left as is.

As stated in Chapter 1, these coupling constants are determined through a fit to experimental data. Some examples of such data are nuclear masses, radii, surface thickness, and mean energies of giant resonances, though more observables can be

used [3, 4, 49]. The actual fit is done by minimizing the objective function [62]

$$\chi^2(\mathbf{x}) = \sum_p \left( \frac{\mathcal{O}_p^{(\mathrm{th})}(\mathbf{x}) - \mathcal{O}_p^{(\mathrm{exp})}}{w_p} \right)^2 , \tag{2.8}$$

with respect to EDF parameters $\mathbf{x} = \{x_i\}$. Here $\mathcal{O}_p$ is a selected observable and $w_p$ is the corresponding weight that represents the adopted theoretical error.

There are two kinds of errors associated with calculations made from any parameterization: statistical and systematic [71]. The statistical error represents the theoretical uncertainty associated with model parameters and is obtained using least-squares covariance analysis [68, 72–74], where the statistical standard deviation of an observable $\mathcal{O}$ is given by

$$\sigma_{\mathcal{O}}^2 = \sum_{i,j} \mathrm{Cov}(x_i, x_j) \left[ \frac{\partial \mathcal{O}}{\partial x_i} \frac{\partial \mathcal{O}}{\partial x_j} \right], \tag{2.9}$$

where $\mathrm{Cov}(x_i, x_j)$ is the covariance matrix for the model parameters.

The systematic error represents the root-mean-square (rms) spread of predictions of different Skyrme EDFs obtained by means of diverse fitting protocols. In the absence of the exact reference model, such an inter-model deviation represents a rough approximation to the systematic error, and should be viewed as such. To assess the systematic error of our calculations, we used 6 different EDF parameterizations: SkM* [75], SkP [32], SLy4 [76], SV-min [68], UNEDF0 [49], and UNEDF1 [50]. They were developed with the following priorities [59]:

- SkM* was developed with a focus on surface energy and fission barriers in actinides.
- SkP aimed at a simultaneous description of the mean field and the pairing interaction.
- SLy4 was optimized with an emphasis on neutron-rich nuclei and properties of neutron matter.

- SV-min was adjusted to a variety of data on spherical nuclei, such as diffraction radii and surface thickness.
- UNEDF0 was developed by considering data on spherical and deformed nuclei.
- UNEDF1 was developed with UNEDF0's data set combined with excitation energies of fission isomers.

## 2.2 The Hartree-Fock-Bogoliubov Equations

Our objective is to calculate the ground state energy of a particular nucleus. As the nucleus is too complex to allow for an exact solution, we use the variational principle to find an approximation [77]:

$$\delta E\big[\Psi\big] = 0, \tag{2.10}$$

where

$$E\big[\Psi\big] = \frac{\langle\Psi|E[\rho,\tilde{\rho}]|\Psi\rangle}{\langle\Psi|\Psi\rangle}. \tag{2.11}$$

The ground state wavefunction $|\Psi\rangle$ is built using the Hartree-Fock-Bogoliubov (HFB) approach. The HFB method is a generalization of the Hartree-Fock (HF) method and the BCS model (named for Bardeen, Cooper, and Schrieffer [78]). Specifically, it combines the long-range particle-hole interactions of the HF method with the short-range particle-particle pairing interactions of the BCS model. Its key concept is to represent the ground state of the system as a vacuum with respect to **quasi-particle operators**

$$\beta_k|\Psi\rangle = 0 \quad \forall \;\; k, \tag{2.12}$$

where $\beta_k$ is the quasi-particle annihilation operator. They are related to the single particle operators in the following way:

$$\begin{aligned}\beta_k^\dagger &= \sum_l U_{lk} c_l^\dagger + V_{lk} c_l, \\ \beta_k &= \sum_l U_{lk}^* c_l + V_{lk}^* c_l^\dagger,\end{aligned} \tag{2.13}$$

where $\beta_k^\dagger$ is the quasi-particle creation operator and $c_l^\dagger$ and $c_l$ are the single-particle creation and annihilation operators respectively [77]. Since these quasi-particle operators represent fermions, they must obey the fermion anti-commutation relations

$$\begin{aligned}\{\beta_k^\dagger, \beta_{k'}^\dagger\} = \{\beta_k, \beta_{k'}\} = 0, \\ \{\beta_k^\dagger, \beta_{k'}\} = \delta_{kk'}.\end{aligned} \tag{2.14}$$

This puts the following conditions on the matrices $U$ and $V$:

$$\begin{aligned}U^\dagger U + V^\dagger V = 1, \\ U U^\dagger + V^* V^T = 1, \\ U^T V + V^T U = 0, \\ U V^\dagger + V^* U^T = 0.\end{aligned} \tag{2.15}$$

To ensure that the ground state is unique, the following two quantities are defined: the density matrix $\rho$ and the pairing matrix $\tilde{\rho}$:

$$\begin{aligned}\rho &= V^* V^T, \\ \tilde{\rho} &= -V^* U^T.\end{aligned} \tag{2.16}$$

The energy of the system given in equation 2.1 is defined in terms of quasi-particle operators, and the variation is taken with respect to $\rho$ and $\tilde{\rho}$ to give the HFB

equations:

$$\begin{pmatrix} h-\lambda & \Delta \\ -\Delta^* & -h^*+\lambda \end{pmatrix} \begin{pmatrix} U_k \\ V_k \end{pmatrix} = E_k \begin{pmatrix} U_k \\ V_k \end{pmatrix}, \tag{2.17}$$

where $h$ is the HF Hamiltonian containing the self-consistent field, $\Delta$ is the pairing field, $\lambda$ is the chemical potential, $E_k$ are the one-quasiparticle energy eigenstates, and $(U_k, V_k)$ are the two-component HFB eigenvectors (the columns of the matrices that determine the quasi-particle operators) [48]. The solution of these equations yields the ground state binding energy of a nucleus. As $h$ and $\Delta$ are both depend on $\rho$ and $\tilde{\rho}$, this is a non-linear eigenvalue problem and requires a self-consistent solution.

## 2.3 HFB Solvers

Solving the HFB equations is no easy task, and a great deal of effort is placed in the development of computer codes that can complete it. Three such codes were used to produce all of the results in this dissertation: HFBTHO [79], its updated version HFBTHOv200d [80], and AxialHFB [48]. To allow for large scale mass table calculations, all of these codes were augmented with Message Passing Interface (MPI) routines.

### 2.3.1 HFBTHO

HFBTHO solves the HFB equations through direct diagonalization using cylindrical coordinates in one of two bases: the harmonic oscillator (HO) or transformed harmonic oscillator (THO) based on the local scaling transformation [81]. The HO basis was used for all of the work presented in this dissertation. The size of the basis was set to 20 oscillator shells (1771 basis states); this gave the best accuracy vs calculation time ratio. To approximately restore particle number symmetry broken by the HFB method, the Lipkin-Nogami [82, 83] method as implemented in [84] was used.

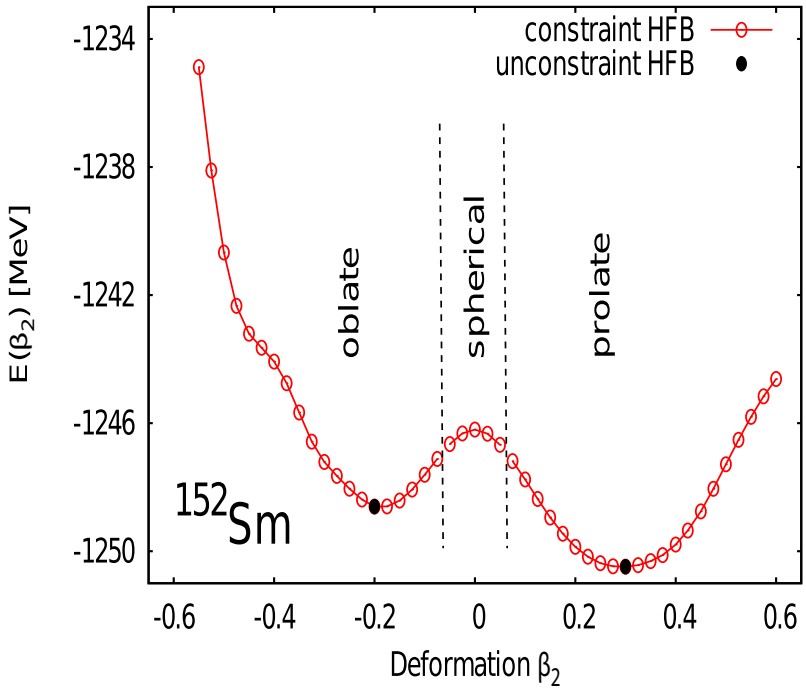


**Figure 2.1:** The potential energy surface of the deformed nucleus $^{152}$Sm as a function of the quadrupole deformation $\beta_2$. Open circles mark three regions of nuclear shapes (oblate, spherical, and prolate) where deformation-constrained HFB calculations are performed. The local minima (dots) are obtained by unconstrained HFB calculations initiated from the neighboring constrained solutions.

The ground state binding energy depends on the shape of the nucleus (nuclear deformations will be covered in detail in Chapter 6). Since the shape of a nucleus is not usually known *a priori*, solutions with many different shapes must be found. As HFBTHO conserves both axial symmetry and parity, it can only make calculations on shapes that do the same. The most important are ellipsoidal shapes, expressed in terms of quadrupole deformations $\beta_2$ [85]. The procedure [86] is shown schematically in Figure 2.1 for the deformed nucleus $^{152}$Sm. To find the ground state minimum, we divide the potential energy surface into three regions: spherical ($\beta_2 = 0$), prolate ($\beta_2 > 0$), and oblate ($\beta_2 < 0$). In each region, we calculate the total energy by constraining the total quadrupole moment $Q_{20}$ of the nucleus. If a local minimum

is found, we carry out an unconstrained calculation to pin down its energy, and the ground state energy is eventually obtained by taking the lowest energy solution.

As one HFBTHO solution representing a single nuclear configuration can be performed on a single core, mass table calculations are embarrassingly parallel. For our large-scale mass table calculations, HFBTHO was extended with a minimal MPI communication in order to run in parallel across many cores. The scaling of the mass table calculation with the number of cores implies that a simple master-slave parallel architecture is sufficient.

These calculations were done for a wide range of nuclei to ensure that all particle bound species between the proton and neutron drip lines would be included (our work on calculating the positions of those drip lines is detailed in Chapter 3). We used the JAGUAR (now TITAN) and KRAKEN (now decommissioned) Cray XT5 supercomputers housed at the Oak Ridge National Laboratory's Leadership Computing Facility and the University of Tennessee's National Institute for Computational Sciences, respectively. Figure 2.2 [86] shows all 4508 even-even nuclei initially included in the mass table calculations. Using 9060 processors of JAGUAR, computation of the entire even-even mass table took about 2 hours.

### 2.3.2 HFBTHOv200d

The newest version of HFBTHO, HFBTHOv200d, was recently completed and used for some of the work presented here. Its improvements from HFBTHO which were useful for the purposes of this work are the following [80]:

1. An improved Coulomb interaction has been implemented.

2. The modified Broyden's method [87] has been added to allow for faster convergence to a solution.

3. Optional breaking of reflection symmetry has been implemented.

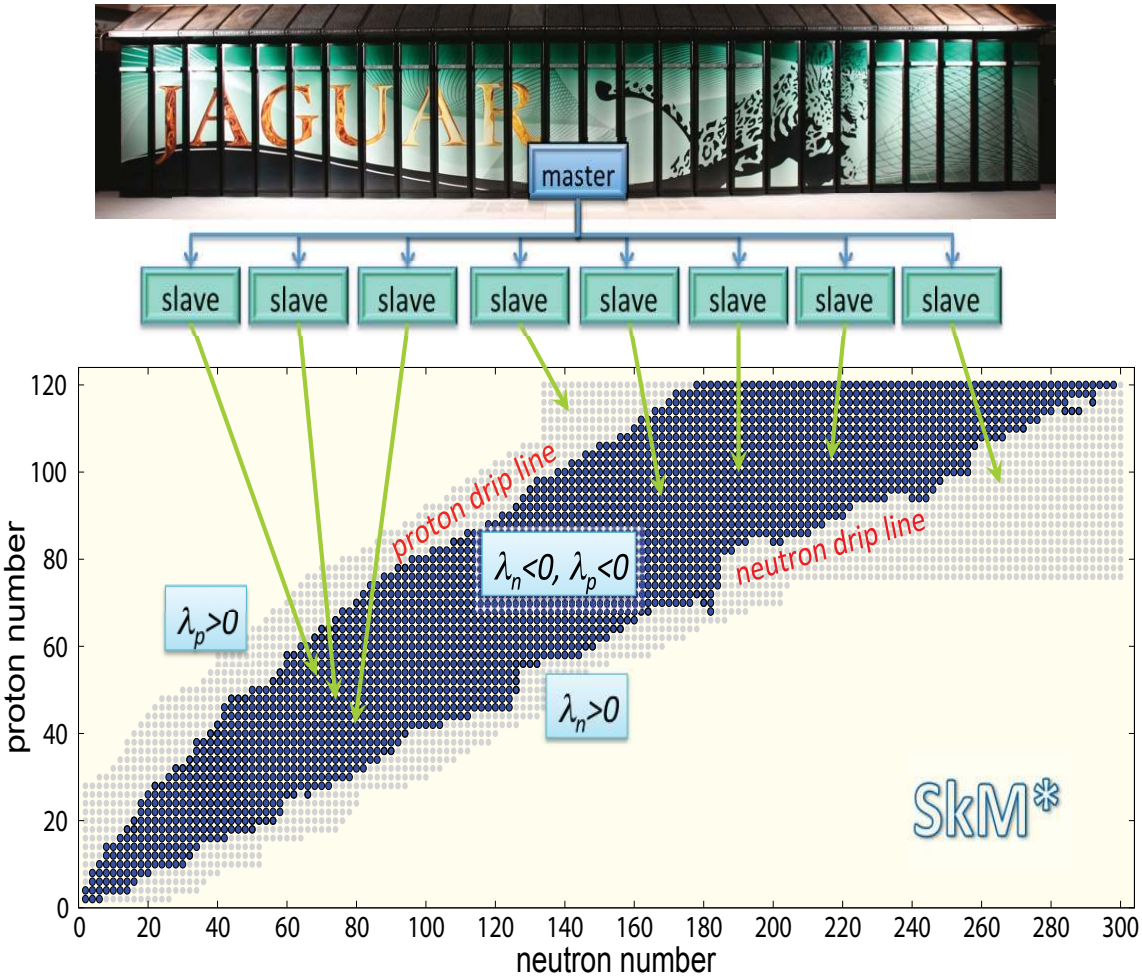


**Figure 2.2:** Computing a nuclear mass table on a supercomputer (in this case, the JAGUAR XT5). The problem is embarrassingly parallel, as a single HFB run can be carried out on one slave core without communicating with the other tasks. Calculations were performed using the SkM* EDF for 4508 even-even nuclei (gray circles). 2333 of those nuclei (marked by dark dots) are predicted to be particle stable. Image of JAGUAR courtesy of the National Center for Computational Sciences, Oak Ridge National Laboratory.

4. The calculation of all axial multipole moments (corresponding to nuclear deformations) up to $\lambda = 8$ has been added.

5. The linear constraint method based on the approximation of the Random Phase Approximation (RPA) matrix for multi-constraint calculations has been added.

6. The blocking of quasiparticles in the Equal Filling Approximation (EFA), allowing for the calculation of even-odd and odd-odd systems, has been implemented.

The MPI of HFBTHOv200d is currently the same as the one used for HFBTHO.

### 2.3.3 AxialHFB

AxialHFB is very similar in construction to HFBTHO with two notable exceptions. First, it solves the HFB equations using the gradient method routine provided by L. M. Robledo [88]. This method is particularly well suited to deal with multiple constraints [77] and does not require special techniques such as the augmented Lagrangian method [89] implemented in HFBTHO. Second, AxialHFB is also capable of breaking intrinsic reflection symmetry, allowing for the calculation of parity-breaking shapes. It has also been augmented with the Coulomb interaction used in HFBTHOv200d.

The task of AxialHFB is the same as HFBTHO: find the ground state binding energy of a nucleus. Since AxialHFB allows for parity-breaking shapes, we include in our search reflection-asymmetric (or pear-like) shapes expressed as octupole deformations $\beta_3$, as well as ellipsoidal shapes. The procedure [48] is shown schematically in Figure 2.3 for the nucleus $^{220}$Ra. To find the ground state minimum, we perform calculations for a set range of quadrupole and octupole deformation constraints. When the lowest energy value corresponding to the constrained calculations is found, a precise unconstrained calculation is performed from that point to determine the ground state energy.

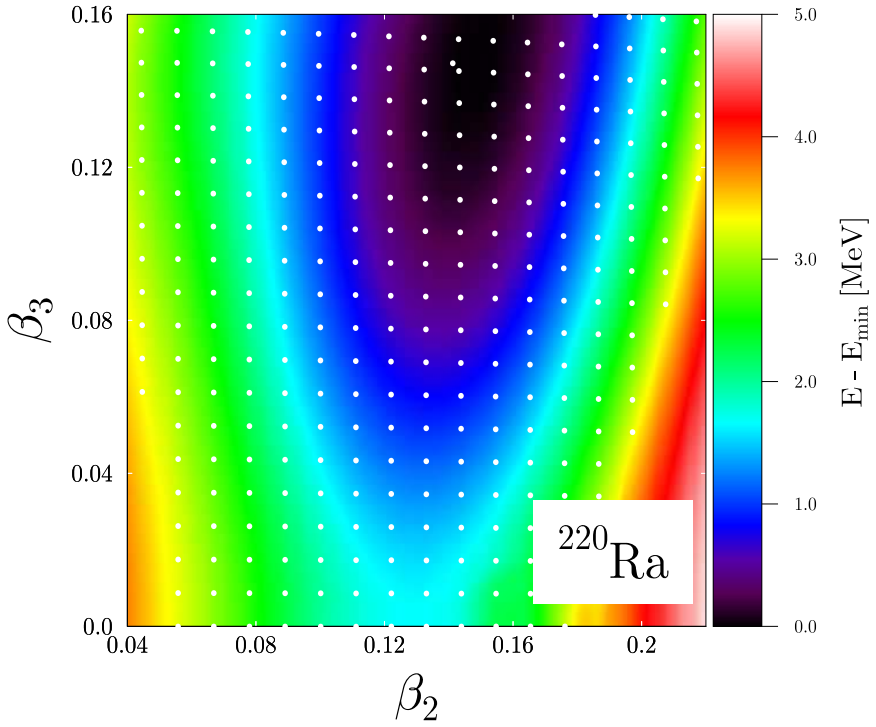


**Figure 2.3:** The contour map of the 2D potential energy surface of $^{220}$Ra calculated with the SLy4 EDF by constraining both the quadrupole and octupole moments characterized by shape deformations $\beta_2$ and $\beta_3$, respectively. The mesh points at which calculations were performed are marked by white dots. The energy (in MeV) is shown relative to the ground state minimum.

Like HFBTHO, AxialHFB was extended with a minimal MPI communication to run in parallel across many cores. The calculations were done on nuclei found to be within our calculated drip lines [59]. For this task we used the KRAKEN Cray XT5, DARTER Cray XC30 (housed at the University of Tennessee's National Institute for Computational Sciences), and EOS Cray XC30 (housed at the Oak Ridge National Laboratory's Leadership Computing Facility) supercomputers. Using AxialHFB, an even-even mass table can be completed in about 13 hours. However, neither DARTER nor EOS is large enough to calculate an entire mass table at once, so the table calculations were split into smaller pieces. At the time of writing, a mass table calculation has only been done for UNEDF0, and the other EDFs will be completed in future work.

# Chapter 3

# The Limits of the Nuclear Landscape: Proton and Neutron Drip Lines

This chapter is revised based on the following published work:

- J. Erler, N. Birge, M. Kortelainen, W. Nazarewicz, E. Olsen, A. Perhac, and M. Stoitsov, "The Limits of the Nuclear Landscape", *Nature* **486**, 509 (2012).

My primary contributions to this paper can be found in Chapter 10.

## 3.1 Introduction

Every atomic nucleus is characterized by a specific number of protons and neutrons and occupies a place on the nuclear chart. This chart is bounded by *drip lines*, indicated by the values of proton and neutron number where there is not enough binding energy to prevent the last nucleons from escaping the nucleus. Where are the drip lines on the nuclear chart, and how many nuclei exist between them?

There are approximately 3000 known nuclei that either occur naturally on Earth or can be synthesized in a laboratory [90, 91], with 100 more being added in 2011

[92], 67 in 2012 [93], and 12 in 2013 [94]. Of those, only 288 are stable or practically stable (with a half-life longer than the expected lifetime of the Solar System) and form the so-called "valley of stability". One moves out of this valley with increasing nucleon number and soon enters the vast territory of short-lived radioactive nuclei, which decay by $\alpha$ or $\beta-$ emission or by spontaneous fission. At some point, adding more nucleons doesn't produce a new bound nucleus; this is when the drip line is reached.

Experimentally, the proton drip line has been determined up to protactinium ($Z = 91$) [90], while the neutron drip line has only been determined up to oxygen ($Z = 8$) [91]. This is due to the close proximity of the proton drip line to the valley of stability, whereas the neutron drip line is much farther away. Very neutron-rich nuclei are studied through the fragmentation of stable nuclei and are particularly challenging to generate because of very low production rates and difficulties in the separation and identification of the products. It is expected that the next generation of radioactive ion-beam facilities will greatly extend our knowledge of the neutron drip line up to $A \approx 100$ [95].

The hunt for the limits of nuclear binding is also motivated theoretically, as it is closely connected to the question of the origin of elements in the universe. The astrophysical rapid proton capture (rp) and rapid neutron capture (r) processes, which are responsible for the generation of many heavy elements, are thought to operate very closely to the drip lines [96, 97].

The stability of a nucleus is primarily determined by its separation energy [91], the amount of energy needed to remove from it a single neutron ($S_n$), single proton ($S_p$), two neutrons ($S_{2n}$), or two protons ($S_{2p}$). Written in terms of binding energies:

$$
\begin{aligned}
S_n &= B(Z, N-1) - B(Z, N), \\
S_p &= B(Z-1, N) - B(Z, N), \\
S_{2n} &= B(Z, N-2) - B(Z, N), \\
S_{2p} &= B(Z-2, N) - B(Z, N),
\end{aligned} \tag{3.1}
$$

where $Z$ is the proton number, $N$ is the neutron number, and $B(Z, N)$ is the binding energy of the nucleus. These expressions can also be written in terms of chemical potentials $\lambda$ and pairing gaps $\Delta$ [98]:

$$
\begin{aligned}
S_n &\approx -\lambda_n - \Delta_n, \\
S_p &\approx -\lambda_p - \Delta_p, \\
S_{2n} &\approx -2\lambda_n, \\
S_{2p} &\approx -2\lambda_p.
\end{aligned} \tag{3.2}
$$

If the separation energy is positive, the nucleus is stable against nucleon emission; conversely, if the separation energy is negative, the nucleus is unstable against it. The neutron drip line is reached when $S_n \approx 0$ (for the one-neutron drip line) or $S_{2n} \approx 0$ (for the two-neutron drip line); analogous definitions apply to the proton drip lines.

The drip line position is strongly affected by nucleonic superfluidity, or pairing [99], which causes nuclei with even numbers of protons and neutrons to be more bound than their odd-nucleon numbered neighbors. A prime example of this is seen in isotopes of helium: the even-even species $^{4}$He, $^{6}$He, and $^{8}$He are bound whereas the isotopes with odd neutron number $^{5}$He, $^{7}$He, and $^{9}$He are not. Evidence of pairing is also found by the fact that the one-nucleon drip line is reached earlier than the two-nucleon drip line, and the region of nuclear existence has a border which zigzags between odd and

even nucleon species. Since the aim of this study is to estimate the maximum extent of nuclear binding, we focus on even-even nuclei and two-nucleon separation energies. However, other separation energies and drip lines can be estimated from even-even calculations using the expressions of 3.1 given above.

To make assessments on the drip lines, it is necessary to calculate the separation energies of as many nuclei as possible. For this task the mass table binding energies, chemical potentials, and pairing gaps of HFBTHO were used. For even-even nuclei all separation energies could be calculated directly from the mass table data. For even-Z, odd-N nuclei the chemical potentials and pairing gaps needed were found by taking an average over their even-even $N+1$ and $N-1$ neighbors (similarly for odd-Z, even-N nuclei). For odd-Z, odd-N nuclei the chemical potentials and pairing gaps were obtained by taking an average over their even-Z, odd-N and odd-Z, even-N neighbors.

## 3.2 Results

The summary of our survey across the nuclear chart is presented in Figure 3.1. The dashed grey gridlines show the magic numbers known around the valley of stability (20, 28, 50, 82, 126) as well as the predicted regions of stability in superheavy nuclei around $N = 184$ and 258 [95]. The mean two-nucleon drip lines and their associated systematic uncertainties have been obtained by averaging the predictions of individual models (see Table 3.2). Also shown is the two-neutron drip line of SV-min together with its statistical error bars at $Z = 12$, 68, and 120. As can be seen, the statistical error generally falls into the band of systematic uncertainty.

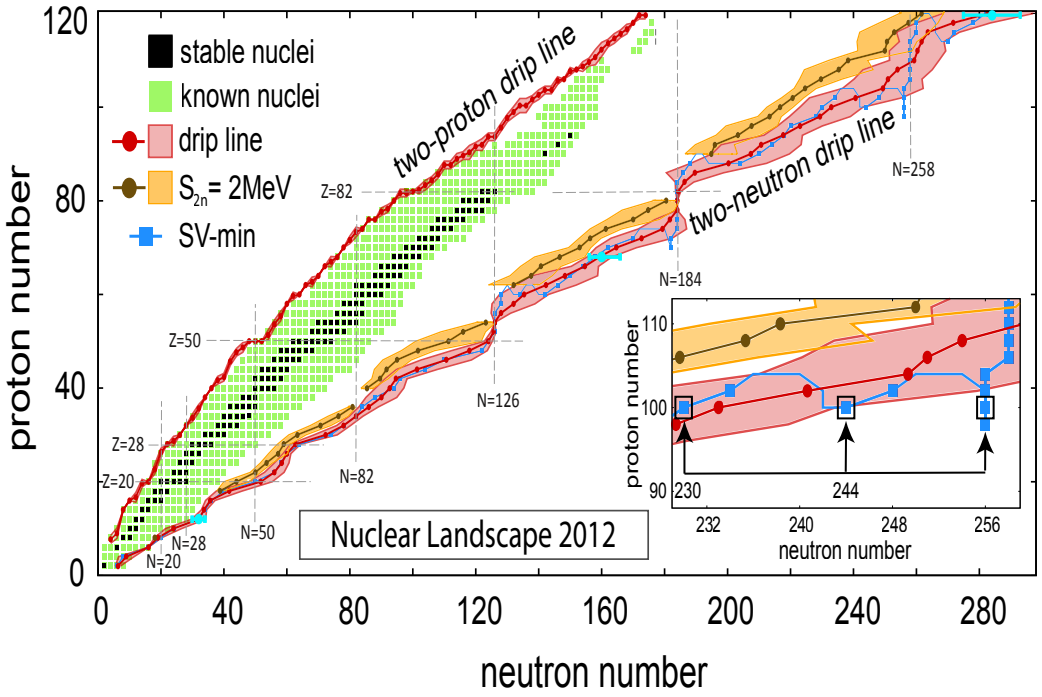


**Figure 3.1:** Map of even-even bound nuclei as a function of $Z$ and $N$. The 767 squares represent the stable (black) and radioactive (green) even-even isotopes known experimentally [90, 91]. The mean drip lines and their uncertainties (red) were obtained by averaging the results of different models. The two-neutron drip line of SV-min (blue) is shown together with the statistical uncertainties at $Z = 12$, 68, and 120 (blue error bars). The $S_{2n} = 2$ MeV line is also shown together with its systematic uncertainty (orange). The inset shows the irregular behavior of the two-neutron drip line around $Z = 100$.

Figures 3.2 and 3.3 demonstrate the difficulties associated with theoretical extrapolations toward the drip lines. The $S_{2n}$ values are shown for the isotopic chains of even-even erbium and zirconium isotopes predicted with the SLy4, SV-min, UNEDF0, and UNEDF1 EDFs and the FRDM [100] and HFB-21 [101] models. In the region for which experimental data exist, all models agree and reproduce the data well. However, the discrepancy between models steadily grows when moving away from this region. This is because the dependence of the effective interaction on the neutron-to-proton asymmetry (neutron excess) is poorly determined. This is seen in both the right inset of Figure 3.2, where the two-neutron drip line is predicted to be between $N = 154$ (FRDM) and $N = 162$ (UNEDF0), and in the inset of Figure

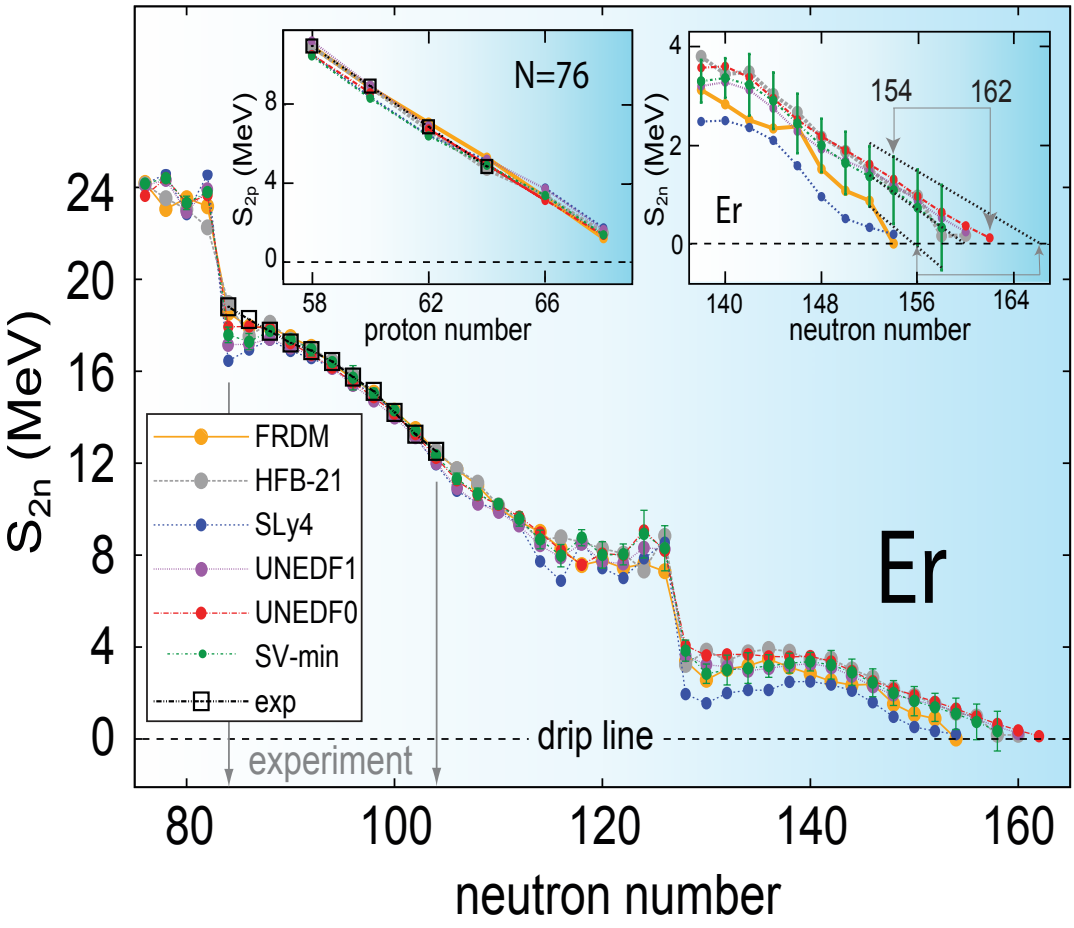


**Figure 3.2:** Calculations performed in this work using the SLy4, SV-min, UNEDF0, UNEDF1, FRDM [100] and HFB-21 [101] models for even-even isotopes of erbium. The differences between model predictions are small in the regions where data exist (bracketed by vertical arrows) and grow steadily when extrapolating toward the two-neutron drip line. The bars on the SV-min results indicate statistical errors due to uncertainty in the coupling constants of the functional. Detailed predictions around $S_{2n} = 0$ are illustrated in the right inset. The left inset depicts the calculated and experimental $S_{2p}$ values at $N = 76$.

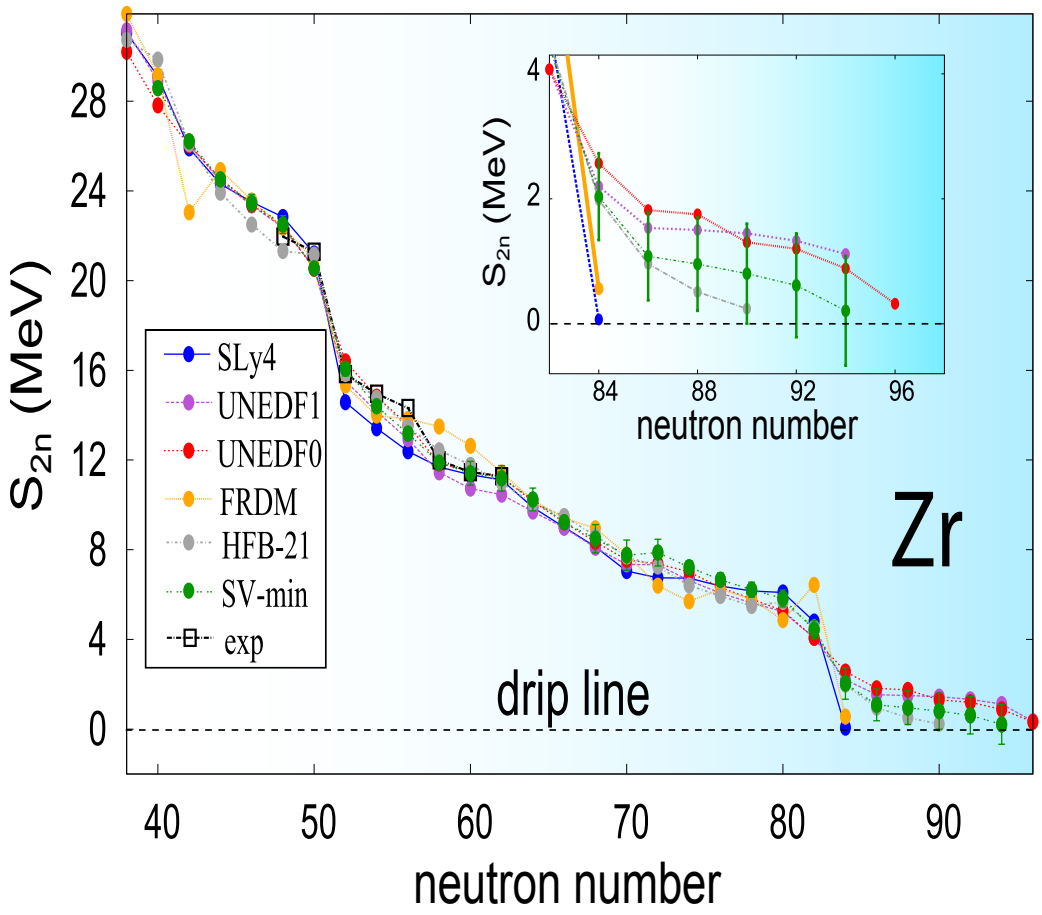


**Figure 3.3:** Similar to Figure 3.2 but for even-even zirconium isotopes. The inset figure shows detailed predictions around $S_{2n} = 0$; $S_{2p}$ analysis was not performed for these isotopes.

3.3, where the two-neutron drip line is predicted to be between $N = 84$ (FRDM) and $N = 96$ (UNEDF0); that is, the model-dependent 'error-bar' is appreciable. This is not the case for the two-proton drip line, where the associated extrapolation error is small and all the models we used are in excellent agreement with experiment (as seen in the left inset of Figure 3.2). This is due to the two-proton drip line's close proximity to the valley of stability, made possible by the repulsive electrostatic interaction between protons and because the proton continuum is effectively shifted up in energy as a result of the confining effect of the Coulomb barrier.

In addition to systematic errors, calculated observables are also subject to statistical errors due to uncertainties in EDF parameters [68, 72]. Figure 3.2 shows how the statistical error in $S_{2n}$ predicted with the SV-min EDF propagates with $N$. The gradual growth of error bars when approaching the two-neutron drip line is primarily caused by the isovector coupling constants of the functional that are not well constrained by current data [72]. The resulting statistical error in the position of the two-neutron drip line can be obtained by extrapolating the error band of calculated values toward $S_{2n} = 0$ (indicated by dotted lines in the right inset of Figure 3.2). In the case of SV-min and erbium isotopes, the statistical uncertainty corresponds to $N = 156$ to 166.

Looking back at Figure 3.1 we see that the theoretical error in the position of the two-neutron drip line grows steadily with distance from the valley of stability. Yet the overall consistency of our model predictions is greater than initially anticipated. This is particularly true for $N \leq 50$ and $N$ around 60, 126, and 184, where the error band is small. We also observe that the recently discovered isotope $^{40}$Mg [102] is predicted to be two-neutron bound by all of our models. In addition, the neutron-rich isotopes $^{26}$O and $^{28}$O are consistently calculated to lie inside the two-neutron drip line. While $^{26}$O has been observed experimentally [103] $^{28}$O has not [91, 93, 94], and configuration interaction calculations [104] have attributed this anomalous behavior to the repulsive three-body force (see however, [105]). If a similar effect is observed in heavier nuclei,

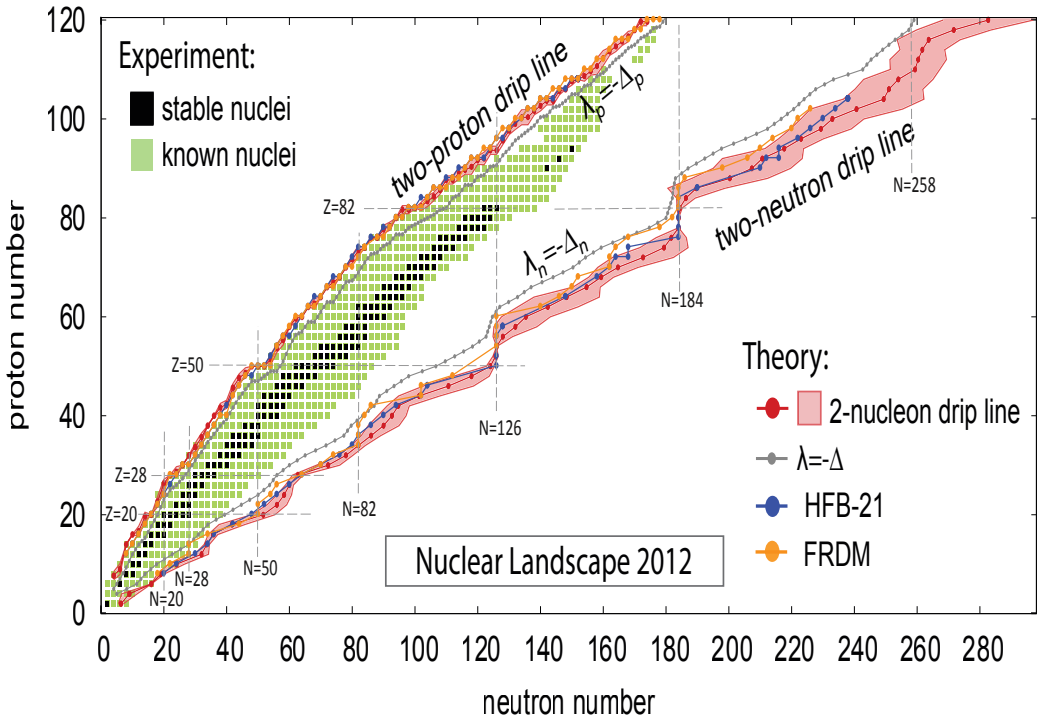


**Figure 3.4:** Similar to Figure 3.1 but includes predictions of the FRDM and HFB-21 models. The $\lambda_n = -\Delta_n$ and $\lambda_p = -\Delta_p$ one-nucleon drip line trajectories are added to indicate the extent of odd-N and odd-Z systems, respectively.

where DFT calculations are believed to be more reliable, this may suggest systematic modifications of the isovector-density-dependent interactions of the EDF.

As shown in Figure 3.4, the predictions of the FRDM and HFB-21 models also generally fall within our uncertainty band; this is consistent with Figures 3.2 and 3.3, where both models are generally consistent with our calculated uncertainty bands for the two-neutron drip line and show excellent agreement with the predicted two-proton drip line. The results of a follow up project using three different relativistic interactions [106] show great consistency with the uncertainties of the Skyrme DFT drip line results shown here. This is an interesting result given the difference in construction between the two interactions and lends confidence to these predictions.

Figure 3.1 also shows a complicated zigzag pattern of the two-neutron drip line in some regions. The inset shows the irregular behavior of the two-neutron drip line predicted by SV-min at around $Z = 100$. Although the primary drip line is located

at $N = 230$, neutron binding reappears around $N = 242$ and then again at $N = 256$, giving rise to secondary and tertiary drip lines. Such behavior is due to the presence of shell effects at neutron closures that tend to lower the binding energy along the localized bands of stability [107]. The phenomenon of re-entrant binding is predicted in several areas of the two-neutron drip line, for example at around $Z = 60$ (for $N = 132$ and 140), $Z = 70$ (for $N = 182$), and $Z = 100$ (for $N = 258$). All cases are shown in Table 3.2, where any number marked with an asterisk indicates the neutron number for the primary two-neutron drip line.

Figure 3.1 also shows the $S_{2n} = 2$ MeV line, together with its uncertainty band, corresponding to the very neutron-rich r-process path. Again our predictions seem fairly robust, especially around the neutron magic numbers where separation energies change rapidly. Such theoretical data can be used in future r-process simulations to estimate uncertainties of element abundances related to theoretical uncertainties of separation energies.

There is a great deal of consistency between models regarding the position of the two-proton drip line, with the calculated systematic uncertainty usually not exceeding $\Delta Z = 2$. The nuclides $^{42}$Cr, $^{48}$Ni, and $^{54}$Zn, which are known to be two-proton unstable, are firmly predicted as such, as are the $\alpha$-emitters $^{166}$Pt, $^{172}$Hg, and $^{186}$Po.

In Table 3.1 we show for $2 \leq Z \leq 120$ the number of bound even-even nuclei and the total number of bound nuclei (even-even, even-odd and odd-odd species) predicted from the mass table calculation of each EDF. The total number of bound nuclei we predict with the Skyrme-DFT approach is $6900 \pm 500_{syst}$. Previous theoretical estimates on this number are quite uncertain, ranging from 5000 to 12000 isotopes [108, 109]. To put things in perspective, recall in Section 3.1 that only approximately 3000 nuclei have been experimentally confirmed.

**Table 3.1:** The number of even-even nuclei and the total number of nuclei predicted from the mass table calculation for each EDF.

| EDF | Even-Even | Total |
|---|---|---|
| SkM* | 2333 | 7512 |
| SkP | 2042 | 6575 |
| SLy4 | 1928 | 6235 |
| SV-min | 2116 | 6734 |
| UNEDF0 | 2209 | 7400 |
| UNEDF1 | 2219 | 7163 |

## 3.3 Conclusion

Although the majority of rare isotopes inhabiting the outskirts of the nuclear landscape are unlikely to be seen, their properties impact astrophysical processes and, hence, all the matter around us. The road to understanding those exotic species takes us through reliable nuclear simulations with quantified uncertainties, and this study represents a step in that direction. In the long term, of particular importance is the development of novel nuclear EDFs that reproduce both bulk nuclear properties and spectroscopic data. Work along these lines is already in progress [49, 50].

The experimental range of the nuclear landscape continues to increase as new isotopes are discovered each year. As experiment advances, so too does theory, as more quantitative models of the nucleus are being developed with the aid of high-performance computing.

**Table 3.2:** The values for the two-nucleon drip lines for each EDF. For a given Z, the neutron numbers corresponding to the two-proton (first number) and two-neutron drip lines (second number) are shown. An asterisk marks the case where the drip line is first broken (see inset of Fig. 3.1.)

| Z | SkM* | | SkP | | SLy4 | | SV-min | | UNEDF0 | | UNEDF1 | |
|---|---|---|---|---|---|---|---|---|---|---|---|---|
| 2 | 2 | 6 | 2 | 6 | 2 | 6 | 2 | 6 | 2 | 6 | 2 | 6 |
| 4 | 2 | 14 | 2 | 8 | 2 | 8 | 2 | 8 | 2 | 8 | 2 | 8 |
| 6 | 4 | 16 | 4 | 16 | 4 | 16 | 4 | 16 | 4 | 16 | 4 | 16 |
| 8 | 4 | 20 | 6 | 18 | 6 | 18 | 6 | 20 | 6 | 20 | 4 | 18 |
| 10 | 6 | 28* | 6 | 24 | 8 | 20* | 8 | 24 | 6 | 24 | 8 | 24 |
| 12 | 8 | 32 | 8 | 32 | 8 | 28 | 8 | 32 | 8 | 34 | 8 | 34 |
| 14 | 8 | 34 | 10 | 34 | 10 | 32 | 10 | 34 | 8 | 34 | 8 | 34 |
| 16 | 12 | 36* | 12 | 36 | 12 | 34 | 12 | 36 | 10 | 38 | 10 | 34 |
| 18 | 14 | 50 | 14 | 40 | 14 | 40 | 14 | 40 | 14 | 40 | 14 | 40 |
| 20 | 16 | 56 | 16 | 48 | 16 | 48 | 16 | 50 | 16 | 52 | 14 | 56 |
| 22 | 18 | 58 | 18 | 56 | 18 | 50 | 18 | 56 | 18 | 58 | 18 | 58 |
| 24 | 18 | 60 | 20 | 58 | 20 | 54 | 20 | 58 | 18 | 60 | 20 | 60 |
| 26 | 20 | 60 | 20 | 60 | 20 | 58 | 22 | 60 | 20 | 62 | 20 | 60 |
| 28 | 22 | 64* | 22 | 62 | 24 | 60 | 24 | 64 | 22 | 64 | 22 | 62 |
| 30 | 26 | 78 | 26 | 70 | 26 | 68 | 26 | 74 | 24 | 70 | 26 | 74 |
| 32 | 28 | 82 | 28 | 76 | 28 | 76 | 30 | 78 | 28 | 78 | 28 | 78 |
| 34 | 32 | 86 | 30 | 80 | 30 | 80 | 32 | 82 | 30 | 82 | 30 | 82 |
| 36 | 34 | 90 | 32 | 84 | 34 | 82 | 34 | 84 | 32 | 88 | 32 | 88 |
| 38 | 34 | 94 | 34 | 88 | 36 | 82 | 36 | 88 | 34 | 94 | 34 | 94 |
| 40 | 38 | 94 | 36 | 92 | 36 | 84 | 38 | 94 | 36 | 96 | 36 | 96 |
| 42 | 40 | 96* | 40 | 94 | 40 | 88 | 40 | 96 | 38 | 98 | 38 | 96 |
| 44 | 42 | 110 | 42 | 98 | 42 | 92* | 42 | 104 | 40 | 106 | 42 | 98 |
| 46 | 42 | 124 | 44 | 106 | 44 | 100 | 44 | 110 | 42 | 112 | 42 | 112 |
| 48 | 44 | 126 | 46 | 114 | 46 | 110 | 46 | 122 | 44 | 118 | 44 | 118 |

**Table 3.2:** (continued)

| Z | SkM* | | SkP | | SLy4 | | SV-min | | UNEDF0 | | UNEDF1 | |
|---|---|---|---|---|---|---|---|---|---|---|---|---|
| 50 | 50 | 126 | 50 | 122 | 52 | 124 | 52 | 124 | 48 | 124 | 48 | 124 |
| 52 | 56 | 126 | 56 | 124 | 56 | 126 | 56 | 126 | 54 | 126 | 54 | 126 |
| 54 | 58 | 126 | 58 | 126 | 58 | 126 | 58 | 126 | 56 | 126 | 56 | 126 |
| 56 | 60 | 132 | 60 | 126 | 60 | 126 | 60 | 126 | 60 | 132 | 58 | 126 |
| 58 | 60 | 144 | 62 | 130 | 60 | 126 | 62 | 128 | 60 | 136 | 60 | 128* |
| 60 | 64 | 146 | 64 | 134 | 64 | 126 | 64 | 128* | 62 | 142 | 62 | 136 |
| 62 | 68 | 152 | 68 | 136 | 68 | 126* | 68 | 146 | 66 | 148 | 66 | 146 |
| 64 | 70 | 156 | 70 | 144 | 70 | 128* | 70 | 150 | 70 | 154 | 68 | 154 |
| 66 | 74 | 160* | 72 | 148 | 72 | 148 | 74 | 154 | 72 | 158 | 72 | 156 |
| 68 | 76 | 164* | 76 | 152 | 76 | 154 | 76 | 158 | 76 | 162 | 74 | 162 |
| 70 | 80 | 176* | 80 | 156 | 78 | 158 | 80 | 162* | 78 | 166 | 78 | 166 |
| 72 | 82 | 184 | 82 | 160 | 80 | 160 | 82 | 170* | 80 | 182 | 80 | 176* |
| 74 | 84 | 184 | 84 | 164 | 84 | 166 | 84 | 184 | 82 | 184 | 82 | 184 |
| 76 | 88 | 184 | 88 | 174* | 86 | 172* | 88 | 184 | 86 | 184 | 86 | 184 |
| 78 | 92 | 184 | 92 | 182 | 90 | 184 | 92 | 184 | 90 | 184 | 90 | 184 |
| 80 | 96 | 184 | 94 | 184 | 94 | 184 | 96 | 184 | 92 | 184 | 94 | 184 |
| 82 | 102 | 186 | 102 | 184 | 100 | 184 | 102 | 184 | 96 | 184 | 96 | 184 |
| 84 | 108 | 192* | 106 | 184 | 106 | 184 | 104 | 184 | 106 | 186 | 102 | 186 |
| 86 | 112 | 208 | 108 | 186 | 110 | 184 | 110 | 186 | 108 | 188* | 106 | 186 |
| 88 | 118 | 214 | 112 | 200 | 112 | 184 | 112 | 188* | 110 | 208 | 110 | 208 |
| 90 | 122 | 220 | 118 | 206 | 116 | 184* | 118 | 210 | 114 | 212 | 114 | 212 |
| 92 | 126 | 222 | 122 | 210 | 120 | 186* | 122 | 214 | 120 | 216 | 118 | 216 |
| 94 | 128 | 226* | 126 | 214 | 124 | 208 | 126 | 218 | 124 | 220* | 122 | 220* |
| 96 | 130 | 234* | 128 | 218 | 126 | 214 | 130 | 220 | 128 | 226* | 128 | 226* |
| 98 | 132 | 246* | 132 | 222 | 130 | 218 | 130 | 228* | 130 | 232* | 130 | 230* |
| 100 | 138 | 258* | 134 | 228 | 134 | 220 | 136 | 230* | 134 | 236* | 132 | 234* |

**Table 3.2:** (continued)

| Z | SkM* | | SkP | | SLy4 | | SV-min | | UNEDF0 | | UNEDF1 | |
|---|---|---|---|---|---|---|---|---|---|---|---|---|
| 102 | 142 | 258 | 140 | 232 | 136 | 222 | 140 | 234* | 138 | 240* | 134 | 258 |
| 104 | 146 | 258 | 144 | 236 | 142 | 230 | 144 | 256 | 142 | 258 | 140 | 258 |
| 106 | 150 | 258 | 148 | 244* | 146 | 232* | 148 | 258 | 146 | 258 | 146 | 258 |
| 108 | 156 | 266 | 152 | 250* | 152 | 234* | 152 | 258 | 150 | 258 | 150 | 258 |
| 110 | 160 | 274 | 156 | 258 | 156 | 250 | 158 | 258 | 154 | 258 | 154 | 258 |
| 112 | 162 | 278 | 160 | 258 | 160 | 252* | 160 | 258 | 158 | 258 | 158 | 258* |
| 114 | 166 | 280* | 164 | 258 | 162 | 258 | 164 | 258* | 162 | 260 | 160 | 260* |
| 116 | 170 | 284* | 168 | 260* | 166 | 258 | 168 | 260* | 166 | 260 | 164 | 260* |
| 118 | 172 | 284* | 172 | 262* | 170 | 258 | 172 | 260* | 168 | 262* | 168 | 282* |
| 120 | 178 | 298 | 174 | 276 | 174 | 258* | 176 | 282 | 172 | 290 | 172 | 288* |

# Chapter 4

# The Landscape of Two-Proton Radioactivity

This chapter is revised based on the following published works:

- E. Olsen, M. Pfützner, N. Birge, M. Brown, W. Nazarewicz, and A. Perhac, "Landscape of Two-Proton Radioactivity", *Phys. Rev. Lett.* **110**, 222501 (2013).
- E. Olsen, M. Pfützner, N. Birge, M. Brown, W. Nazarewicz, and A. Perhac, "Erratum: Landscape of Two-Proton Radioactivity [Phys. Rev. Lett. 110, 222501 (2013)]", *Phys. Rev. Lett.* **111**, 139903 (2013).

My primary contributions to these papers can be found in Chapter 10.

## 4.1 Introduction

With the impressive progress in mapping new territories in the nuclear landscape, new phenomena emerge in rare isotopes with extreme proton-to-neutron imbalance. On the proton-rich side of the nuclear chart, due to the presence of the Coulomb barrier that has a confining effect on the nucleonic density, relatively long lived

proton emitters exist beyond the proton-drip line [110–113]. In recent decades, the phenomenon of proton emission from odd-Z nuclei in this region has been developed into a powerful spectroscopic tool yielding a wealth of detailed structure information [110]. In cases where single proton emission is either energetically forbidden or strongly suppressed due to proton pairing, an unbound even-Z nucleus may undergo a simultaneous emission of two protons [114]. Which nuclei are able to undergo two-proton ($2p$) emission?

While the idea of ground state $2p$ radioactivity was theorized in 1960, it wasn't until 2002 that it was experimentally observed in $^{45}$Fe [115, 116] and then later in $^{19}$Mg [117, 118], $^{48}$Ni [119], and $^{54}$Zn [120, 121]. Interest in the phenomenon of $2p$ radioactivity has increased significantly due to the measurement of proton-proton correlations in the decay of $^{45}$Fe [122], revealing both the three-body nature of the process and its sensitivity to the angular momentum composition of the wave function. These findings were corroborated by recent studies of $2p$ correlations in the decay of $^{6}$Be resonances [123, 124].

Most theoretical work on $2p$ radioactivity has centered around finding the best $2p$ emitting candidates for experimental observation and has thus focused on a rather narrow range of nuclei with $22 < Z < 30$ [125–129]. Motivated by astrophysical applications, this region was later extended to $30 < Z < 38$ [130]. This begs the question: is $2p$ radioactivity just a property of light and medium mass nuclei, or does it occur in heavy systems as well?

Two-proton decay can happen either sequentially ($pp$) or simultaneously ($2p$). To undergo true $2p$ decay, a nucleus must satisfy the following conditions:

$$Q_{2p} = -S_{2p} > 0, \quad Q_p = -S_p < 0. \tag{4.1}$$

In this case single proton emission is forbidden, so the only decay path is simultaneous two-proton decay (see the inset of Figure 4.1). For sequential $pp$ decay, a nucleus must satisfy:

$$Q_{2p} > 0, \quad Q_{2p} > Q_p > 0. \tag{4.2}$$

To maximize the number of true $2p$ emitters we could find, we used the less stringent criteria [110]:

$$Q_{2p} > 0, \quad Q_p < \frac{1}{5} Q_{2p}, \tag{4.3}$$

for which single proton decay is strongly suppressed, but not forbidden. To find sequential $pp$ emitters, we used:

$$Q_{2p} > 0, \quad Q_{2p} > Q_p > \frac{1}{5} Q_{2p}. \tag{4.4}$$

The $Q$ values were calculated using mass table binding energy and pairing gap data from HFBTHO. The binding energies of odd-$N$ and odd-$Z$ systems were obtained by adding the averages of the neighboring even-even binding energies and pairing gaps. Considering the uncertainties of current approaches to odd-even binding energy differences [67], this was a reasonable procedure. For the EDFs used in this work, the rms deviation from experimental $S_{2p}$ values was typically less than 1 MeV. For instance, for UNEDF0 and UNEDF1, it was 0.86 and 0.79 MeV, respectively [50].

For nuclei which satisfied equations 4.3 or 4.4, we calculated their $2p$ half-lives and applied the following selection criteria:

$$10^{-7}\text{s} < T_{2p} < 10^{-1}\text{s}, \tag{4.5}$$

which defines the feasibility of experimental observation of $2p$ decay. The lower bound of 100 ns corresponds to the typical sensitivity limit of in-flight, projectile fragmentation techniques [113]. The upper bound of 100 ms ensures that $2p$ decay will not be dominated by $\beta$ decay (we note that the half-lives of the observed medium-mass $2p$ emitters are all in the range of several ms).

The half-lives for $2p$ decay were estimated using two simple models. The first, the direct-decay model, results from the factorization of the decay amplitude into a product of two-body terms [131]. The removal of one proton leaves the core+p system in a state of energy $E_p$, relative to the three-body decay threshold, and requires a transfer of orbital angular momentum $l_p$. The core+p system is taken here as the ground state of the one-proton daughter:

$$E_p = Q_{2p} - Q_p,$$

where $Q_{2p}$ and $Q_p$ denote the decay energies for $2p$ and single-proton emission, respectively. All of our calculations were made with $l_p = 0$, i.e., assuming the fastest decay possible. In this way, we establish a limit of the least neutron deficient nuclei decaying by $2p$ emission. We note, however, that inclusion of larger values of angular momentum, in particular $l_p = 1$, known to occur around $Z = 28$, would increase the number of predicted candidates.

To calculate the $2p$-decay lifetimes, the following formula was used:

$$T_{2p} = \frac{\hbar \ln(2)}{\Gamma_{2p}}, \tag{4.6}$$

where $\Gamma_{2p}$ is the partial decay width. To determine $\Gamma_{2p}$, we used the expression given in equation (20) of Ref. [113]. The spectroscopic factor $\theta^2$ in this expression was determined by comparison with the experimentally established four $2p$ emitters shown in Table 4.1. Using the experimental separation energies, the average value $\theta^2 = 0.173$ was obtained and used in subsequent calculations.

The diproton model assumes that both protons leave the core nucleus as a correlated $2p$ pair with $l = 0$. Within this model [125, 127], the $2p$-decay width is given by the Wentzel-Kramers-Brillouin (WKB) expression given in equation (12) of Ref. [127]. In our calculations, the average diproton potential has been approximated by $2V_p(r)$, where $V_p$ is the average proton potential containing the Woods-Saxon field in the Chepurnov parameterization [132] and the Coulomb term (the results are fairly

**Table 4.1:** Experimental partial $2p$ half-lives used to optimize the spectroscopic factors and the resulting predictions of the direct-decay and diproton models. In the direct model, $l_p = 0$ was assumed.

| Nucleus | Experiment | direct | diproton |
|---|---|---|---|
| $^{19}$Mg | 4.0(15) ps | 6.2 ps | 12.3 ps |
| $^{45}$Fe | 3.7(4) ms | 1.1 ms | 8.7 ms |
| $^{48}$Ni | $3.0^{+2.2}_{-1.2}$ ms | 6.8 ms | 5.3 ms |
| $^{54}$Zn | $1.98^{+0.73}_{-0.41}$ ms | 1.0 ms | 0.8 ms |

insensitive to the choice of the average potential [127]). The diproton spectroscopic factor can be estimated in the cluster overlap approximation [125]:

$$\theta^2_{\rm dipr} = G^2 \left[\frac{A}{A-2}\right]^{2n} \mathcal{O}^2, \tag{4.7}$$

where [133]

$$G^2 = \frac{(2n)!}{2^{2n}(n!)^2},$$

$n$ is the average principal proton oscillator quantum number defined as [19]

$$n \approx (3Z)^{1/3} - 1,$$

and $\mathcal{O}^2$ is the proton overlap function. The value of $\mathcal{O}^2 = 0.015$ was determined by a $\chi^2$ optimization to the experimental half-lives of $^{19}$Mg, $^{45}$Fe, $^{48}$Ni, and $^{54}$Zn. The values of the half-lives of these nuclei predicted by the diproton model are given in Table 4.1; they are consistent with the direct-decay model and the estimates of Refs. [131, 134].

For nuclei which satisfied equation 4.5, we calculated their $\alpha$ decay lifetimes and applied the following selection criteria:

$$T_{2p} < 10 T_\alpha. \tag{4.8}$$

This condition guarantees that the $2p$-decay branch is at least 10% (this was done to eliminate fast $\alpha$ emitters from our considerations). Of these candidates, to select where the competition between $2p$ and $\alpha$ decay can be seen, we used the criterion

$$0.1T_{2p} < T_{\alpha} < 10T_{2p}, \tag{4.9}$$

which ensures that the branching ratio for either $2p$ or $\alpha$ decay is at least 10%. The $\alpha$-decay half-lives were obtained from the global phenomenological expression of equation (13) in Ref. [135].

## 4.2 Results

For each EDF considered in this work, we selected candidates for $2p$ emission according to the imposed criteria on lifetimes given by equations (4.5) and (4.8). We define the model multiplicity $m(Z,N) = k$ where a nucleus $(Z,N)$ is predicted by $k$ EDFs ($k = 1, ..., 6$) to be a $2p$ emitter. The average path for $2p$ emission in the $(Z,N)$ plane is given by $N_{\rm av}(Z)$, where, for a given element $Z$, the model averaged neutron number is

$$N_{\rm av}(Z) = \frac{\sum_N N m(Z,N)}{\sum_N m(Z,N)}, \tag{4.10}$$

provided that at least one candidate has been found for this $Z$.

Figure 4.1 shows the trajectories $N_{\rm av}(Z)$ for both the diproton (true $2p$) and direct (true $2p$ and sequential $pp$) decay models. It is seen that (i) both ways of estimating $2p$ half-lives give very similar predictions for the average path of $2p$ radioactivity (up until $Z = 52$ where true $2p$ decay is calculated to end) and (ii) this path quickly departs from the two-proton drip line with increasing atomic number. We also find candidates for sequential $pp$ emission in every even-Z isotope above Te, except in Xe, where $\alpha$ decay dominates. Furthermore, according to our calculations, $\alpha$ decay wins over $2p$ emission in nuclei above lead, so $Z = 82$ marks the upper bound of the ground

state $2p$ emission landscape. The intermodel consistency for our predicted $Q_{2p}$ values along $N_{\rm av}(Z)$ is quite good; namely, the rms deviation for our six EDFs is typically 150 keV, well below the average deviation from experiment.

Results of our survey are presented in more detail in Figure 4.2. We see that each element between nickel and tellurium has isotopes expected to undergo true $2p$ radioactivity. For three light elements ($Z$ = 20, 24, and 26) no $2p$ candidates were predicted because the calculated half-lives were shorter than the lower limit of condition (4.5), which is a consequence of our restriction to the $l = 0$ decay channel. We note that the observed $2p$ decay of $^{45}$Fe is dominated by the $l = 1$ channel [113]. While the nuclei $^{54}$Zn, $^{59}$Ge, $^{63}$Se, and $^{71}$Sr discussed in [130] are generally expected to meet the energy criteria of equation 4.3, their predicted $Q_{2p}$ values are too low to meet the lifetime criteria of equation 4.5. In general, due to large uncertainties in the calculated half-lives because of uncertainties in $Q_{2p}$ [134], the estimated error on the predicted neutron number of a $2p$ emitter is $\Delta N = 1$.

In the region beyond $^{54}$Zn, the predicted $2p$ candidates which are closest to the current experimental reach and predicted by both the direct and diproton models are $^{57}$Ge(3), $^{62}$Se(2), $^{66}$Kr(3), and $^{103}$Te(2), where the numbers in parentheses indicate the corresponding number of neutrons beyond the most neutron-deficient isotope known to date. All other cases, including the sequential $pp$ emitters, are located by more than 3 neutrons away from the present body of known isotopes. This distance increases with atomic number and reaches 14 neutrons for $^{165}$Pb, which is predicted to be the $pp$ emitting lead isotope closest to the drip line. Other best candidates for ground state $2p$ radioactivity in heavy nuclei (according the the direct-decay model) are $^{127}$Gd, $^{135}$Er, $^{153}$Os, and $^{164}$Pb; each of these nuclei was predicted to be a sequential $pp$ emitter by all six EDFs.

In a few cases, competition between $2p$ emission and $\alpha$ decay is predicted. The two best candidates, predicted by at least two mass models, are $^{103}$Te and $^{145}$Hf. The nucleus $^{103}$Te appears as one of the most interesting cases in our survey: two EDFs (SV-min and UNEDF1) predict the competition between $\alpha$ decay and true

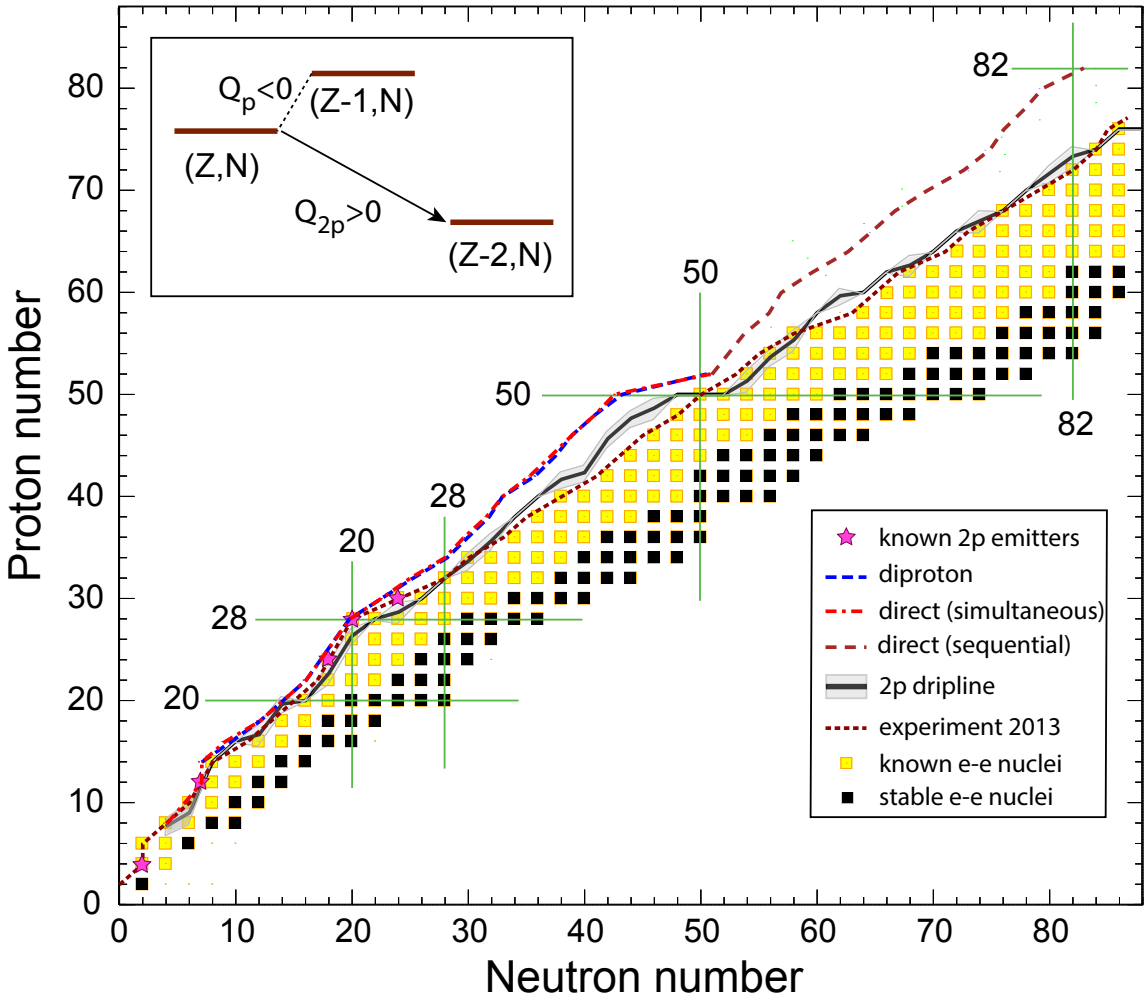


**Figure 4.1:** The landscape of ground state $2p$ emitters. The mean two-proton drip line (thick black line) and its uncertainty (grey) were obtained from Ref [59]. The known proton-rich even-even nuclei are marked by yellow squares, stable even-even nuclei by black squares, and known $2p$ emitters by stars. The current experimental reach for even-Z nuclei (including odd-A systems) [136, 137] is marked by a dotted line. The average lines $N_{\rm av}(Z)$ of true $2p$ decay for the diproton (dashed blue line) and direct-decay (dash-dotted red line) models are shown, as well as the average line of sequential ($pp$) decay for the direct-decay model (dashed brown line). The energetic condition for true $2p$ decay is illustrated in the inset.

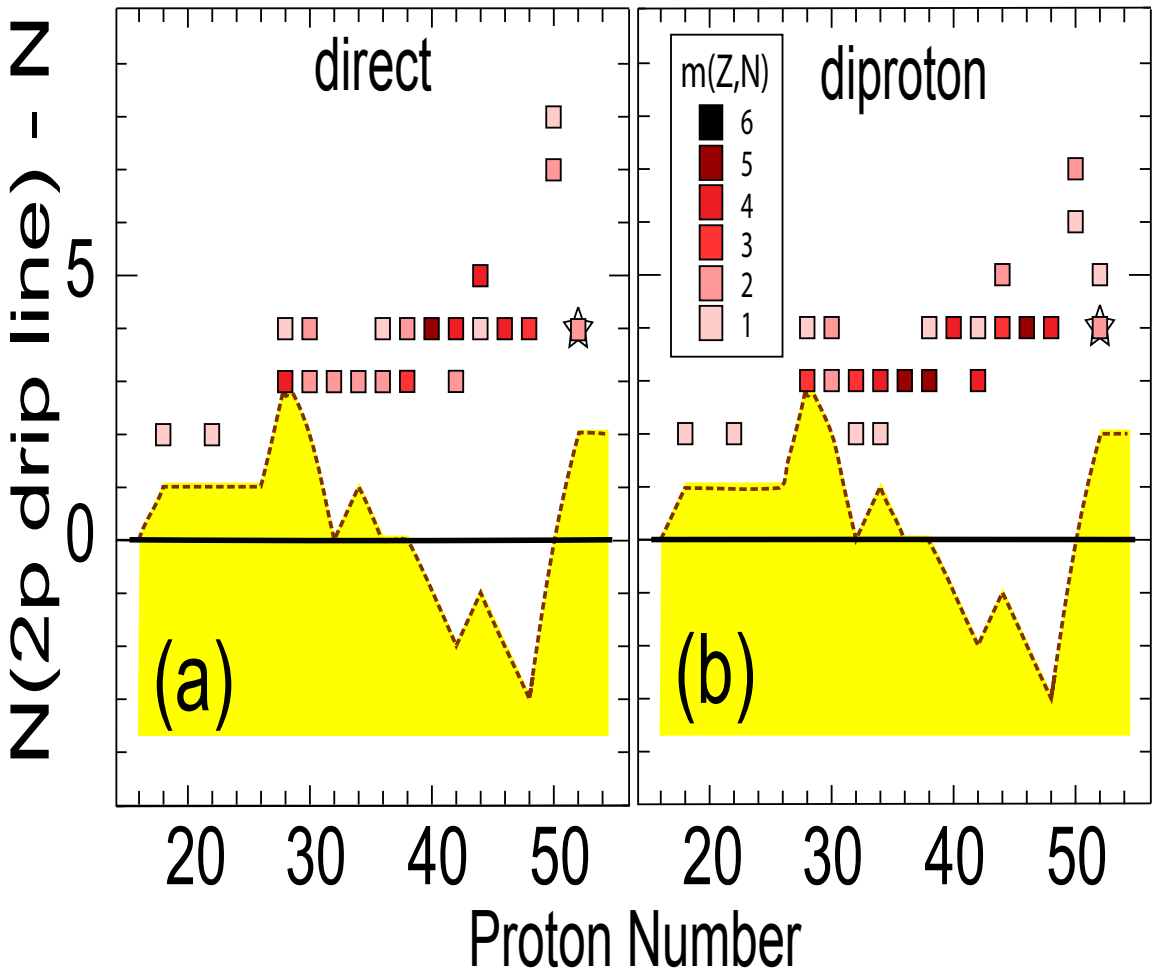


**Figure 4.2:** The predictions of the direct-decay (a) and diproton (b) models for true ground state $2p$ radioactivity. For each value of $Z \geq 18$, neutron numbers $N$ of predicted two-proton emitters are shown relative to the average two-proton drip line of Ref [59] shown in Figure 4.1. The model multiplicity $m(Z, N)$ is indicated by the legend. The candidates for competing $2p$ and $\alpha$ decay are marked by stars. The current experimental reach of Figure 4.1 is marked by a dotted line.

$2p$ radioactivity, one EDF (SLy4) predicts the competition between $\alpha$ decay and sequential $pp$ decay, and one EDF (SkM*) predicts the dominance of $\alpha$ decay. In $^{145}$Hf, $\alpha$ decay is predicted to compete with sequential $pp$ emission.

## 4.3 Conclusion

In this theoretical survey we quantified the landscape of $2p$ radioactivity. We used two different decay models and six different EDFs to assess model-dependent extrapolations beyond the two-proton drip line. Most importantly, we found that this decay mode is not an isolated phenomenon, limited to a narrow range of light and medium mass nuclei, but a typical feature for proton-unbound isotopes with even atomic numbers. According to our calculations, almost all elements between argon and lead have $2p$-decaying isotopes. The upper end of the $2p$ decay territory is determined by $\alpha$ decay, which totally dominates above $Z = 82$.

Unfortunately, most of the new candidates for $2p$ radioactivity are located far beyond the current experimental reach. Only in two regions is the $2p$-decay mode predicted to occur closely enough to be addressed by today's experiments. One ranges from germanium to krypton, and the other is located just above tin. Other regions will have to wait for the facilities of the next generation. A confrontation of our predictions for heavier $2p$ emitters with future data will be of great value for modeling of proton-unstable nuclei and improving the nuclear EDF.

Perhaps the most interesting case studied was $^{103}$Te, in which the competition between $2p$ emission and $\alpha$ decay is predicted. The observation of these two decay modes in the same nucleus would provide an excellent test of nuclear structure models and a deeper understanding of the dynamics of charged particle emission from nuclei.

Finally, we note that all EDFs employed in our study yield a similar range of $2p$ radioactivity. While details for individual nuclei differ because of the high sensitivity of $2p$ and $\alpha$ decay half-lives to predicted $Q$ values, the global trends presented in this survey seem to be fairly robust.

# Chapter 5

# Neutron-skin Uncertainties

This chapter is revised based on the following published work:

- M. Kortelainen, J. Erler, W. Nazarewicz, N. Birge, Y. Gao, and E. Olsen, "Neutron-Skin Uncertainties of Skyrme Energy Density Functionals", *Phys. Rev. C.* **88**, 031305 (2013).

My primary contributions to this paper can be found in Chapter 10.

## 5.1 Introduction

The journey through the unexplored regions of the nuclear chart, especially on the neutron-rich side, is not going to be easy, but the scientific payoff promises that it will be well worth it [138]. A major objective of this quest will be to explain neutron-rich matter in both the laboratory and the cosmos across a wide range of nucleonic densities.

In heavy neutron-rich nuclei, the excess of neutrons gives rise to a neutron skin, characterized by the neutron distribution extending beyond the proton distribution. The skin can be characterized by its thickness, which is commonly defined in terms of the difference of rms radii:

$$r_{\rm skin} = \langle r_n^2 \rangle^{1/2} - \langle r_p^2 \rangle^{1/2}. \tag{5.1}$$

As discussed in Ref. [139], it is better to define the neutron skin through neutron and proton diffraction radii and surface thicknesses. However, for well-bound nuclei, which do not exhibit halo features, the above definition of $r_{\rm skin}$ is practically equivalent [140].

Neutron-skin thickness has been found to correlate with a number of observables in finite nuclei related to isovector nuclear fields [72, 141–146]. Furthermore, it has a close connection to the neutron matter equation of state (EOS) and properties of neutron stars [51, 72, 142, 147–159]. In this context, precise experimental data on $r_{\rm skin}$ are crucial for constraining the poorly known isovector sector of nuclear structure models.

Various experimental probes have been used to determine $r_{\rm skin}$ [139, 143, 160]. The Lead Radius Experiment (PREX) recently measured the parity-violating asymmetry coefficient $A_{\rm PV}$ for $^{208}$Pb [161], which yielded $r_{\rm skin} = 0.33^{+0.16}_{-0.18}$ [162]. Unfortunately, the experimental error bar of PREX is too large to provide any practical constraint on well calibrated theoretical models [143]. At present, the most precisely determined [163] isovector indicator in heavy nuclei is the electric dipole polarizability $\alpha_D$ in $^{208}$Pb [73, 143], which has been used to put constraints on the $r_{\rm skin}$ of $^{208}$Pb [143, 163].

Many new measurements of isovector quantities are currently in development. PREX-II [164] (a follow-up measurement to PREX) has been designed to improve the experimental precision of neutron-skin thickness to 0.06 fm. A Calcium Radius Experiment (CREX) measurement of the neutron skin in $^{48}$Ca [165] is promising an unprecedented precision of 0.02 fm. Last but not least, on-going experimental studies of $\alpha_D$ in several neutron-rich nuclei [166] will soon provide key data.

To help determine a benchmark for the precision of future experiments on $r_{\rm skin}$ which aim at informing theory about isovector properties of effective nuclear

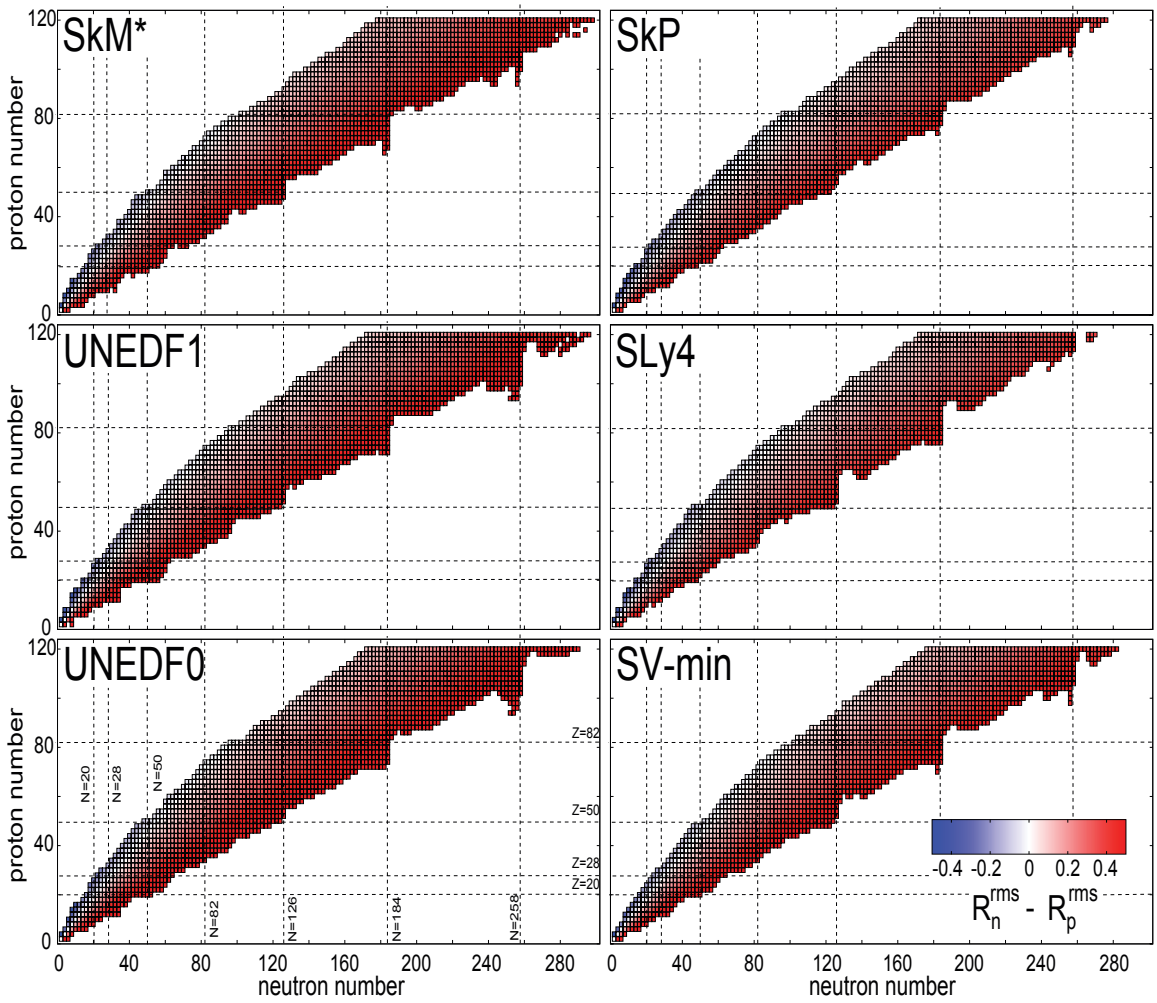


**Figure 5.1:** Survey of neutron skin radii calculated for all six EDFs: SkM*, SkP, UNEDF1, SLy4, UNEDF0, and SV-min.

interactions it is necessary to calculate the value of $r_{\text{skin}}$ for as many nuclei as possible. For this task mass table proton and neutron radii of HFBTHO were used.

## 5.2 Results

The $r_{\text{skin}}$ values of each individual EDF [59] are displayed in Figure 5.1. The first thing we notice is the EDFs considered give very consistent answers when it comes to $r_{\text{skin}}$ despite their different optimization strategies. We also notice a smooth transition from proton skins ($r_{\text{skin}} < 0$) in proton-rich nuclei to pronounced neutron skins in

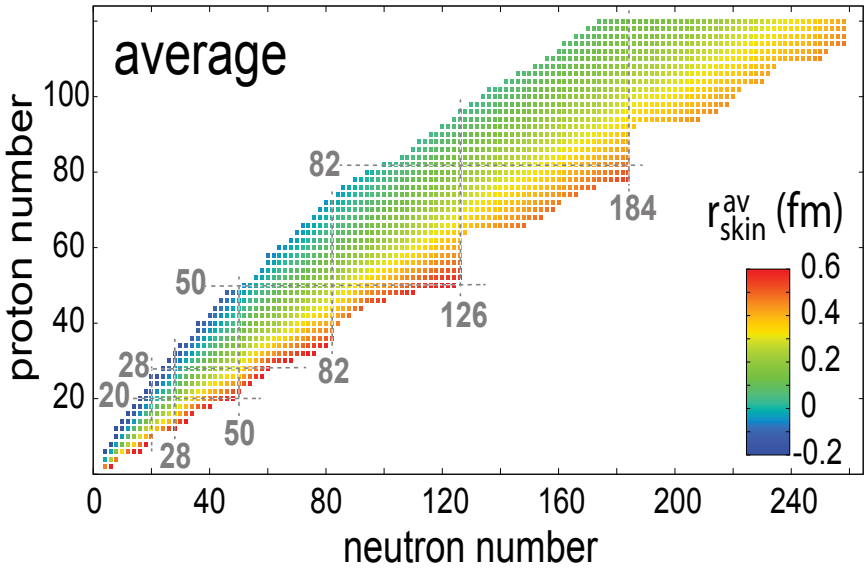


**Figure 5.2:** The model-average value of $r_{\rm skin}$ for the six EDFs used in Figure 5.1.

neutron-rich nuclei. This is seen further in Figure 5.2, where the mean values of $r_{\rm skin}$ are shown. As expected, the average value of the neutron-skin thickness $r_{\rm skin}^{\rm av}$ increases steadily with $N$ for each isotopic chain [139, 160].

The systematic error $\Delta r_{\rm skin}^{\rm syst}$ of these values also increases gradually when approaching the neutron drip line. However, the range of $\Delta r_{\rm skin}^{\rm syst}$ is surprisingly small: the model spread does not exceed 0.05 fm for extremely neutron-rich systems, a fact reflected by the consistency of the results between EDFs. To get a deeper insight into the error contributions of $\Delta r_{\rm skin}^{\rm syst}$ the deviation of $r_{\rm skin}$ values from $r_{\rm skin}^{\rm av}$ were studied for all six EDFs. It was found that SV-min had the least deviation while SkP and UNEDF0 showed large deviations below and above the average respectively. By inspecting the NMPs of these EDFs [49–51, 167] we found that the low $r_{\rm skin}$ values of SkP can be partly attributed to its value of the slope of the symmetry energy, $L = 19.7$ MeV (as compared to $L = 44.8$ MeV for SV-min). Still, the parameter $L$ cannot be the whole story, as its value for UNEDF0 ($L = 45.1$ MeV) is very close to that of SV-min.

The statistical error $\Delta r_{\rm skin}^{\rm stat}$ of $r_{\rm skin}$ was also studied through the isotopic chains of Ca, Zr, Er, and Z=120. Using UNEDF0 and SV-min it was found that similarly

**Table 5.1:** Theoretical uncertainties on $r_{\rm skin}$ in $^{208}$Pb and $^{48}$Ca (in fm). Shown are the statistical errors of UNEDF0 and SV-min and the errors of PREX [161] and planned PREX-II [164] and CREX [165] experiments.

| Nucleus | $\Delta r_{\rm skin}^{\rm stat}$ | | Experiment |
|---|---|---|---|
| | UNEDF0 | SV-min | |
| $^{208}$Pb | 0.058 | 0.037 | 0.18 [161], 0.06[164] |
| $^{48}$Ca | 0.035 | 0.026 | 0.02 [165] |

to the systematic error $\Delta r_{\rm skin}^{\rm stat}$ propagates with $N$. The gradual growth of statistical error with neutron excess is primarily caused by isovector coupling constants of the functional that are poorly constrained by current data. The $\Delta r_{\rm skin}^{\rm stat}$ values were also found to be significantly larger than the systematic error (reaching as high as 0.14 fm) with dominant error contributions coming from $L$ and $a_{\rm sym}$. The contribution from $L$ was by far the largest in all the isotopes and yielded over 50% of the total error (the strong impact of $L$ on the statistical error of neutron rms radii was also found in Ref. [74]).

To be able to advance theory, the uncertainty of an experimental measurement of $r_{\rm skin}$ must be less than its calculated theoretical statistical error. To find this necessary experimental accuracy the $\Delta r_{\rm skin}^{\rm stat}$ values of $^{208}$Pb and $^{48}$Ca were calculated for UNEDF0 and SV-min and are shown in Table 5.1. The error bar of PREX [161] is unfortunately too large ($\sim$0.18 fm) to provide a useful constraint on isovector properties of current models. Similarly, the error bar of PREX-II [164] is very close but slightly too large (0.06 fm). The superb anticipated accuracy of the planned CREX experiment (0.02 fm) [165] will have an impact on reducing the statistical error on $r_{\rm skin}$.

## 5.3 Conclusion

This survey addresses systematic and statistical errors on neutron-skin thickness predicted by various Skyrme EDF parameterizations. Because $r_{\rm skin}$ has been found to strongly correlate with various isovector indicators, it provides an essential constraint

on nuclear EDFs that aim to make extrapolations into the *terra incognita* at the neutron-rich side of the nuclear landscape.

We found that the systematic error $\Delta r_{\rm skin}^{\rm syst}$ obtained in this work and in Ref. [143] is smaller than the statistical error $\Delta r_{\rm skin}^{\rm stat}$. As expected, both errors grow with neutron number due to the propagation of uncertainties of poorly determined EDF isovector coupling constants. It is important to note that the systematic error depends on the particular choice of EDFs used. For example, there is a systematic shift predicted in $r_{\rm skin}$ values between the Skyrme models studied in this work and relativistic EDFs [143, 145] whose values exceed $\Delta r_{\rm skin}^{\rm syst}$ obtained here.

The slope of the symmetry energy $L$ is the single main contributor to $\Delta r_{\rm skin}^{\rm stat}$. As pointed out in many previous studies, this parameter is strongly correlated with many isovector indicators. Therefore, planned precise measurements of $r_{\rm skin}$ will help in pinning down this crucial NMP. Conversely, if $L$ could be constrained by some other experimental data [159], this would also reduce model uncertainty on $r_{\rm skin}$.

# Chapter 6

# Reflection-Asymmetric Deformations in Nuclear Ground States

Some of the material in this chapter is based on the following published work:

- E. Olsen, J. Erler, W. Nazarewicz, and M. Stoitsov, "Reflection-Asymmetric Nuclear Deformations within the Density Functional Theory", *J. Phys. Conf. Ser.* **402**, 012034 (2012).

My primary contributions to this paper can be found in Chapter 10.

## 6.1 Introduction

One of the fundamental properties of the atomic nucleus is its shape. The DFT description of nuclei is performed in the reference frame of the nucleus (the intrinsic frame) in which it may acquire a deformed shape. How does this nuclear deformation occur and what effect does shape deformation have on ground state nuclear properties?

The concept of nuclear shape deformation is ultimately related to the spontaneous symmetry breaking effect known in many areas of physics. Microscopically, deformations are associated with quantum-mechanical states that are nearly degenerate in energy [168]. Such a hybridization in quantum systems leads to reduced stability where even an infinitely small perturbation can produce a transition in the system [169]. In the case of nuclei, such a perturbation can occur through the coupling between degenerate single-particle orbits and collective nuclear vibrations [170, 171].

The theoretical description of nuclear shapes is done through a multipole expansion of mass moments parameterized by spherical harmonics $Y_{\lambda\mu}(\theta, \phi)$. Each spherical harmonic is multiplied by a deformation parameter $\alpha_{\lambda\mu}$ [170]. While triaxial deformations ($\mu \neq 0$) are quite common in nuclear excited states [171–173] they are very rare in nuclear ground states (see Ref. [174]). As such, for our work we assume all deformations to be axially symmetric and set $\mu = 0$. Thus we use axial deformations $\beta_\lambda = \alpha_{\lambda 0}$.

Every isoscalar mass moment can be interpreted physically. The isoscalar monopole moment ($\lambda = 0$) corresponds to an expansion or contraction of the nuclear volume. Since the nucleus is highly incompressible [77] a constant volume is assumed and this moment is omitted. The isoscalar dipole moment ($\lambda = 1$) corresponds to a translation of the entire nucleus; by setting our origin to the center of mass of the system, this moment can safely be ignored. The isoscalar quadrupole moment ($\lambda = 2$) corresponds to an ellipsoidal deformation [77, 175] which can be prolate (positive) or oblate (negative). The isoscalar octupole moment ($\lambda = 3$) corresponds to a reflection-asymmetric or pear-shaped deformation [170, 176] and is the primary interest of this work (a visual of these deformations can be found in Figure 6.1). While quadrupole deformations are common in nuclear ground states (see Figure 6.2) octupole deformations are more concentrated into particular regions of the nuclear chart [170, 177].

To identify nuclei with ground state octupole deformations it is necessary to calculate the binding energies of as many nuclei as possible. For this task AxialHFB

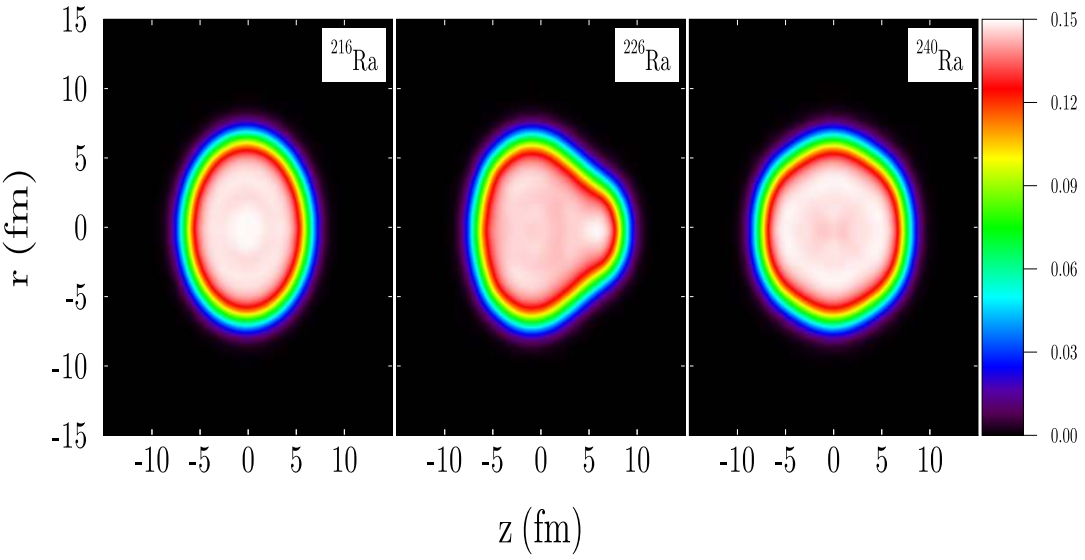


**Figure 6.1:** Nucleon density distributions (in cylindrical coordinates $r$ and $z$) calculated for $^{216}$Ra ($\beta_2 = 0.00$, $\beta_3 = 0.00$), $^{226}$Ra ($\beta_2 = 0.20$, $\beta_3 = 0.198$), and $^{240}$Ra ($\beta_2 = 0.24$, $\beta_3 = 0.00$) showing spherical, quadrupole, and octupole deformed shapes. All calculations were performed using the SLy4 functional.

was used in mass table calculations that recorded the binding energies and their associated quadrupole and octupole deformation parameters for even-even nuclei across the nuclear chart.

Information from the mass tables can also be used to evaluate the effect of octupole deformation on nuclear ground state properties. As binding energies encompass all of the interactions within a nucleus [178], differences between them (mass differences) can be used to isolate particular interactions. For example, separation energies (like $S_{2n}$ and $S_{2p}$) provide information on shell structure and phase transitions [179]. Through the double difference indicator $\delta V_{pn}$

$$\delta V_{pn} = \frac{1}{4}\Big[B(N,Z) - B(N-2,Z) - B(N,Z-2) + B(N-2,Z-2)\Big], \qquad (6.1)$$

the average interaction between the last two protons and the last two neutrons of an even-even nucleus can be obtained [179–181]. This quantity is meant to approximate

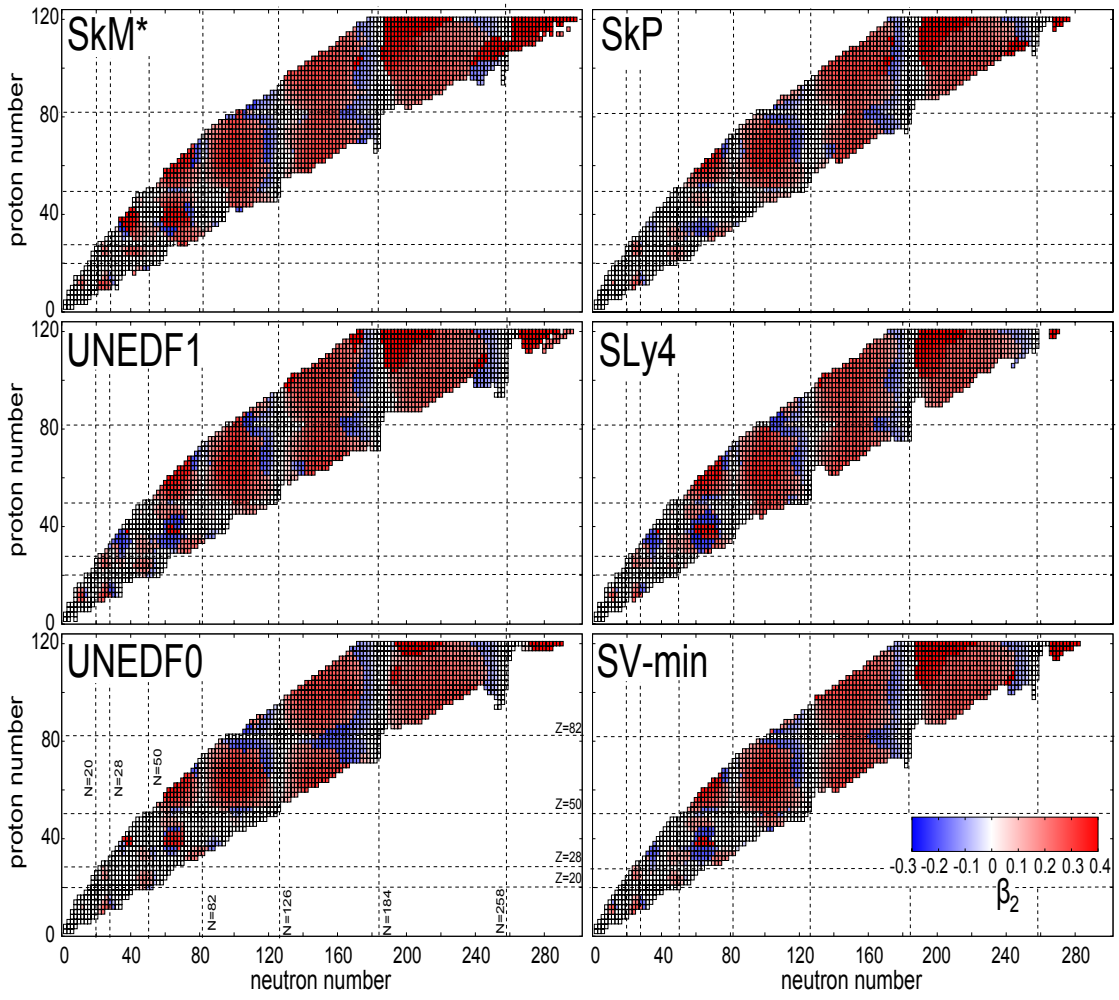


**Figure 6.2:** Predicted quadrupole moments from our HFBTHO mass table calculations [59].

the following mixed derivative [182]

$$\delta V_{pn} \approx \frac{\partial^2 B}{\partial Z \partial N}. \tag{6.2}$$

## 6.2 Preliminary Results

The results of our UNEDF0 mass table quadrupole and octupole deformations for nuclear ground states are shown in Figure 6.3. The quadrupole deformations from HFBTHO are shown to compare with those obtained from AxialHFB. The difference in neutron borders between (a) and (b) is due to the fact that AxialHFB calculations do not include re-entrant nuclei (see Chapter 3). As seen from the figure, both codes give very similar results despite the inclusion of octupole deformations in the solutions of AxialHFB. This implies that the octupole deformation has very little effect on the quadrupole moment. The lack of quadrupole deformation at $N = 50$, 82, 126, 184, and 258 is indicative of shell closure. The octupole deformations shown in (c) are predicted to be concentrated in the lanthanides and actinides; this result is quite expected [170, 183]. These deformations are also predicted to extend into superheavy systems (particularly in the proton-rich region) as has been seen before [184].

The initial results of our mass filter calculations are shown in Figure 6.4. Since we wanted to analyze the effect of octupole deformation on quadrupole deformation, we performed separate calculations for each binding energy used in the mass filters with the SLy4 EDF that found not only the unconstrained minima of all $\beta_2$ and $\beta_3$ points chosen, but also the minima for when $\beta_3$ was constrained to be zero. Such an analysis was not performed for UNEDF0, as we didn't record the minima for when $\beta_3$ was constrained to be zero; this will be done in future work.

The isotopes of radium and thorium serve as useful test cases, as it is well established that they contain octupole deformations [186–189]. Looking at the top graph, it is seen that the octupole deformation maximizes around $N = 138$ and then gradually decreases with neutron number. The effect of the octupole deformation on

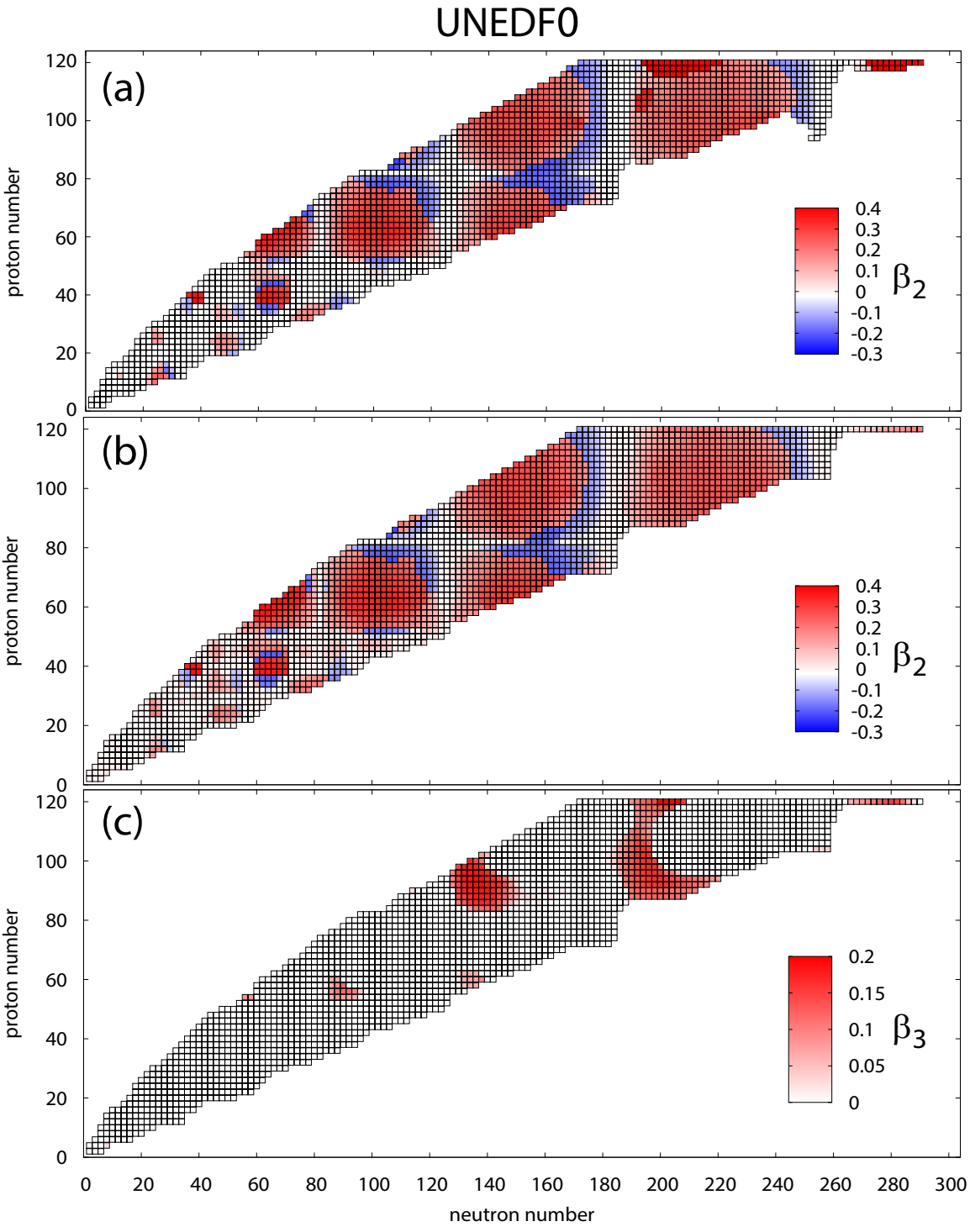


**Figure 6.3:** (a) The quadrupole deformations of the UNEDF0 mass table of HFBTHO (taken from Figure 6.2). (b) The quadrupole deformations of the UNEDF0 mass table of AxialHFB. (c) Similar to (b) but for octupole deformations.

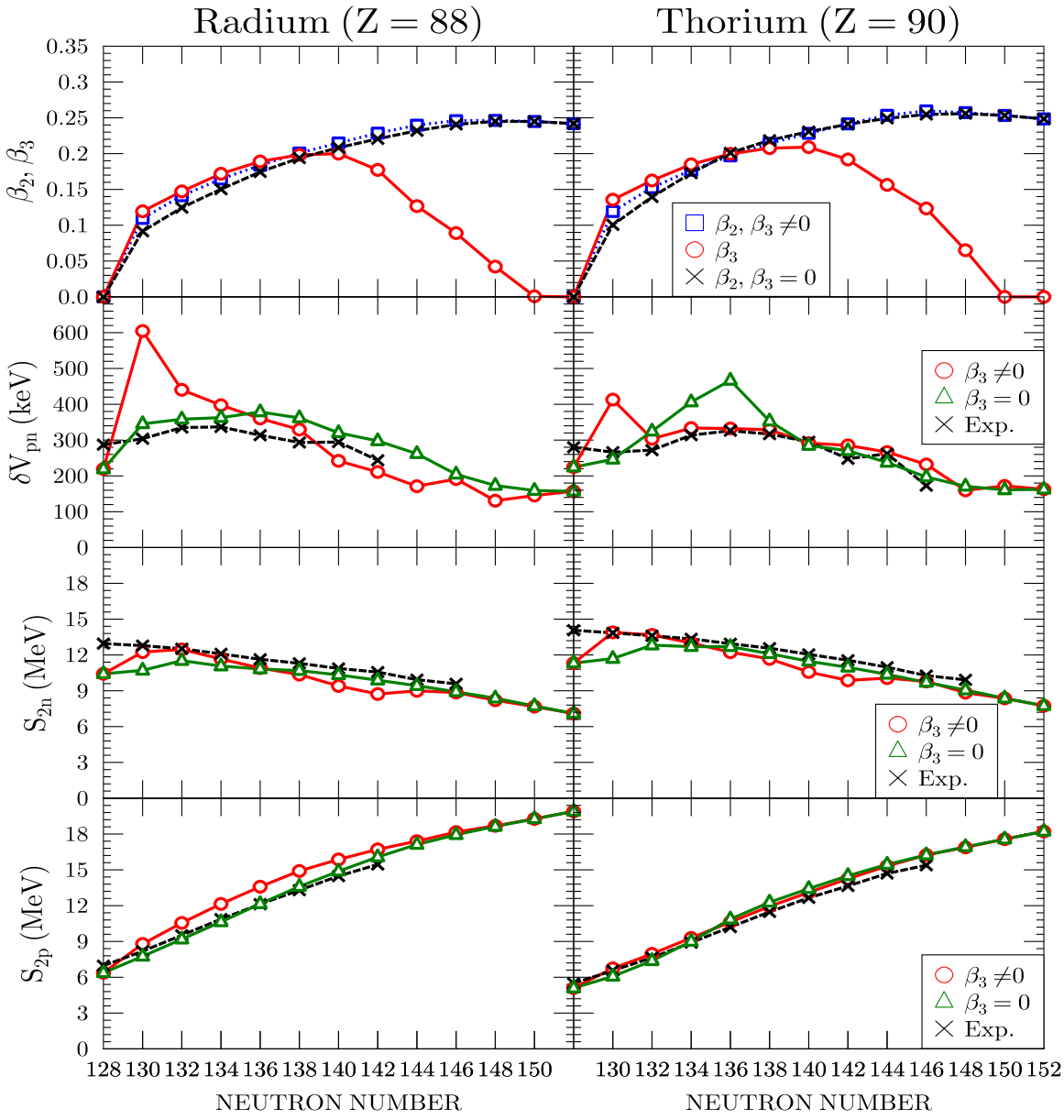


**Figure 6.4:** Top: ground state deformation parameters $\beta_2$ and $\beta_3$ obtained from the ground state minimum found with AxialHFB for radium and thorium isotopes. Solutions allowing for octupole deformations ($\beta_3 \neq 0$) are compared with those assuming reflection-symmetry ($\beta_3 = 0$). Bottom 3 graphs: $\delta V_{pn}$, $S_{2n}$, and $S_{2p}$ for reflection-symmetric (triangles) and asymmetric (circles) shapes compared with experimental values (**x**) of Ref. [185]. The binding energies used to calculate these values are from the SLy4 EDF.

the quadrupole moment is again found to be very small, as the $\beta_2$ values obtained in the full minimization ($\beta_3 \neq 0$) are nearly identical to those obtained assuming reflection-symmetry ($\beta_3 = 0$).

In general, the agreement with experiment for $\delta V_{pn}$ is improved when octupole deformations are included. The spike around $N = 130$ for results with $\beta_3 \neq 0$ is due to the rapid transition between spherical and deformed shapes; this effect (typical to mean-field calculations) is supposed to be minimized if beyond-mean-field effects are taken into account. The effect of octupole deformations on the two-nucleon separation energies $S_{2n}$ and $S_{2p}$ appears to be very small.

## 6.3 Future Work

The quadrupole deformations of the mass table ground state nuclei for AxialHFB closely match those of HFBTHO and demonstrate shell closure in the proper places. The calculations also correctly predict the presence of octupole deformations in the lanthanides and actinides and further suggest their presence in superheavy systems. The initial mass filter analysis suggests that $\delta V_{pn}$ is somehow affected by octupole deformations, bringing it closer to experiment, whereas $S_{2n}$ and $S_{2p}$ are not.

The current task is to make mass table calculations with AxialHFB using the EDFs SkM*, SkP, SLy4, SV-min, UNEDF1, and UNEDF2 (see Chapter 7) and identify cases where the octupole deformation is present. As with UNEDF0, the quadrupole deformations found from those mass tables will be compared with those obtained from HFBTHO to ensure consistency between the two HFB solvers. Once those calculations are complete, the values of $\delta V_{pn}$, $S_{2n}$, and $S_{2p}$ can be found for the mass table of each EDF; this will enable a comprehensive analysis on how octupole deformations affect mass filters.

# Chapter 7

# Nuclear Energy Density Optimization: Shell Structure (UNEDF2)

This chapter is revised based on the following published work:

- M. Kortelainen, J. McDonnell, W. Nazarewicz, E. Olsen, P.-G. Reinhard, J. Sarich, N. Schunck, S. Wild, D. Davense, J. Erler, and A. Pastore, "Nuclear Energy Density Optimization: Shell Structure", *Phys. Rev. C.* **89**, 054314 (2014).

My primary contributions to this paper can be found in Chapter 10.

## 7.1 Introduction

All of the work presented in Chapters 3, 4, 5, and 6 has been about using EDFs to make calculations on quantities not yet known. This corresponds to the third goal of the UNEDF, NUCLEI, and FIDIPRO collaborations listed in Chapter 1. The first two goals listed there talk of building and testing an optimal EDF; what progress has been made towards such a development?

As discussed in Chapter 2, the coupling constants of an EDF are determined through the minimization of a $\chi^2$ objective function. Our optimization strategy [49] involves using HFB solvers and high-performance computing to make calculations on nuclei that could not previously be done easily (such as on deformed or odd-A systems) and including these results (along with selected experimental data) in the $\chi^2$ fit. Once the optimization is complete, linear-regression techniques are used to find correlations between EDF parameters, parameter uncertainties, and errors of calculated observables [68, 72, 190–192]. In this way, the predictive capabilities and theoretical uncertainties of the EDF can be determined.

The first parameterization to use this approach included 44 binding energies from deformed nuclei, 28 binding energies and charge radii from spherical nuclei, and 8 odd-even mass differences within its dataset. Known as UNEDF0 [49], it was found to work well for heavy nuclei and acted as a benchmark for future optimizations. The next parameterization was designed for use in fission and fusion studies and expanded on the dataset of UNEDF0 by adding 3 more binding energies and 4 fission isomer excitation energies. In addition, the center of mass correction to the EDF was removed due to the problems it causes in fission and in shifting single-particle energies. Known as UNEDF1 [50], it was able to reproduce empirical fission barriers in the actinide region while providing a description of global nuclear properties comparable to that of UNEDF0.

The most recent parameterization (known as UNEDF2) was designed to study shell structure, a fundamental property of the atomic nucleus [175]. In order to do this, the dataset of UNEDF1 was expanded to include data on single-particle (s.p.) splittings, as shell structure can be associated with the s.p. spectra of the mean-field potential [77, 193]. A total of 9 empirical data points were chosen from the doubly-magic nuclei $^{40,48}$Ca, $^{132}$Sn, and $^{208}$Pb [194, 195]. The weight of these s.p. data points in the $\chi^2$ function was set to $w = 1.2$ MeV, a choice motivated by the singular value decomposition (SVD) analysis performed in Ref. [191] which showed that Skyrme EDFs can reproduce empirical s.p. levels at this precision level.

S.p. shell structure is also very sensitive to details of the energy density and is the result of the subtle interplay between the gradient terms and the effective mass, spin-orbit, and tensor terms of the EDF [191, 196]. In recent years, the role of these tensor coupling constants (in Skyrme EDFs in particular) has been thoroughly investigated [191, 196–207]. An important conclusion from several of those papers is that the inclusion of tensor terms should not be done perturbatively but should instead involve a complete EDF reoptimization at the deformed HFB level. This implies that constraints on the tensor terms must be included in the pool of fit observables. As such, the tensor terms $C_0^{\mathbb{J}^2}$ and $C_1^{\mathbb{J}^2}$ of equation 2.7 were included in the optimization. Previously, for UNEDF0 and UNEDF1, they were set to zero and not optimized, a choice motivated by the requirement of taking the original SLy4 parameterization [208] as a reference point where these terms were not included.

To build on our previous work, 5 new odd-even mass differences have been added to the UNEDF2 dataset. Their inclusion was motivated by the observation that pairing properties of actinide nuclei and neutron-rich tin isotopes are poorly reproduced by UNEDF1, suggesting that the weight of pairing-related data in the objective function should be increased. In addition to these new experimental points, the weight of all odd-even mass differences in the optimization has been increased from $w = 0.050$ MeV to $w = 0.100$ MeV.

Lastly, the theoretical calculation of s.p. splittings in $^{132}$Sn required the value of its ground state energy. As such, this value was added to the dataset. Experimental information for this value was taken from the 2003 mass evaluation [185] and its weight was set to $w = 2$ MeV, the same value used for the other binding energies of the dataset.

To summarize, the UNEDF2 optimization dataset contains 47 deformed binding energies, 29 spherical binding energies, 28 proton point radii, 13 odd-even mass differences, 4 fission isomer excitation energies, and 9 s.p. level splittings. What are the results of the optimization, and how do they compare with our previous work?

## 7.2 Optimization

The objective function of the optimization was minimized with the POUNDerS (Practical Optimization Using No Derivatives [for Squares]) algorithm [49] where no derivatives are calculated; this was done to facilitate both calculation time and accuracy. All HFB calculations in the UNEDF2 optimization were performed by HFBTHOv200d.

Compared with UNEDF0 and UNEDF1, the standard deviations of the UNEDF2 parameters were smaller overall, reflecting improved constraints on the coupling constants. As expected, both the neutron and proton pairing strengths in UNEDF2 were a little larger, a direct consequence of adding more odd-even mass differences into the dataset. Interestingly, the UNEDF2 and UNEDF1 parameterizations were quite similar overall. This result was a little surprising, as it could be expected that relaxing the constraints on the tensor coupling constants would lead to a significant rearrangement of all of the others, in particular the spin-orbit coupling constants. Indeed, it was shown in Ref. [199] that there is a strong anticorrelation between the isoscalar spin-orbit and tensor coupling constants. Yet in spite of this very strong correlation, the value of $C_0^{\rho\nabla J}$ changed by only 13% between UNEDF1 and UNEDF2.

Sensitivity analysis of the UNEDF2 parameters to both specific data types and individual experimental data points was also performed. It was found that s.p. splittings, fission isomer excitation energies, and odd-even mass differences seemed to be the main drivers of the parameterization, while the relative role of masses was reduced. Two trends were identified: (i) bulk coupling constants (i.e., $\rho$, $K$, and $a_{\mathrm{sym}}$) were not really impacted by odd-even mass differences and (ii) surface coupling constants (involving gradient terms) were more sensitive to odd-even mass differences, fission isomer excitation energies, and s.p. splittings. Overall, the UNEDF2 parameters were shown to have a weak dependence on individual experimental data points; of all the data points, the strongest dependence was from s.p. splittings.

## 7.3 Results of UNEDF2 Calculations

With the optimized parameters of the UNEDF2 functional fully determined, it was necessary to use this EDF in calculations on various nuclear properties to ascertain its quality. As with the optimization, all of the following calculations were completed using HFBTHOv200d. We start with results on shell structure, as this was the main purpose of developing UNEDF2.

The s.p. levels for neutrons in $^{48}$Ca and for protons and neutrons in $^{208}$Pb were calculated and compared with the previous UNEDF EDFs and the measured values of Ref. [194]. The positions of most of the levels calculated with UNEDF2 were found to be slightly improved compared to UNEDF1, which was itself a minor improvement over UNEDF0. The exception was the $N = 28$ gap in $^{48}$Ca which was clearly too small with UNEDF2. The s.p. proton levels in $^{208}$Pb showed that the $Z = 82$ magic gap was too small in both UNEDF1 and UNEDF2 because of their low energy values for the $h_{9/2}$ shell. Further, an inversion of the $1j_{15/2}$ and $1i_{11/2}$ shells between UNEDF1 and UNEDF2 was observed as well as an upward shift in the energy of the $3p_{3/2}$ shell.

To see how well UNEDF2 reproduced global nuclear properties we performed a mass table calculation and obtained binding energies, pairing gaps, and proton radii for even-even nuclei across the whole nuclear landscape. Figure 7.1 shows the residuals of the nuclear binding energies calculated with UNEDF2 with respect to the experimental values for isotopic and isotonic chains of even-even nuclei. Whereas the residuals for the isotopic chains show the typical arc-like features common to many EDF calculations, these are hardly present in the isotonic chain residuals. It is difficult to explain this result, which may point to beyond-mean-field effects not included in our functional and the related bias of the optimization [209].

Figure 7.2 shows the residuals obtained from UNEDF2 for two-neutron and two-proton separation energies. When compared with the prediction of UNEDF1 [50] the slightly worse root-mean-squared deviation (RMSD) for $S_{2n}$ primarily comes from larger deviations at the ends of each isotopic chain. As far as $S_{2p}$ values are

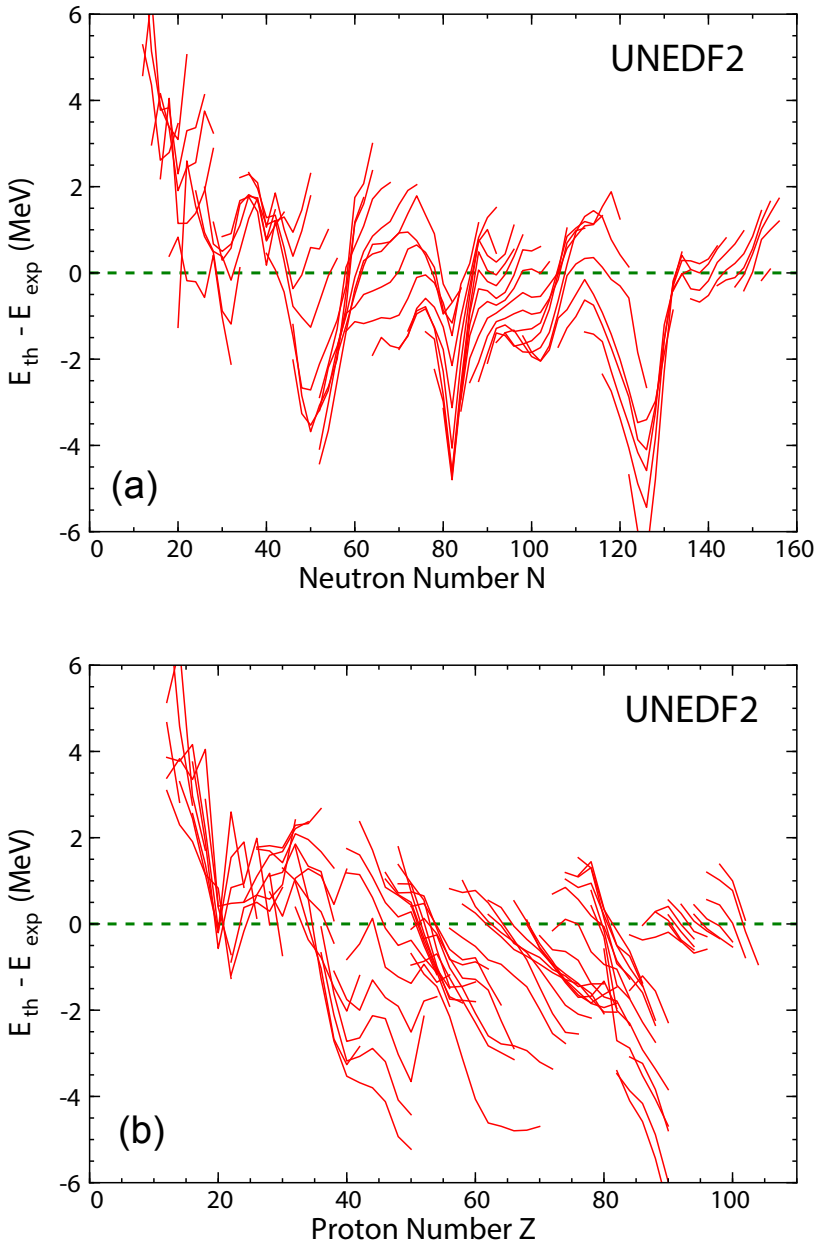


**Figure 7.1:** The residuals of nuclear binding energies of even-even nuclei calculated with UNEDF2. Panel (a) shows isotopic chains, panel (b) the isotonic chains.

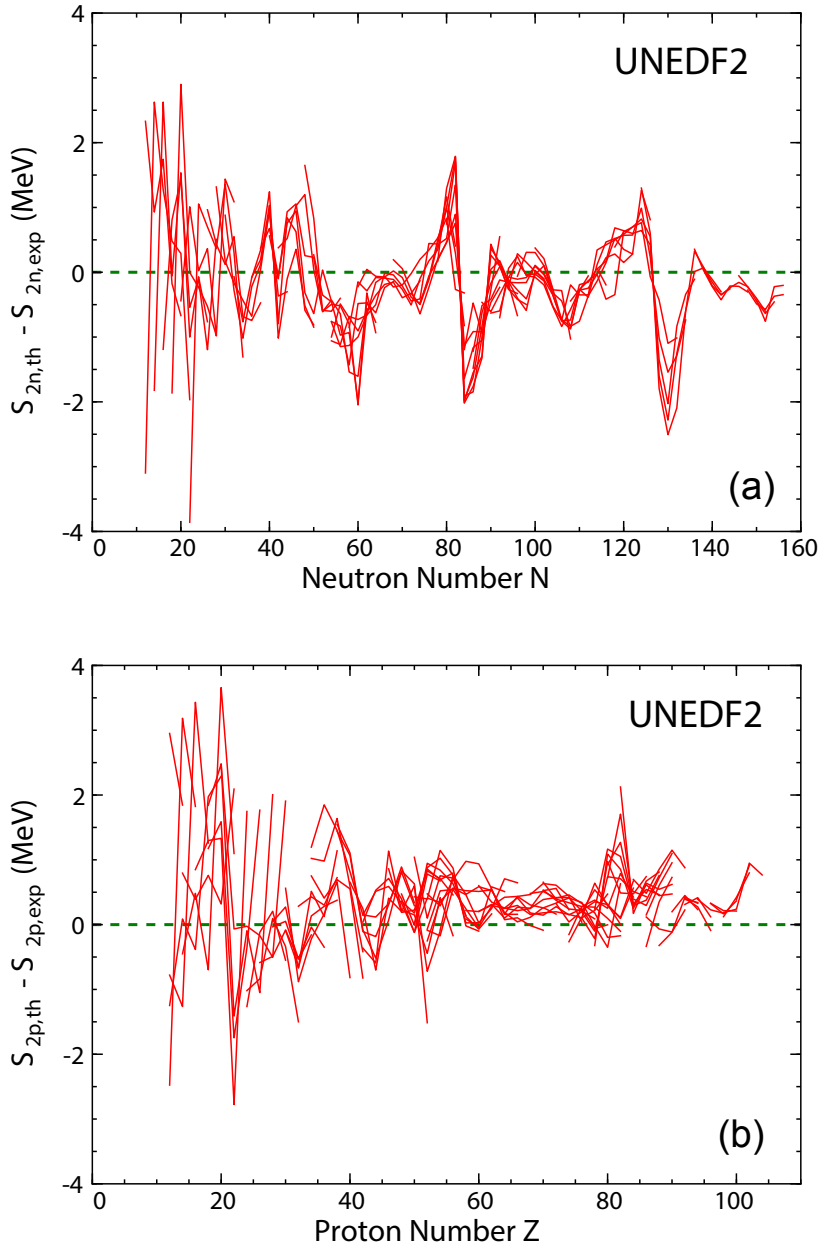


**Figure 7.2:** The residuals of (a) $S_{2n}$ and (b) $S_{2p}$ obtained with UNEDF2 for even-even nuclei.

concerned, UNEDF1 yields values that are systematically too high. This trend is much less pronounced with UNEDF2. Overall, compared with UNEDF1, UNEDF2 is slightly less predictive for binding energies, $S_{2n}$ values, and proton radii, but offers better reproduction of $S_{2p}$ values and neutron pairing gaps. The differences are small, however.

## 7.4 Conclusion

In this study we have introduced the UNEDF2 parameterization of the Skyrme energy density. Compared with our previous EDFs, there are two main differences: (i) we released the requirement that the isoscalar and isovector tensor coupling constants be zero and (ii) we included experimental data on s.p. level splittings in doubly magic nuclei to better constrain spin-orbit and tensor coupling constants. In addition to those major changes, we slightly extended our dataset to improve the pairing properties of the functional, especially in heavy nuclei. Following previous UNEDF optimizations, we performed a comprehensive sensitivity analysis of our parameterization in order to obtain standard deviations and correlations among EDF parameters.

The interval of confidence for the optimized parameters was narrower for UNEDF2 than it was for UNEDF1, which itself was more tightly constrained than UNEDF0. In addition, the results of the sensitivity analysis show that there is relatively weak dependence on individual experimental points. These results point to the fact that the coupling constants of the UNEDF2 functional were properly constrained by the data.

On the other hand, the quality of single-particle shell structure near closed shell nuclei was almost as good as one can get with Skyrme EDFs, but this was almost the case with UNEDF0 and UNEDF1. Global nuclear properties computed with UNEDF2 also reflect little to no improvement with respect to previous parameterizations.

Although one can certainly improve the optimization protocol (for example by changing the relative weights in the $\chi^2$ objective function) we believe this relative lack of improvement should be viewed as an intrinsic limitation of the Skyrme energy density, a local energy density that is up to second order in derivatives [33, 210]. Indeed, as shown in Figures 7.1 and 7.2, the residuals of various quantities predicted with UNEDF2 do not have a statistical distribution; hence, adding more data points or playing with the $\chi^2$ function is not going to change the situation, as the deviations are mainly affected by systematic errors, i.e., imperfect modeling. In this context, UNEDF2 is an all-around Skyrme EDF that is fairly well constrained by various data, but also marks the end of the Skyrme EDF strategy.

At this phase of nuclear DFT developments, it thus seems necessary to go beyond traditional Skyrme functionals. Two major avenues are being explored: one following the spirit of DFT, where the primary building block is the EDF that includes all correlation effects, and the other following the spirit of self-consistent mean-field theory, where the major ingredient is an effective interaction and the beyond-mean-field correlations are added afterwards.

# Chapter 8

# Sum Rules Calculations with the Finite Amplitude Method

## 8.1 Introduction

The focus of the work presented so far has been on calculating properties of nuclear ground states and using those properties for various purposes. What about nuclear excited states? Can the framework used so far be extended to include them as well?

Physically, nuclear excited states are seen as collective vibrations of the nucleus as a whole and are caused by the interaction of the nucleus with external particles through absorption or collisions. For incoming particles with a particular energy a significant increase in the cross-section of absorption can be seen [211]; this energy corresponds to a giant resonance [77]. A nucleus can have multiple giant resonances, each one corresponding to a particular kind of motion and determined by the angular momentum transferred from the incoming particle. If the proton and neutron distributions move as one, the giant resonance is known as isoscalar; if they move opposite to one another, it is known as isovector. The giant resonance is the salient feature of the nuclear excited state and will be the focus of the chapter.

To describe giant resonances, we assume the nucleus starts out in its ground state and is excited through a one-body operator $F$. The response of the nuclear ground state to the action of the operator $F$ is characterized by the strength function $S(\omega)$ [212]:

$$S(\omega) = \sum_{k>0} |\langle k|F|0\rangle|^2 \delta(\omega - \omega_k), \tag{8.1}$$

where $|0\rangle$ is the ground state, $|k\rangle$ are the excited states with corresponding excitation energies $E_k$, and $\omega_k = E_k - E_0$. The strength function gives the excitation spectrum of the nucleus for various values of $\omega$ for a giant resonance defined by the operator $F$.

The calculation of $S(\omega)$ is performed within the framework of the Random Phase Approximation (RPA) [77]. With pairing included, this becomes the Quasiparticle Random Phase Approximation (QRPA). The QRPA method is built directly from the HFB approach, where the second variation of the EDF with respect to $\rho$ and $\tilde{\rho}$ yields the QRPA equations [213]:

$$\begin{pmatrix} A & B \\ B^* & A^* \end{pmatrix} \begin{pmatrix} X \\ Y \end{pmatrix} = \omega \begin{pmatrix} X \\ -Y \end{pmatrix}, \tag{8.2}$$

where $X$ and $Y$ are the matrices of mode amplitudes, $\omega$ is the excitation energy, and $A$ and $B$ are the particle-hole and particle-particle matrices. The mode amplitudes and excitation energy are then used to calculate the entire strength function.

Solving the QRPA equations is no easy task, as the $A$ and $B$ matrices are very large making direct diagonalization both computationally demanding and time consuming. An alternative solution method known as the Finite Amplitude Method (FAM) (integrated into both the RPA [214] and QRPA [215] formalisms) was developed to get around this difficulty. The idea of the FAM is to formulate the QRPA in terms of linear response theory (where the excitation operator $F$ is treated as a perturbation) and solve the resulting equations of $X$ and $Y$ for different values of $\omega$. The strength function is then calculated for individual values of $\omega$ which can be graphed to obtain

a picture of the entire strength function and the energy centroid (position) and width of the giant resonance can be determined visually.

An alternative to the QRPA method is the sum rules approach [212, 216, 217], where the sum rule $m_p$ is related to the one-body Hermitian operator $F$ by [77]:

$$m_p = \sum_k |\langle k|F|0\rangle|^2 (E_k - E_0)^p. \tag{8.3}$$

The total sum of $m_p$ for $-\infty \leq p \leq \infty$ exactly determines the strength function. Fortunately, only a few sum rules are actually needed to obtain information on the giant resonance in question: the inverse energy-weighted sum rule $m_{-1}$, the energy-weighted sum rule $m_1$, and the cubic energy-weighted sum rule $m_3$. Through ratios of these sum rules the average excitation energy of the giant resonance can be found [212]:

$$\begin{aligned} E_1 &= \sqrt{\frac{m_1}{m_{-1}}}, \\ E_3 &= \sqrt{\frac{m_3}{m_1}}, \end{aligned} \tag{8.4}$$

where $E_1$ represents a lower bound for the average excitation energy and $E_3$ an upper bound. The difference of the ratios gives the width $\sigma_{\max}$ of the giant resonance [217]:

$$\sigma_{\max} = \frac{1}{4}\sqrt{\frac{m_3}{m_1} - \frac{m_1}{m_{-1}}}. \tag{8.5}$$

These three sum rules are evaluated within the QRPA framework and typically solved in different ways: $m_{-1}$ through a constrained HFB calculation [218], $m_1$ analytically (in many cases), and $m_3$ through a scaling calculation [219]. A new way of solving the sum rules has recently been proposed by Nobuo Hinohara where through the FAM formalism [220] the calculation of each sum rule can be performed

through contour integration:

$$m_p = \frac{1}{2\pi i} \oint_D \omega^p S(\omega) d\omega = \sum_k \omega_k^p |\langle k|F|0\rangle|^2, \tag{8.6}$$

where $\omega_k^p = (E_k - E_0)^p$ and the contour $D$ encircles all positive frequencies and excludes all singularities in the complex plane.

A subroutine to perform this contour integration was added to HFBTHO to make sum rules calculations. This subroutine was augmented with an MPI routine that sends each discretized part of the integration to a different core to be evaluated; such a routine speeds up calculation time considerably. Calculations have been made for the isoscalar giant monopole resonance which corresponds to a symmetric expansion and contraction of the nucleus and is known as a breathing mode [221]. This resonance was chosen as its excitation energy is proportional to the nuclear incompressibility [222].

## 8.2 Preliminary Results

In Table 8.1 the results of the inverse energy-weighted sum rule $m_{-1}$ are shown for the oblate deformed solution of $^{24}$Mg. To check the results of the FAM sum rule calculations a constrained calculation subroutine was added to HFBTHOv200d which solves the following expression [223]:

$$m_{-1} = \frac{1}{2} A \frac{d\langle r^2(\lambda)\rangle}{d\lambda}\bigg|_{\lambda=0}, \tag{8.7}$$

where $A$ is the mass number, $\langle r^2(\lambda)\rangle$ is the mean square radius of the constrained nucleus, and $\lambda$ is the constraint. The results between the two methods are very consistent which lends confidence to this new sum rules procedure.

**Table 8.1:** The calculation of $m_{-1}$ for the oblate HFB state of $^{24}$Mg using the EDFs SkM* and SLy4. The results of HFBTHOv200d were obtained using a constrained calculation subroutine added to the code. 101 points corresponds to how many points were used in the contour integration.

| | HFBTHOv200d | FAM(101 points) |
|---|---|---|
| SkM* | 5.242 | 5.237 |
| SLy4 | 5.010 | 5.004 |

## 8.3 Future Work

This project is currently in development. The ultimate goal of this work is to demonstrate the usefulness and efficiency of the FAM in calculating sum rules so this data may be used in future EDF parameter fitting. Current plans include extending the MPI routine to allow for mass table calculations of the sum rules for the EDFs SkM*, SkP, SLy4, SV-min, UNEDF0, UNEDF1, and UNEDF2. We also want to extend our calculations to the isoscalar quadrupole, isovector monopole, and isovector quadrupole giant resonances as they can each be related to the symmetry energy of nuclear matter [224, 225].

# Chapter 9

# Conclusion

In this dissertation we have explored the usefulness of using high-performance computing in nuclear physics, specifically in the calculations of large-scale mass tables. We analyzed the limits of nuclear binding and made an estimate on how many particle bound nuclei exist in nature. We studied the phenomenon of two-proton radioactivity to see if it existed in heavy nuclei beyond the two-proton drip line. We calculated neutron skin values and assessed the necessary error bars needed for an experimental measurement to further advance theory. We searched the nuclear landscape for reflection-asymmetric nuclear deformations. We used our knowledge of nuclear theory to formulate a new EDF. And lastly, we enhanced a method for calculating sum rules using parallel computing.

## 9.1 Proton and Neutron Drip Lines

The point at which nuclear binding ends on the nuclear chart is known as the drip line. Where are the drip lines for protons and neutrons, and how many nuclei exist between them? We sought to answer these questions by calculating one and two nucleon separation energies for as many nuclei as possible and observing when their values turned from positive (particle stable) to negative (particle unstable).

Both statistical and systematic errors were assessed, the latter by using 6 EDFs in our calculations. The results from each EDF were unexpectedly consistent, making them fairly robust. Both types of error were rather low for the proton drip line and increased with increasing neutron number. Also, the statistical error never exceeded the systematic error for our calculations. Lastly, we estimate that there are between 6400 and 7400 particle-bound nuclei between the drip lines, though this projection should be seen as specific to 2012.

## 9.2 Two-Proton Radioactivity

$2p$ decay is a phenomenon found in nuclei that exist beyond the two-proton drip line. Current theoretical work has only analyzed this decay mode in elements up to strontium; does it exist in heavier nuclei as well? For the first time we performed a global survey of $2p$ radioactivity and identified candidates for which it can take place. We calculated one and two-proton separation energies, $2p$ and $\alpha$ decay lifetimes for 6 EDFs and imposed selection criteria on each of these values for this identification.

We found that almost all elements between argon and lead have $2p$ decaying isotopes; the exceptions were calcium, chromium, iron, (thought to be a consequence of our selection criteria) and xenon (where $\alpha$ decay dominated). Simultaneous emission was found in nuclei up to tellurium, and sequential emission was found to exist up to isotopes of lead. The upper limit of the $2p$ decay territory was found to be $Z = 82$, for all cases beyond this were dominated by $\alpha$ decay. The most interesting case we found was $^{103}$Te, where $2p$ and $\alpha$ decay were predicted to compete with each other. We also note all the EDFs we used gave similar ranges of $2p$ radioactivity, making the global trends of this survey fairly robust.

## 9.3 Neutron Skins

A feature of nuclei in the neutron-rich region of the nuclear chart is the neutron skin, where the neutron distribution extends further than the proton distribution. The neutron-skin thickness is a useful quantity whose known experimental value would help inform theory about isovector properties of the effective nuclear interaction. What precision does an experimental value need to further advance theory? To help determine this benchmark we performed mass table calculations for proton and neutron rms radii for 6 EDFs and assessed their systematic and statistical errors.

The results of each EDF were found to be rather consistent, making them fairly robust. The average neutron-skin thickness value was found to increase with neutron number and its systematic error was surprisingly low and smaller than the statistical error. Statistical error also propagated with neutron number and its main contribution was found to be the slope of the symmetry energy. Overall, it was found that the expected accuracy of the upcoming CREX experiment (0.02 fm) is sufficient enough to have an impact on reducing the statistical error on neutron-skin thickness.

## 9.4 Reflection-Asymmetric Deformations

Through spontaneous symmetry breaking it is possible for a nucleus in its ground state to acquire a deformed shape. Some possible deformations are ellipsoidal and reflection-asymmetric pear-like shapes. What effect do the latter deformations have on nuclear ground state properties? To explore this problem we performed mass table calculations on even-even nuclei to find binding energies and their associated deformations. We also calculated selected mass filters to isolate specific nuclear interactions to analyze any such effects.

The quadrupole deformation results of AxialHFB match closely with those obtained from HFBTHO. The octupole deformation results were localized to the lanthanide, actinide, and proton-rich superheavy regions of the nuclear chart. The

mass filter $\delta V_{pn}$ was shown to be somehow affected by octupole deformations, whereas the other two $S_{2n}$ and $S_{2p}$ were not. Nothing conclusive can be said of this work at this time, as more data is needed. As such, more mass tables are to be calculated, and with this data more mass filters can be determined and analyzed as well.

## 9.5 UNEDF2

While all of the work so far focused on using EDFs to make calculations on nuclear properties, what progress has been made in the development and testing of new EDFs? The work of the UNEDF, NUCLEI, and FIDIPRO collaborations has produced three nuclear EDFs: UNEDF0, UNEDF1, and the newest parameterization UNEDF2. Building on the work of its predecessors, the dataset of UNEDF2 included single-particle splittings to study shell structure, as well as new odd-even mass differences and an additional binding energy. The optimization procedure was identical to that of UNEDF0 and UNEDF1 and produced an EDF that was fairly well constrained by various data.

Despite the inclusion of single-particle splittings in the dataset, the results of UNEDF2 on shell structure were found to be very similar to those of UNEDF0 and UNEDF1. Similarly, there was little to no improvement in the reproduction of global nuclear properties from the UNEDF2 mass table calculation. We believe this to mean that we have pushed the predictive power of the Skyrme EDF to its intrinsic limit. As such, UNEDF2 marks the end of the Skyrme EDF strategy. Methods are in development to go beyond the Skyrme EDF and include building more effects into the EDF itself and further developing the self-consistent mean-field approach.

## 9.6 Sum Rules

All of our work has focused on nuclear ground states; what about nuclear excited states? Nuclear excitations exist as collective vibrations and exhibit a trait known as

giant resonances, whose energy centroid and width can be related to various nuclear properties. To find the energy centroid and width of a giant resonance we work within the framework of the QRPA which is built from the HFB approach. As solving the QRPA equations is difficult, alternative solutions have been found. The most recent proposed strategy involves using the FAM to calculate the sum rules. The purpose of this project is to validate this new method and demonstrate its worth.

The initial results for the inverse-energy weighted sum rule of this procedure look quite promising. This method will be used in numerous mass table calculations for different sum rules of different giant resonances.

## 9.7 Summary

Through the use of high-performance computing and large-scale mass table calculations we have made a number of useful predictions. We made estimates on the total number of stable nuclei that exist in nature and on the positions of the proton and neutron drip lines. We examined the phenomenon of two-proton decay and found it to be a typical feature of proton-unbound isotopes with even atomic numbers. We studied neutron skins and found the precision necessary for an experimentally measured neutron skin value to be able to further advance theory. We have started to analyze nuclear deformations to see their effects on ground state binding energies and mass filters. We constructed a new EDF, assessed its quality, and found that the Skyrme interaction has taken us as far as it can. Lastly, we created a new method for calculating the sum rules used to extract information from giant resonances.

The goal of nuclear theory to create a comprehensive and quantitative description of nuclear properties and interactions currently remains unfulfilled. It was the purpose of this dissertation to take another step towards achieving such a description by demonstrating how global nuclear properties can be used to advance the collective knowledge of nuclear physics. The use of error analysis through this study gives

confidence to its results and should encourage the use of large-scale mass tables in future work.

# Chapter 10

# My Contributions

- Publications

  1. J. Erler, N. Birge, M. Kortelainen, W. Nazarewicz, E. Olsen, A. Perhac, and M. Stoitsov, "Microscopic Nuclear Mass Table with High-Performance Computing", *J. Phys. Conf. Ser.* **402**, 012030 (2012).

     (a) Proofread and edited the drafts of the paper.

  2. E. Olsen, J. Erler, W. Nazarewicz, and M. Stoitsov,

     "Reflection-Asymmetric Nuclear Deformations within the Density Functional Theory", *J. Phys. Conf. Ser.* **402**, 012034 (2012).

     (a) Using AxialHFB, calculated the binding energy values of Radon, Radium, and Thorium for various quadrupole ($\beta_2$) and octupole ($\beta_3$) deformations.

     (b) Made Figure 2.

     (c) Using AxialHFB, calculated the nuclear density values used in Figure 3.

     (d) Made Figure 3.

     (e) Calculated all $S_{2n}$, $S_{2p}$, and $\delta V_{pn}$ values.

     (f) Made Figures 4 and 5.

(g) Proofread and edited the drafts of the paper.

3. J. Erler, N. Birge, M. Kortelainen, W. Nazarewicz, E. Olsen, A. Perhac, and M. Stoitsov, "The Limits of the Nuclear Landscape", *Nature* **486**, 509 (2012).

   (a) Determined the number of experimentally known even-even isotopes.

   (b) Added the stable and known nuclei to Figure 1.

   (c) Added the dashed $Z$ lines in Supplementary Figures 2, 3, and 4.

   (d) Compiled the data for Supplementary Table 1.

   (e) Proofread and edited the drafts of the paper.

4. E. Olsen, M. Pfützner, N. Birge, M. Brown, W. Nazarewicz, and A. Perhac, "Landscape of Two-Proton Radioactivity", *Phys. Rev. Lett.* **110**, 222501 (2013).

   E. Olsen, M. Pfützner, N. Birge, M. Brown, W. Nazarewicz, and A. Perhac, "Erratum: Landscape of Two-Proton Radioactivity [Phys. Rev. Lett. 110, 222501 (2013)]", *Phys. Rev. Lett.* **111**, 139903 (2013).

   (a) Calculated $Q_p$, $Q_{2p}$ and $Q_\alpha$ for all nuclei from HFBTHO output and filtered the data through the selection criteria $Q_{2p} > 0$, $Q_p < 0.2 * Q_{2p}$.

   (b) For the diproton decay model, calculated the $2p$ lifetime $T_{2p}$ for all nuclei which passed the first criteria and filtered the data through the selection criteria $10^{-7}\text{s} < T_{2p} < 10^{-1}$.

   (c) Calculated the proton overlap function (proportional to the diproton spectroscopic factor) via $\chi^2$ minimization over the experimental half-lives of $^{19}$Mg, $^{45}$Fe, $^{48}$Ni, and $^{54}$Zn.

   (d) For both the direct and diproton decay models, calculated $\alpha$ decay lifetimes for nuclei which passed the second criteria and filtered the data through two selection criteria: $T_{2p} < 0.1 * T_\alpha$ (to find cases where the $2p$ branching ratio is at least 10%) and $0.1 * T_{2p} < T_\alpha < 10 * T_{2p}$ (to find cases where $2p$ and $\alpha$ decay compete).

(e) For both the direct and diproton models, calculated the model multiplicity of each nucleus that passed the third criteria.

(f) Added the diproton, direct ($2p$), and direct ($pp$) lines to Figure 1.

(g) Added the model multiplicity values to Figure 2.

(h) Edited Figures 1 and 2 for the erratum.

(i) Supervised and managed undergraduate students in their work on this research.

(j) Proofread and edited the drafts of the paper.

5. M. Stoitsov, N. Schunck, M. Kortelainen, N. Michel, H. Nam, E. Olsen, J. Sarich, and S. Wild, "Axially Deformed Solution of the Skyrme-Hartree-Fock-Bogoliubov Equations using the Transformed Harmonic Oscillator Basis (II) HFBTHO v2.00d: a new version of the program", *Comp. Phys. Comm.* **184**, 1592 (2013).

   (a) Aided in the development of the MPI for the parallelization of HFBTHOv200d.

   (b) Proofread and edited the drafts of the paper.

6. M. Kortelainen, J. Erler, W. Nazarewicz, N. Birge, Y. Gao, and E. Olsen, "Neutron-Skin Uncertainties of Skyrme Energy Density Functionals", *Phys. Rev. C.* **88**, 031305 (2013).

   (a) Calculated the average value of the neutron skin for each nucleus (data shown on Figure 1$a$).

   (b) Proofread and edited the drafts of the paper.

7. M. Kortelainen, J. McDonnell, W. Nazarewicz, E. Olsen, P.-G. Reinhard, J. Sarich, N. Schunck, S. Wild, D. Davense, J. Erler, and A. Pastore, "Nuclear Energy Density Optimization: Shell Structure", *Phys. Rev. C.* **89**, 054314 (2014).

   (a) Aided in the mass table calculations for HFBTHOv200d.

(b) Proofread and edited the drafts of the paper.

8. N. Hinohara, M. Kortelainen, W. Nazarewicz, and E. Olsen, "Sum Rule Calculation using the Finite Amplitude Method" (*work to be published*).

   (a) Developed the algorithm and wrote the MPI for the parallelization of the sum rule calculation on HFBTHOv200d.

   (b) Added subroutines to HFBTHOv200d to allow for the calculation of the isoscalar monopole giant resonance.

9. E. Olsen, N. Birge, J. Erler, W. Nazarewicz, A. Perhac, N. Schunck, and M. Stoitsov, "Reflection-Asymmetric Nuclear Deformations with Density Functional Theory and High Performance Computing", (*work to be published*).

   (a) Developed the algorithm and wrote the MPI for the parallelization of AxialHFB.

   (b) Changed the Coulomb interaction in AxialHFB to the one used in HFBTHOv200d.

   (c) Added the functional parameterizations SkM*, SkP, SV-min, UNEDF0, UNEDF1, and UNEDF2 to AxialHFB.

   (d) Updated AxialHFB to match results of HFBTHOv200d to the keV scale.

   (e) Performed mass table calculations with AxialHFB for UNEDF0.

- Presentations at Meetings

  – "Octupole Deformations of the Ground States of Nuclei", poster, E. Olsen, W. Nazarewicz, and M. Stoitsov, Conference on Computational Physics, Gatlinburg, TN, October 30-November 3, 2011.

  – "Reflection-Asymmetric Nuclear Deformations within the Density Functional Theory", student talk, E. Olsen, J. Erler, W. Nazarewicz, and M.

Stoitsov, 3rd UiO-MSU-ORNL-UT School on Topics in Nuclear Physics: The computational quantum many-body problem, Oak Ridge National Laboratory, Oak Ridge, TN, January 23-27, 2012.

– "Reflection-Asymmetric Nuclear Deformations within the Density Functional Theory", poster, E. Olsen, J. Erler, W. Nazarewicz, and M. Stoitsov, Stewardship Science Academic Alliances Symposium, Washington D.C., February 22-23, 2012.

– "Reflection-Asymmetric Nuclear Deformations within the Density Functional Theory", poster, E. Olsen, J. Erler, W. Nazarewicz, and M. Stoitsov, American Physical Society April Meeting, Atlanta, GA, March 31-April 3, 2012.

– "Reflection-Asymmetric Nuclear Deformations within Density Functional Theory", E. Olsen, J. Erler, W. Nazarewicz, and M. Stoitsov, Intercollaboration meeting, CEA Saclay, France, April 10-11, 2012.

– "Reflection-Asymmetric Nuclear Deformations within Density Functional Theory", E. Olsen, J. Erler, W. Nazarewicz, and M. Stoitsov, FUSTIPEN Topical Meeting on "The structure of the heavy nuclei" at GANIL, Caen, France, April 16-17, 2012.

– "Density Functional Theory Candidates for 2-Proton Emission", E. Olsen, M. Pfützner, N. Birge, M. Brown, W. Nazarewicz, and A. Perhac, 6th LACM-EFES-JUSTIPEN Workshop at Oak Ridge National Laboratory, Oak Ridge, TN, October 31-November 3, 2012.

– "The Landscape of Two-Proton Radioactivity within Density Functional Theory", E. Olsen, M. Pfützner, N. Birge, M. Brown, W. Nazarewicz, and A. Perhac, NUCLEI Collaboration meeting at Indiana University, Bloomington, IN, June 24-27, 2013.

– "Reflection-Asymmetric Nuclear Deformations within Density Functional Theory", E. Olsen, N. Birge, J. Erler, W. Nazarewicz, A. Perhac,

N. Schunck, and M. Stoitsov, Stewardship Science Academic Alliances Symposium, Albuquerque, NM, June 27-28, 2013.

# Bibliography

[1] A. B. Balantekin *et al*, "Nuclear Theory and Science of the Facility for Rare Isotope Beams," *Mod. Phys. Lett. A*, vol. 29, no. 11, p. 1430010, 2014. 1

[2] RIA Theory Bluebook: A Road Map. A Report from the RIA Theory Group, (2007). 1

[3] J. Erler, P. Klüpfel, and P.-G. Reinhard, "Self-consistent nuclear mean-field models: example Skyrme-Hartree-Fock," *J. Phys. G: Nucl. Part. Phys.*, vol. 38, no. 3, p. 033101, 2011. 1, 11

[4] M. Bender, P.-H. Heenen, and P.-G. Reinhard, "Self-consistent mean-field models for nuclear structure," *Rev. Mod. Phys.*, vol. 75, pp. 121–180, Jan 2003. 1, 9, 11

[5] R. Furnstahl, "The UNEDF Project," *Nucl. Phys. News*, vol. 21, no. 2, pp. 18–24, 2011. 1, 3

[6] R. Machleidt and I. Slaus, "The nucleon-nucleon interaction," *J. Phys. G: Nucl. Part. Phys.*, vol. 27, no. 5, p. R69, 2001. 2

[7] P. Navrátil, J. P. Vary, and B. R. Barrett, "Large-basis *ab initio* no-core shell model and its application to $^{12}$C," *Phys. Rev. C*, vol. 62, p. 054311, Oct 2000. 2

[8] P. Navrátil, S. Quaglioni, I. Stetcu, and B. R. Barrett, "Recent developments in no-core shell-model calculations," *J. Phys. G: Nucl. Part. Phys.*, vol. 36, no. 8, p. 083101, 2009. 2

[9] P. Navrátil and S. Quaglioni, "*Ab initio* many-body calculations of deuteron-$^4$He scattering and $^6$Li states," *Phys. Rev. C*, vol. 83, p. 044609, Apr 2011. 2

[10] B. R. Barrett, P. Navrátil, and J. P. Vary, "*Ab initio* no core shell model," *Prog. Part. Nucl. Phys.*, vol. 69, no. 0, pp. 131 – 181, 2013.

[11] P. Maris *et al*, "Origin of the Anomalous Long Lifetime of $^{14}$C," *Phys. Rev. Lett.*, vol. 106, p. 202502, May 2011. 2

[12] R. B. Wiringa, "Quantum Monte Carlo calculations for light nuclei," *Nucl. Phys. A*, vol. 631, no. 0, pp. 70 – 90, 1998. 2

[13] B. S. Pudliner, V. R. Pandharipande, J. Carlson, S. C. Pieper, and R. B. Wiringa, "Quantum monte carlo calculations of nuclei with $A \leq 7$," *Phys. Rev. C*, vol. 56, pp. 1720–1750, Oct 1997. 2

[14] R. B. Wiringa, S. C. Pieper, J. Carlson, and V. R. Pandharipande, "Quantum Monte Carlo calculations of $A = 8$ nuclei," *Phys. Rev. C*, vol. 62, p. 014001, Jun 2000.

[15] S. C. Pieper and R. B. Wiringa, "Quantum Monte Carlo Calculations of Light Nuclei," *Annu. Rev. Nucl. Part. Sci.*, vol. 51, no. 1, pp. 53–90, 2001.

[16] S. C. Pieper, "Quantum Monte Carlo Calculations of Light Nuclei," *Nucl. Phys. A*, vol. 751, no. 0, pp. 516 – 532, 2005. 2

[17] R. F. Bishop, M. F. Flynn, M. C. Boscá, E. Buendía, and R. Guardiola, "Translationally invariant coupled cluster theory for simple finite systems," *Phys. Rev. C*, vol. 42, pp. 1341–1360, Oct 1990. 2

[18] G. Hagen, T. Papenbrock, D. J. Dean, and M. Hjorth-Jensen, "*Ab initio* coupled-cluster approach to nuclear structure with modern nucleon-nucleon interactions," *Phys. Rev. C*, vol. 82, p. 034330, Sep 2010. 2

[19] A. Bohr and B. R. Mottelson, *Nuclear Structure Volume I.* New York: W. A. Benjamin Inc., 1969. 2, 38

[20] M. G. Mayer, "On Closed Shells in Nuclei. II," *Phys. Rev.*, vol. 75, pp. 1969–1970, Jun 1949. 2

[21] O. Haxel, J. H. D. Jensen, and H. E. Suess, "On the "Magic Numbers" in Nuclear Structure," *Phys. Rev.*, vol. 75, pp. 1766–1766, Jun 1949. 2

[22] B. A. Brown and B. H. Wildenthal, "Status of the Nuclear Shell Model," *Annu. Rev. Nucl. Part. Sci.*, vol. 38, no. 1, pp. 29–66, 1988. 2

[23] N. Michel, W. Nazarewicz, M. Płoszajczak, and T. Vertse, "Shell model in the complex energy plane," *J. Phys. G: Nucl. Part. Phys.*, vol. 36, no. 1, p. 013101, 2009. 2

[24] N. Michel, W. Nazarewicz, M. Płoszajczak, and K. Bennaceur, "Gamow Shell Model Description of Neutron-Rich Nuclei," *Phys. Rev. Lett.*, vol. 89, p. 042502, Jul 2002. 2

[25] N. Michel, W. Nazarewicz, M. Płoszajczak, and J. Okołowicz, "Gamow shell model description of weakly bound nuclei and unbound nuclear states," *Phys. Rev. C*, vol. 67, p. 054311, May 2003. 2

[26] S. E. Koonin, D. J. Dean, and K. Langanke, "Results from Shell-Model Monte Carlo Studies," *Annu. Rev. Nucl. Part. Sci.*, vol. 47, no. 1, pp. 463–504, 1997. 2

[27] T. Otsuka, M. Honma, T. Mizusaki, N. Shimizu, and Y. Utsuno, "Monte Carlo Shell Model for Atomic Nuclei," *Prog. Part. Nucl. Phys.*, vol. 47, no. 1, pp. 319 – 400, 2001. 2

[28] S. E. Koonin, D. J. Dean, and K. Langanke, "Shell Model Monte Carlo Methods," *Phys. Rep.*, vol. 278, no. 1, pp. 1 – 77, 1997. 2

[29] I. Z. Petkov and M. V. Stoitsov, *Nuclear Density Functional Theory*. Oxford: Clarendon Press, 1991. 2

[30] C. Speicher, R. M. Dreizler, and E. Engel, "Density Functional Approach to Quantumhadrodynamics: Theoretical Foundations and Construction of Extended Thomas-Fermi Models," *Ann. Phys.*, vol. 213, no. 2, pp. 312 – 354, 1992. 2

[31] R. M. Dreizler and E. K. U. Gross, *Density Functional Theory*. Berlin: Springer, 1990. 3

[32] J. Dobaczewski *et al*, "Hartree-Fock-Bogolyubov Description of Nuclei near the Neutron-Drip Line," *Nucl. Phys. A*, vol. 422, no. 1, pp. 103 – 139, 1984. 3, 11

[33] E. Perlińska, S. G. Rohoziński, J. Dobaczewski, and W. Nazarewicz, "Local density approximation for proton-neutron pairing correlations: Formalism," *Phys. Rev. C*, vol. 69, p. 014316, Jan 2004. 3, 66

[34] J. Dechargé and D. Gogny, "Hartree-Fock-Bogolyubov calculations with the $D1$ effective interaction on spherical nuclei," *Phys. Rev. C*, vol. 21, pp. 1568–1593, Apr 1980. 3, 8

[35] S. Goriely, S. Hilaire, M. Girod, and S. Péru, "First Gogny-Hartree-Fock-Bogoliubov Nuclear Mass Model," *Phys. Rev. Lett.*, vol. 102, p. 242501, Jun 2009. 3

[36] P.-G. Reinhard, "The relativistic mean-field description of nuclei and nuclear dynamics," *Rep. Prog. Phys.*, vol. 52, no. 4, p. 439, 1989. 3

[37] P. Ring, "Relativistic Mean Field Theory in Finite Nuclei," *Prog. Part. Nucl. Phys.*, vol. 37, no. 0, pp. 193 – 263, 1996. 3

[38] D. Lunney, J. M. Pearson, and C. Thibault, "Recent trends in the determination of nuclear masses," *Rev. Mod. Phys.*, vol. 75, pp. 1021–1082, Aug 2003. 3

[39] M. Stoitsov, W. Nazarewicz, and N. Schunck, "Large-Scale Mass Table Calculations," *Int. J. Mod. Phys. E*, vol. 18, no. 4, pp. 816 – 822, 2009.

[40] J.-P. Delaroche *et al*, "Structure of even-even nuclei using a mapped collective Hamiltonian and the D1S Gogny interaction," *Phys. Rev. C*, vol. 81, p. 014303, Jan 2010.

[41] B. Sun *et al*, "Application of the relativistic mean-field mass model to the $r$-process and the influence of mass uncertainties," *Phys. Rev. C*, vol. 78, p. 025806, Aug 2008. 3

[42] M. V. Stoitsov, J. Dobaczewski, W. Nazarewicz, and P. Borycki, "Large-scale self-consistent nuclear mass calculations," *Int. J. Mass Spectrom.*, vol. 251, no. 23, pp. 243 – 251, 2006. 3

[43] H. Nam *et al*, "UNEDF: Advanced Scientific Computing Collaboration Transforms the Low-Energy Nuclear Many-Body Problem," *JPCS*, vol. 402, no. 1, p. 012033, 2012. 3

[44] S. Bogner *et al*, "Computational nuclear quantum many-body problem: The UNEDF project," *Comput. Phys. Commun.*, vol. 184, no. 10, pp. 2235 – 2250, 2013. 3, 4

[45] NUCLEI collaboration. http://computingnuclei.org. 3

[46] FIDIPRO project. https://www.jyu.fi/fysiikka/en/research/accelerator/fidipro. 3

[47] G. F. Bertsch, D. J. Jean, and W. Nazarewicz, "Computing Atomic Nuclei," *SciDAC Review*, vol. 6, pp. 42–51, 2007. 3

[48] E. Olsen, J. Erler, W. Nazarewicz, and M. Stoitsov, "Reflection-asymmetric nuclear deformations within the Density Functional Theory," *JPCS*, vol. 402, no. 1, p. 012034, 2012. 4, 6, 14, 18

[49] M. Kortelainen *et al*, "Nuclear energy density optimization," *Phys. Rev. C*, vol. 82, p. 024313, Aug 2010. 4, 8, 10, 11, 30, 47, 59, 61

[50] M. Kortelainen *et al*, "Nuclear energy density optimization: Large deformations," *Phys. Rev. C*, vol. 85, p. 024304, Feb 2012. 10, 11, 30, 36, 59, 62

[51] J. Erler, C. J. Horowitz, W. Nazarewicz, M. Rafalski, and P.-G. Reinhard, "Energy density functional for nuclei and neutron stars," *Phys. Rev. C*, vol. 87, p. 044320, Apr 2013. 4, 45, 47

[52] M. Kortelainen *et al*, "Nuclear energy density optimization: Shell structure," *Phys. Rev. C*, vol. 89, p. 054314, May 2014. 4, 7

[53] J. W. Negele and D. Vautherin, "Density-Matrix Expansion for an Effective Nuclear Hamiltonian," *Phys. Rev. C*, vol. 5, pp. 1472–1493, May 1972. 4

[54] R. Machleidt and D. R. Entem, "Chiral effective field theory and nuclear forces," *Phys. Rep.*, vol. 503, no. 1, pp. 1 – 75, 2011. 4

[55] B. Gebremariam, T. Duguet, and S. K. Bogner, "Improved density matrix expansion for spin-unsaturated nuclei," *Phys. Rev. C*, vol. 82, p. 014305, Jul 2010. 4

[56] M. Stoitsov *et al*, "Microscopically based energy density functionals for nuclei using the density matrix expansion: Implementation and pre-optimization," *Phys. Rev. C*, vol. 82, p. 054307, Nov 2010.

[57] B. G. Carlsson and J. Dobaczewski, "Convergence of Density-Matrix Expansions for Nuclear Interactions," *Phys. Rev. Lett.*, vol. 105, p. 122501, Sep 2010. 4

[58] F. Raimondi, B. G. Carlsson, and J. Dobaczewski, "Effective pseudopotential for energy density functionals with higher-order derivatives," *Phys. Rev. C*, vol. 83, p. 054311, May 2011. 4

[59] J. Erler *et al*, "The limits of the nuclear landscape," *Nature*, vol. 486, p. 509, June 2012. 6, 11, 19, 41, 42, 46, 53

[60] E. Olsen *et al*, "Landscape of Two-Proton Radioactivity," *Phys. Rev. Lett.*, vol. 110, p. 222501, May 2013. 6

[61] E. Olsen *et al*, "Erratum: Landscape of Two-Proton Radioactivity [Phys. Rev. Lett. **110**, 222501 (2013)]," *Phys. Rev. Lett.*, vol. 111, p. 139903, Sep 2013. 6

[62] M. Kortelainen *et al*, "Neutron-skin uncertainties of Skyrme energy density functionals," *Phys. Rev. C*, vol. 88, p. 031305, Sep 2013. 6, 11

[63] T. H. R. Skyrme, "The effective nuclear potential," *Nucl. Phys.*, vol. 9, no. 4, pp. 615 – 634, 1959. 8

[64] D. Vautherin and D. M. Brink, "Hartree-Fock Calculations with Skyrme's Interaction. I. Spherical Nuclei," *Phys. Rev. C*, vol. 5, pp. 626–647, Mar 1972. 8

[65] J. Boguta and A. R. Bodmer, "Relativistic Calculation of Nuclear Matter and the Nuclear Surface," *Nucl. Phys. A*, vol. 292, no. 3, pp. 413 – 428, 1977. 8

[66] J. Dobaczewski, W. Nazarewicz, and M. V. Stoitsov, "Nuclear ground-state properties from mean-field calculations," *EPJ A*, vol. 15, no. 1-2, pp. 21–26, 2002. 10

[67] G. F. Bertsch, C. A. Bertulani, W. Nazarewicz, N. Schunck, and M. V. Stoitsov, "Odd-even mass differences from self-consistent mean field theory," *Phys. Rev. C*, vol. 79, p. 034306, Mar 2009. 10, 36

[68] P. Klüpfel, P.-G. Reinhard, T. J. Bürvenich, and J. A. Maruhn, "Variations on a theme by Skyrme: A systematic study of adjustments of model parameters," *Phys. Rev. C*, vol. 79, p. 034310, Mar 2009. 10, 11, 27, 59

[69] E. Chabanat, P. Bonche, P. Haensel, J. Meyer, and R. Schaeffer, "A Skyrme parametrization from subnuclear to neutron star densities," *Nucl. Phys. A*, vol. 627, no. 4, pp. 710 – 746, 1997.

[70] J. R. Stone and P.-G. Reinhard, "The Skyrme interaction in finite nuclei and nuclear matter," *Prog. Part. Nucl. Phys.*, vol. 58, no. 2, pp. 587 – 657, 2007. 10

[71] J. Dobaczewski, W. Nazarewicz, and P.-G. Reinhard, "Error estimates of theoretical models: a guide," *J. Phys. G: Nucl. Part. Phys.*, vol. 41, no. 7, p. 074001, 2014. 11

[72] P.-G. Reinhard and W. Nazarewicz, "Information content of a new observable: The case of the nuclear neutron skin," *Phys. Rev. C*, vol. 81, p. 051303, May 2010. 11, 27, 45, 59

[73] P.-G. Reinhard and W. Nazarewicz, "Information content of the low-energy electric dipole strength: Correlation analysis," *Phys. Rev. C*, vol. 87, p. 014324, Jan 2013. 45

[74] Y. Gao, J. Dobaczewski, M. Kortelainen, J. Toivanen, and D. Tarpanov, "Propagation of uncertainties in the Skyrme energy-density-functional model," *Phys. Rev. C*, vol. 87, p. 034324, Mar 2013. 11, 48

[75] J. Bartel, P. Quentin, M. Brack, C. Guet, and H.-B. Håkansson, "Towards a better parametrisation of Skyrme-like effective forces: A critical study of the SkM force," *Nucl. Phys. A*, vol. 386, no. 1, pp. 79 – 100, 1982. 11

[76] E. Chabanat, P. Bonche, P. Haensel, J. Meyer, and R. Schaeffer, "A Skyrme parametrization from subnuclear to neutron star densities Part II. Nuclei far from stabilities," *Nucl. Phys. A*, vol. 635, no. 12, pp. 231 – 256, 1998. 11

[77] P. Ring and P. Schuck, *The Nuclear Many-Body Problem*. New York: Springer, 1980. 12, 13, 18, 51, 59, 67, 68, 69

[78] J. Bardeen, L. N. Cooper, and J. R. Schrieffer, "Theory of Superconductivity," *Phys. Rev.*, vol. 108, pp. 1175–1204, Dec 1957. 12

[79] M. V. Stoitsov, J. Dobaczewski, W. Nazarewicz, and P. Ring, "Axially deformed solution of the Skyrme–Hartree–Fock–Bogolyubov equations using the transformed harmonic oscillator basis. The program HFBTHO (v1.66p)," *Comput. Phys. Commun.*, vol. 167, no. 1, pp. 43 – 63, 2005. 14

[80] M. V. Stoitsov *et al*, "Axially deformed solution of the Skyrme–Hartree–Fock–Bogoliubov equations using the transformed harmonic oscillator basis (II) HFBTHO v2.00d: A new version of the program," *Comput. Phys. Commun.*, vol. 184, no. 6, pp. 1592 – 1604, 2013. 14, 16

[81] M. V. Stoitsov and I. Zh. Petkov, "Density Functional Theory at Finite Temperatures," *Ann. Phys.*, vol. 184, no. 1, pp. 121 – 147, 1988. 14

[82] H. J. Lipkin, "Collective Motion in Many-Particle Systems: Part 1. The Violation of Conservation Laws," *Ann. Phys.*, vol. 9, no. 2, pp. 272 – 291, 1960. 14

[83] Y. Nogami, "Improved Superconductivity Approximation for the Pairing Interaction in Nuclei," *Phys. Rev.*, vol. 134, pp. B313–B321, Apr 1964. 14

[84] M. V. Stoitsov, J. Dobaczewski, R. Kirchner, W. Nazarewicz, and J. Terasaki, "Variation after particle-number projection for the Hartree-Fock-Bogoliubov method with the Skyrme energy density functional," *Phys. Rev. C*, vol. 76, p. 014308, Jul 2007. 14

[85] M. V. Stoitsov, J. Dobaczewski, P. Ring, and S. Pittel, "Quadrupole deformations of neutron-drip-line nuclei studied within the Skyrme Hartree-Fock-Bogoliubov approach," *Phys. Rev. C*, vol. 61, p. 034311, Feb 2000. 15

[86] J. Erler *et al*, "Microscopic nuclear mass table with high-performance computing," *JPCS*, vol. 402, no. 1, p. 012030, 2012. 15, 16

[87] A. Baran *et al*, "Broyden's method in nuclear structure calculations," *Phys. Rev. C*, vol. 78, p. 014318, Jul 2008. 16

[88] L. M. Robledo and G. F. Bertsch, "Application of the gradient method to Hartree-Fock-Bogoliubov theory," *Phys. Rev. C*, vol. 84, p. 014312, Jul 2011. 18

[89] A. Staszczak, M. Stoitsov, A. Baran, and W. Nazarewicz, "Augmented Lagrangian method for constrained nuclear density functional theory," *EPJ A*, vol. 46, no. 1, pp. 85–90, 2010. 18

[90] National Nuclear Data Center. Evaluated Nuclear Structure Data File. http://www.nndc.bnl.gov/ensdf. 20, 21, 24

[91] M. Thoennessen, "Reaching the limits of nuclear stability," *Rep. Prog. Phys.*, vol. 67, no. 7, p. 1187, 2004. 20, 21, 24, 27

[92] M. Thoennessen and B. Sherrill, "From isotopes to the stars," *Nature*, vol. 473, p. 25, May 2011. 21

[93] New Isotopes Discovered in 2012. http://www.nscl.msu.edu/~thoennes/isotopes-2012/additional-isotopes-2012.pdf. 21, 27

[94] New Isotopes Discovered in 2013. http://www.nscl.msu.edu/~thoennes/isotopes-2013/additional-isotopes-2013.pdf. 21, 27

[95] *Scientific Opportunities with a Rare-Isotope Facility in the United States*. The National Academies Press, 2007. 21, 23

[96] K. Langanke and M. Wiescher, "Nuclear reactions and stellar processes," *Rep. Prog. Phys.*, vol. 64, no. 12, p. 1657, 2001. 21

[97] C. Freiburghaus *et al*, "The Astrophysical r-Process: A Comparison of Calculations following Adiabatic Expansion with Classical Calculations Based on Neutron Densities and Temperatures," *ApJ*, vol. 516, no. 1, p. 381, 1999. 21

[98] M. Beiner, R. J. Lombard, and D. Mas, "Self-consistent calculations of ground state properties for unstable nuclei," *Nucl. Phys. A*, vol. 249, no. 1, pp. 1 – 28, 1975. 22

[99] D. M. Brink and R. A. Broglia, *Nuclear Superfluidity: Pairing in Finite Systems*. Cambridge: Cambridge University Press, 2005. 22

[100] P. Möller, J. R. Nix, W. D. Myers, and W. J. Swiatecki, "Nuclear Ground-State Masses and Deformations," *At. Data and Nucl. Data Tables*, vol. 59, no. 2, pp. 185 – 381, 1995. 24, 25

[101] S. Goriely, N. Chamel, and J. M. Pearson, "Further explorations of Skyrme-Hartree-Fock-Bogoliubov mass formulas. XII. Stiffness and stability of neutron-star matter," *Phys. Rev. C*, vol. 82, p. 035804, Sep 2010. 24, 25

[102] T. Baumann *et al*, "Discovery of $^{40}$Mg and $^{42}$Al suggests neutron drip-line slant towards heavier isotopes," *Nature*, vol. 449, p. 1022, October 2007. 27

[103] E. Lunderberg *et al*, "Evidence for the Ground-State Resonance of $^{26}$**O**," *Phys. Rev. Lett.*, vol. 108, p. 142503, Apr 2012. 27

[104] T. Otsuka, T. Suzuki, J. D. Holt, A. Schwenk, and Y. Akaishi, "Three-Body Forces and the Limit of Oxygen Isotopes," *Phys. Rev. Lett.*, vol. 105, p. 032501, Jul 2010. 27

[105] A. Ekström *et al*, "Optimized Chiral Nucleon-Nucleon Interaction at Next-to-Next-to-Leading Order," *Phys. Rev. Lett.*, vol. 110, p. 192502, May 2013. 27

[106] A. V. Afanasjev, S. E. Agbemava, D. Ray, and P. Ring, "Nuclear landscape in covariant density functional theory," *Phys. Lett. B*, vol. 726, no. 45, pp. 680 – 684, 2013. 28

[107] M. V. Stoitsov, J. Dobaczewski, W. Nazarewicz, S. Pittel, and D. J. Dean, "Systematic study of deformed nuclei at the drip lines and beyond," *Phys. Rev. C*, vol. 68, p. 054312, Nov 2003. 29

[108] M. Matsuo and T. Nakatsukasa, "Open problems in nuclear structure near drip lines," *J. Phys. G: Nucl. Part. Phys.*, vol. 37, no. 6, p. 064017, 2010. 29

[109] D. Vretenar, "Nuclear structure far from stability," *Nucl. Phys. A*, vol. 751, no. 0, pp. 264 – 281, 2005. 29

[110] M. Pfützner, M. Karny, L. V. Grigorenko, and K. Riisager, "Radioactive decays at limits of nuclear stability," *Rev. Mod. Phys.*, vol. 84, pp. 567–619, Apr 2012. 35, 36

[111] B. Blank and M. J. G. Borge, "Nuclear structure at the proton drip line: Advances with nuclear decay studies," *Prog. Part. Nucl. Phys.*, vol. 60, no. 2, pp. 403 – 483, 2008.

[112] B. Blank and M. Płoszajczak, "Two-proton radioactivity," *Rep. Prog. Phys.*, vol. 71, no. 4, p. 046301, 2008.

[113] M. Pfützner, "Particle radioactivity of exotic nuclei," *Phys. Scr.*, vol. 2013, no. T152, p. 014014, 2013. 35, 36, 37, 40

[114] V. I. Goldansky, "On neutron-deficient isotopes of light nuclei and the phenomena of proton and two-proton radioactivity," *Nucl. Phys.*, vol. 19, no. 0, pp. 482 – 495, 1960. 35

[115] M. Pfützner *et al*, "First evidence for the two-proton decay of $^{45}$Fe," *EPJ A*, vol. 14, no. 3, pp. 279–285, 2002. 35

[116] J. Giovinazzo *et al*, "Two-Proton Radioactivity of $^{45}$Fe," *Phys. Rev. Lett.*, vol. 89, p. 102501, Aug 2002. 35

[117] I. Mukha *et al*, "Observation of Two-Proton Radioactivity of $^{19}$Mg by Tracking the Decay Products," *Phys. Rev. Lett.*, vol. 99, p. 182501, Oct 2007. 35

[118] I. Mukha *et al*, "Proton-proton correlations observed in two-proton decay of $^{19}$Mg and $^{16}$Ne," *Phys. Rev. C*, vol. 77, p. 061303, Jun 2008. 35

[119] M. Pomorski *et al*, "First observation of two-proton radioactivity in $^{48}$Ni," *Phys. Rev. C*, vol. 83, p. 061303, Jun 2011. 35

[120] B. Blank *et al*, "First Observation of $^{54}$Zn and its Decay by Two-Proton Emission," *Phys. Rev. Lett.*, vol. 94, p. 232501, Jun 2005. 35

[121] P. Ascher *et al*, "Direct Observation of Two Protons in the Decay of $^{54}$Zn," *Phys. Rev. Lett.*, vol. 107, p. 102502, Sep 2011. 35

[122] K. Miernik *et al*, "Two-Proton Correlations in the Decay of $^{45}$Fe," *Phys. Rev. Lett.*, vol. 99, p. 192501, Nov 2007. 35

[123] L. V. Grigorenko *et al*, "Complete correlation studies of two-proton decays: $^{6}$Be and $^{45}$Fe," *Phys. Lett. B*, vol. 677, no. 12, pp. 30 – 35, 2009. 35

[124] I. A. Egorova *et al*, "Democratic Decay of $^{6}$Be Exposed by Correlations," *Phys. Rev. Lett.*, vol. 109, p. 202502, Nov 2012. 35

[125] B. A. Brown, "Diproton decay of nuclei on the proton drip line," *Phys. Rev. C*, vol. 43, pp. R1513–R1517, Apr 1991. 35, 37, 38

[126] W. E. Ormand, "Properties of proton drip-line nuclei at the *sd-fp*-shell interface," *Phys. Rev. C*, vol. 53, pp. 214–221, Jan 1996.

[127] W. Nazarewicz *et al*, "Structure of proton drip-line nuclei around doubly magic $^{48}$Ni," *Phys. Rev. C*, vol. 53, pp. 740–751, Feb 1996. 37, 38

[128] B. J. Cole, "Stability of proton-rich nuclei in the upper *sd* shell and lower *pf* shell," *Phys. Rev. C*, vol. 54, pp. 1240–1248, Sep 1996.

[129] W. E. Ormand, "Mapping the proton drip line up to $A = 70$," *Phys. Rev. C*, vol. 55, pp. 2407–2417, May 1997. 35

[130] B. A. Brown, R. R. C. Clement, H. Schatz, A. Volya, and W. A. Richter, "Proton drip-line calculations and the *rp* process," *Phys. Rev. C*, vol. 65, p. 045802, Mar 2002. 35, 40

[131] L. V. Grigorenko and M. V. Zhukov, "Two-proton radioactivity and three-body decay. II. Exploratory studies of lifetimes and correlations," *Phys. Rev. C*, vol. 68, p. 054005, Nov 2003. 37, 38

[132] V. Chepurnov *Sov. J. Nucl. Phys.*, vol. 7, p. 1199, 1968. 37

[133] N. Anyas-Weiss *et al*, "Nuclear structure of light nuclei using the selectivity of high energy transfer reactions with heavy ions," *Phys. Rep.*, vol. 12, no. 3, pp. 201 – 272, 1974. 38

[134] B. A. Brown and F. C. Barker, "Di-proton decay of $^{45}$Fe," *Phys. Rev. C*, vol. 67, p. 041304, Apr 2003. 38, 40

[135] H. Koura, "Phenomenological formula for alpha-decay half-lives," *JNST*, vol. 49, no. 8, pp. 816–823, 2012. 39

[136] M. Thoennessen, "Current status and future potential of nuclide discoveries," *Rep. Prog. Phys.*, vol. 76, no. 5, p. 056301, 2013. 41

[137] Discovery of Isotopes Project. http://www.nscl.msu.edu/~thoennes/isotopes/. 41

[138] *Nuclear Physics: Exploring the Heart of Matter*. The National Academies Press, 2013. 44

[139] S. Mizutori, J. Dobaczewski, G. A. Lalazissis, W. Nazarewicz, and P.-G. Reinhard, "Nuclear skins and halos in the mean-field theory," *Phys. Rev. C*, vol. 61, p. 044326, Mar 2000. 45, 47

[140] V. Rotival, K. Bennaceur, and T. Duguet, "Halo phenomenon in finite many-fermion systems: Atom-positron complexes and large-scale study of atomic nuclei," *Phys. Rev. C*, vol. 79, p. 054309, May 2009. 45

[141] B. A. Brown, "Neutron Radii in Nuclei and the Neutron Equation of State," *Phys. Rev. Lett.*, vol. 85, pp. 5296–5299, Dec 2000. 45

[142] R. J. Furnstahl, "Neutron radii in mean-field models," *Nucl. Phys. A*, vol. 706, no. 12, pp. 85 – 110, 2002. 45

[143] J. Piekarewicz *et al*, "Electric dipole polarizability and the neutron skin," *Phys. Rev. C*, vol. 85, p. 041302, Apr 2012. 45, 49

[144] X. Roca-Maza, M. Centelles, X. Viñas, and M. Warda, "Neutron Skin of $^{208}$Pb, Nuclear Symmetry Energy, and the Parity Radius Experiment," *Phys. Rev. Lett.*, vol. 106, p. 252501, Jun 2011.

[145] F. J. Fattoyev and J. Piekarewicz, "Has a Thick Neutron Skin in $^{208}$Pb Been Ruled Out?," *Phys. Rev. Lett.*, vol. 111, p. 162501, Oct 2013. 49

[146] W. Nazarewicz, P.-G. Reinhard, W. Satuła, and D. Vretenar, "Symmetry energy in nuclear density functional theory," *EPJ A*, vol. 50, no. 2, p. 20, 2014. 45

[147] F. Tondeur, M. Brack, M. Farine, and J. M. Pearson, "Static nuclear properties and the parametrisation of Skyrme forces," *Nucl. Phys. A*, vol. 420, no. 2, pp. 297 – 319, 1984. 45

[148] P.-G. Reinhard, "Skyrme forces and giant resonances in exotic nuclei," *Nucl. Phys. A*, vol. 649, no. 14, pp. 305 – 314, 1999.

[149] C. J. Horowitz and J. Piekarewicz, "Neutron Star Structure and the Neutron Radius of $^{208}$Pb," *Phys. Rev. Lett.*, vol. 86, pp. 5647–5650, Jun 2001.

[150] C. J. Horowitz and J. Piekarewicz, "Neutron radii of $^{208}$Pb and neutron stars," *Phys. Rev. C*, vol. 64, p. 062802, Nov 2001.

[151] S. Typel and B. A. Brown, "Neutron radii and the neutron equation of state in relativistic models," *Phys. Rev. C*, vol. 64, p. 027302, Jun 2001.

[152] S. Yoshida and H. Sagawa, "Neutron skin thickness and equation of state in asymmetric nuclear matter," *Phys. Rev. C*, vol. 69, p. 024318, Feb 2004.

[153] F. Sammarruca and P. Liu, "Neutron skin of $^{208}$Pb and density dependence of the symmetry energy," *Phys. Rev. C*, vol. 79, p. 057301, May 2009.

[154] M. Warda, X. Viñas, X. Roca-Maza, and M. Centelles, "Neutron skin thickness in the droplet model with surface width dependence: Indications of softness of the nuclear symmetry energy," *Phys. Rev. C*, vol. 80, p. 024316, Aug 2009.

[155] F. J. Fattoyev and J. Piekarewicz, "Neutron skins and neutron stars," *Phys. Rev. C*, vol. 86, p. 015802, Jul 2012.

[156] F. J. Fattoyev, W. G. Newton, J. Xu, and B.-A. Li, "Generic constraints on the relativistic mean-field and Skyrme-Hartree-Fock models from the pure neutron matter equation of state," *Phys. Rev. C*, vol. 86, p. 025804, Aug 2012.

[157] B. K. Agrawal, J. N. De, and S. K. Samaddar, "Determining the Density Content of Symmetry Energy and Neutron Skin: An Empirical Approach," *Phys. Rev. Lett.*, vol. 109, p. 262501, Dec 2012.

[158] J. M. Lattimer, "The Nuclear Equation of State and Neutron Star Masses," *Annu. Rev. Nucl. Part. Sci.*, vol. 62, no. 1, pp. 485–515, 2012.

[159] A. W. Steiner, J. M. Lattimer, and E. F. Brown, "The Neutron Star Mass-Radius Relation and the Equation of State of Dense Matter," *ApJL*, vol. 765, no. 1, p. L5, 2013. 45, 49

[160] J. Dobaczewski, W. Nazarewicz, and T. R. Werner, "Neutron radii and skins in the Hartree-Fock-Bogoliubov calculations," *Z. Phys. A*, vol. 354, no. 1, pp. 27–35, 1996. 45, 47

[161] S. Abrahamyan *et al*, "Measurement of the Neutron Radius of $^{208}$Pb through Parity Violation in Electron Scattering," *Phys. Rev. Lett.*, vol. 108, p. 112502, Mar 2012. 45, 48

[162] C. J. Horowitz *et al*, "Weak charge form factor and radius of $^{208}$Pb through parity violation in electron scattering," *Phys. Rev. C*, vol. 85, p. 032501, Mar 2012. 45

[163] A. Tamii *et al*, "Complete Electric Dipole Response and the Neutron Skin in $^{208}$Pb," *Phys. Rev. Lett.*, vol. 107, p. 062502, Aug 2011. 45

[164] PREX-II Proposal to Jefferson Lab, http://hallaweb.jlab.org/parity/prex/prexII.pdf. 45, 48

[165] CREX Proposal to Jefferson Lab, http://hallaweb.jlab.org/parity/prex/c-rex2013_v7.pdf. 45, 48

[166] A. Tamii, "Studies of Electric Dipole Resonance in Nuclei Using the Scattering of Polarized Protons," *Acta Phys. Pol. B*, vol. 44, p. 571, 2013. 45

[167] P.-G. Reinhard, M. Bender, W. Nazarewicz, and T. Vertse, "From finite nuclei to the nuclear liquid drop: Leptodermous expansion based on self-consistent mean-field theory," *Phys. Rev. C*, vol. 73, p. 014309, Jan 2006. 47

[168] W. Nazarewicz, "Microscopic Origin of Nuclear Deformations," *Nucl. Phys. A*, vol. 574, no. 12, pp. 27 – 49, 1994. 51

[169] W. Nazarewicz, "Static Multipole Deformations in Nuclei," *Prog. Part. Nucl. Phys.*, vol. 28, no. 0, pp. 307 – 330, 1992. 51

[170] P. A. Butler and W. Nazarewicz, "Intrinsic reflection asymmetry in atomic nuclei," *Rev. Mod. Phys.*, vol. 68, pp. 349–421, Apr 1996. 51, 54

[171] P.-G. Reinhard and E. W. Otten, "Transition to deformed shapes as a nuclear Jahn-Teller effect," *Nucl. Phys. A*, vol. 420, no. 2, pp. 173 – 192, 1984. 51

[172] D. L. Hill and J. A. Wheeler, "Nuclear Constitution and the Interpretation of Fission Phenomena," *Phys. Rev.*, vol. 89, pp. 1102–1145, Mar 1953.

[173] S. Aberg, H. Flocard, and W. Nazarewicz, "Nuclear Shapes in Mean Field Theory," *Annu. Rev. Nucl. Part. Sci.*, vol. 40, no. 1, pp. 439–528, 1990. 51

[174] P. Möller *et al*, "Axial and reflection asymmetry of the nuclear ground state," *At. Data and Nucl. Data Tables*, vol. 94, no. 5, pp. 758 – 780, 2008. 51

[175] A. Bohr and B. R. Mottelson, *Nuclear Structure Volume II*. New York: W. A. Benjamin Inc., 1975. 51, 59

[176] L. P. Gaffney *et al*, "Studies of pear-shaped nuclei using accelerated radioactive beams," *Nature*, vol. 497, p. 199, May 2013. 51

[177] I. Ahmad and P. A. Butler, "Octupole Shapes in Nuclei," *Annu. Rev. Nucl. Part. Sci.*, vol. 43, no. 1, pp. 71–116, 1993. 51

[178] A. S. Jensen, P. G. Hansen, and B. Jonson, "New mass relations and two- and four-nucleon correlations," *Nucl. Phys. A*, vol. 431, no. 3, pp. 393 – 418, 1984. 52

[179] R. B. Cakirli, D. S. Brenner, R. F. Casten, and E. A. Millman, "Proton-Neutron Interactions and the New Atomic Masses," *Phys. Rev. Lett.*, vol. 94, p. 092501, Mar 2005. 52

[180] J.-Y. Zhang, R. F. Casten, and D. S. Brenner, "Empirical proton-neutron interaction energies. Linearity and saturation phenomena," *Phys. Lett. B*, vol. 227, no. 1, pp. 1 – 5, 1989.

[181] D. S. Brenner, R. B. Cakirli, and R. F. Casten, "Valence proton-neutron interactions throughout the mass surface," *Phys. Rev. C*, vol. 73, p. 034315, Mar 2006. 52

[182] M. Stoitsov, R. B. Cakirli, R. F. Casten, W. Nazarewicz, and W. Satuła, "Empirical Proton-Neutron Interactions and Nuclear Density Functional Theory: Global, Regional, and Local Comparisons," *Phys. Rev. Lett.*, vol. 98, p. 132502, Mar 2007. 54

[183] L. M. Robledo, J. L. Egido, J. F. Berger, and M. Girod, "Stable octupole deformation in some actinide nuclei," *Phys. Lett. B*, vol. 187, no. 34, pp. 223 – 228, 1987. 54

[184] J. Erler, K. Langanke, H. P. Loens, G. Martínez-Pinedo, and P.-G. Reinhard, "Fission properties for $r$-process nuclei," *Phys. Rev. C*, vol. 85, p. 025802, Feb 2012. 54

[185] G. Audi, A. H. Wapstra, and C. Thibault, "The AME2003 atomic mass evaluation: (II). Tables, graphs and references," *Nucl. Phys. A*, vol. 729, no. 1, pp. 337 – 676, 2003. 56, 60

[186] J. F. C. Cocks *et al*, "Spectroscopy of Rn, Ra and Th isotopes using multi-nucleon transfer reactions," *Nucl. Phys. A*, vol. 645, no. 1, pp. 61 – 91, 1999. 54

[187] P. T. Greenlees *et al*, "First observation of excited states in $^{226}$U," *J. Phys. G: Nucl. Part. Phys.*, vol. 24, no. 10, p. L63, 1998.

[188] J. F. C. Cocks *et al*, "Observation of Octupole Structures in Radon and Radium Isotopes and Their Contrasting Behavior at High Spin," *Phys. Rev. Lett.*, vol. 78, pp. 2920–2923, Apr 1997.

[189] J. F. Smith *et al*, "Contrasting Behavior in Octupole Structures Observed at High Spin in $^{220}$Ra and $^{222}$Th," *Phys. Rev. Lett.*, vol. 75, pp. 1050–1053, Aug 1995. 54

[190] G. F. Bertsch, B. Sabbey, and M. Uusnäkki, "Fitting theories of nuclear binding energies," *Phys. Rev. C*, vol. 71, p. 054311, May 2005. 59

[191] M. Kortelainen, J. Dobaczewski, K. Mizuyama, and J. Toivanen, "Dependence of single-particle energies on coupling constants of the nuclear energy density functional," *Phys. Rev. C*, vol. 77, p. 064307, Jun 2008. 59, 60

[192] J. Toivanen, J. Dobaczewski, M. Kortelainen, and K. Mizuyama, "Error analysis of nuclear mass fits," *Phys. Rev. C*, vol. 78, p. 034306, Sep 2008. 59

[193] S. Nilsson and I. Ragnarsson, *Shapes and Shells in Nuclear Structure*. Cambridge: Cambridge University Press, 1995. 59

[194] N. Schwierz, I. Wiedenhover, and A. Volya. arXiv:0709.3525, 2007. 59, 62

[195] A. Oros, *Study of the coupling between single-particle and collective degrees of freedom in medium-mass spherical nuclei*. PhD thesis, University of Köln, 1996. 59

[196] W. Satuła, R. A. Wyss, and M. Zalewski, "Contradicting effective mass scalings in the single-particle spectra calculated using the Skyrme energy density functional method," *Phys. Rev. C*, vol. 78, p. 011302, Jul 2008. 60

[197] B. A. Brown, T. Duguet, T. Otsuka, D. Abe, and T. Suzuki, "Tensor interaction contributions to single-particle energies," *Phys. Rev. C*, vol. 74, p. 061303, Dec 2006.

[198] J. Dobaczewski, N. Michel, W. Nazarewicz, M. Płoszajczak, and J. Rotureau, "Shell structure of exotic nuclei," *Prog. Part. Nucl. Phys.*, vol. 59, no. 1, pp. 432 – 445, 2007.

[199] T. Lesinski, M. Bender, K. Bennaceur, T. Duguet, and J. Meyer, "Tensor part of the Skyrme energy density functional: Spherical nuclei," *Phys. Rev. C*, vol. 76, p. 014312, Jul 2007. 61

[200] W. Zou, G. Colò, Z. Ma, H. Sagawa, and P. F. Bortignon, "Tensor correlations and evolution of single-particle energies in medium-mass nuclei," *Phys. Rev. C*, vol. 77, p. 014314, Jan 2008.

[201] D. Tarpanov, H. Liang, N. V. Giai, and C. Stoyanov, "Mean-field study of single-particle spectra evolution in Z=14 and N=28 chains," *Phys. Rev. C*, vol. 77, p. 054316, May 2008.

[202] M. Zalewski, J. Dobaczewski, W. Satuła, and T. R. Werner, "Spin-orbit and tensor mean-field effects on spin-orbit splitting including self-consistent core polarizations," *Phys. Rev. C*, vol. 77, p. 024316, Feb 2008.

[203] M. Zalewski *et al*, "Global nuclear structure effects of the tensor interaction," *Phys. Rev. C*, vol. 80, p. 064307, Dec 2009.

[204] M. Bender *et al*, "Tensor part of the Skyrme energy density functional. II. Deformation properties of magic and semi-magic nuclei," *Phys. Rev. C*, vol. 80, p. 064302, Dec 2009.

[205] M. Moreno-Torres *et al*, "Tensor effects in shell evolution at Z, N = 8, 20, and 28 using nonrelativistic and relativistic mean-field theory," *Phys. Rev. C*, vol. 81, p. 064327, Jun 2010.

[206] Y. Z. Wang, J. Z. Gu, J. M. Dong, and X. Z. Zhang, "Systematic study of tensor effects in shell evolution," *Phys. Rev. C*, vol. 83, p. 054305, May 2011.

[207] M. Grasso and M. Anguiano, "Tensor parameters in Skyrme and Gogny effective interactions: Trends from a ground-state-focused study," *Phys. Rev. C*, vol. 88, p. 054328, Nov 2013. 60

[208] E. Chabanat, P. Bonche, P. Haensel, J. Meyer, and R. Schaeffer, "New Skyrme effective forces for supernovae and neutron rich nuclei," *Phys. Scr.*, vol. 1995, no. T56, p. 231, 1995. 60

[209] M. Bender, G. F. Bertsch, and P.-H. Heenen, "Global study of quadrupole correlation effects," *Phys. Rev. C*, vol. 73, p. 034322, Mar 2006. 62

[210] J. Dobaczewski and J. Dudek, "Time-Odd Components in the Rotating Mean Field and Identical Bands," *Acta Phys. Pol. B*, vol. 27, p. 45, 1996. 66

[211] G. C. Baldwin and G. S. Klaiber, "Photo-Fission in Heavy Elements," *Phys. Rev.*, vol. 71, pp. 3–10, Jan 1947. 67

[212] E. Lipparini and S. Stringari, "Sum rules and giant resonances in nuclei," *Phys. Rep.*, vol. 175, no. 34, pp. 103 – 261, 1989. 68, 69

[213] M. Stoitsov, M. Kortelainen, T. Nakatsukasa, C. Losa, and W. Nazarewicz, "Monopole strength function of deformed superfluid nuclei," *Phys. Rev. C*, vol. 84, p. 041305, Oct 2011. 68

[214] T. Nakatsukasa, T. Inakura, and K. Yabana, "Finite amplitude method for the solution of the random-phase approximation," *Phys. Rev. C*, vol. 76, p. 024318, Aug 2007. 68

[215] P. Avogadro and T. Nakatsukasa, "Finite amplitude method for the quasiparticle random-phase approximation," *Phys. Rev. C*, vol. 84, p. 014314, Jul 2011. 68

[216] E. R. Marshalek and J. da Providência, "Sum Rules, Random-Phase-Approximation, and Constrained Self-Consistent Fields," *Phys. Rev. C*, vol. 7, pp. 2281–2293, Jun 1973. 69

[217] O. Bohigas, A. M. Lane, and J. Martorell, "Sum rules for nuclear collective excitations," *Phys. Rep.*, vol. 51, no. 5, pp. 267 – 316, 1979. 69

[218] S. Stringari, E. Lipparini, G. Orlandini, M. Traini, and R. Leonardi, "Time-dependent Hartree-Fock polarizability and random phase approximation sum rules: (I). Theory," *Nucl. Phys. A*, vol. 309, no. 12, pp. 177 – 188, 1978. 69

[219] J. Martorell, O. Bohigas, S. Fallieros, and A. M. Lane, "Energies and moments of giant resonances for isoscalar monopole and quadrupole excitations: A sum-rule approach," *Phys. Lett. B*, vol. 60, no. 4, pp. 313 – 316, 1976. 69

[220] N. Hinohara, M. Kortelainen, and W. Nazarewicz, "Low-energy collective modes of deformed superfluid nuclei within the finite-amplitude method," *Phys. Rev. C*, vol. 87, p. 064309, Jun 2013. 69

[221] D. H. Youngblood, C. M. Rozsa, J. M. Moss, D. R. Brown, and J. D. Bronson, "Isoscalar Breathing-Mode State in $^{144}$Sm and $^{208}$Pb," *Phys. Rev. Lett.*, vol. 39, pp. 1188–1191, Nov 1977. 70

[222] S. Shlomo and D. H. Youngblood, "Nuclear matter compressibility from isoscalar giant monopole resonance," *Phys. Rev. C*, vol. 47, pp. 529–536, Feb 1993. 70

[223] J. Treiner, H. Krivine, O. Bohigas, and J. Martorell, "Nuclear incompressibility: From finite nuclei to nuclear matter," *Nucl. Phys. A*, vol. 371, no. 2, pp. 253 – 287, 1981. 70

[224] M. Casas, J. Martorell, and J. M. G. Gomez, "Giant isovector monopole resonances and the symmetry energy of nuclear matter," *Phys. Lett. B*, vol. 152, no. 12, pp. 6 – 10, 1985. 71

[225] G. Scamps and D. Lacroix, "Systematics of isovector and isoscalar giant quadrupole resonances in normal and superfluid spherical nuclei," *Phys. Rev. C*, vol. 88, p. 044310, Oct 2013. 71

# Vita

Erik Michael Olsen was born in Stony Brook, New York to Paul and Diane Olsen. All throughout school he was interested in math, science, and music, but became particularly interested in physics after taking a course on the subject in high school. After graduating from Longwood High School in 2003 he went on to study physics at The State University of New York (SUNY) Geneseo. From there he found a special interest in quantum mechanics and eventually nuclear physics. He graduated from college with a Bachelor of Arts degree in Physics in 2007 and entered into the graduate physics program of The University of Tennessee, Knoxville in that same year. He started work with Dr. Witek Nazarewicz on theoretical nuclear physics in 2009.